Neutron-Gamma Ray Discrimination Using Normalized Cross Correlation

by

Premkumar Chandhran

A Thesis Presented in Partial Fulfillment
of the Requirements for the Degree
Master of Science

Approved May 2015 by the
Graduate Supervisory Committee:

Keith E. Holbert, Chair
Andreas Spanias
Umit Y. Ogras

ARIZONA STATE UNIVERSITY

August 2015

ABSTRACT

The reduced availability of ^{3}He is a motivation for developing alternative neutron detectors. ^{6}Li-enriched CLYC (Cs_2LiYCl_6), a scintillator, is a promising candidate to replace ^{3}He. The neutron and gamma ray signals from CLYC have different shapes due to the slower decay of neutron pulses. Some of the well-known pulse shape discrimination techniques are charge comparison method, pulse gradient method and frequency gradient method. In the work presented here, we have applied a normalized cross correlation (NCC) approach to real neutron and gamma ray pulses produced by exposing CLYC scintillators to a mixed radiation environment generated by ^{137}Cs, ^{22}Na, ^{57}Co and ^{252}Cf/AmBe at different event rates. The cross correlation analysis produces distinctive results for measured neutron pulses and gamma ray pulses when they are cross correlated with reference neutron and/or gamma templates. NCC produces good separation between neutron and gamma rays at low (< 100 kHz) to mid event rate (< 200 kHz). However, the separation disappears at high event rate (> 200 kHz) because of pileup, noise and baseline shift. This is also confirmed by observing the pulse shape discrimination (PSD) plots and figure of merit (FOM) of NCC. FOM is close to 3, which is good, for low event rate but rolls off significantly along with the increase in the event rate and reaches 1 at high event rate. Future efforts are required to reduce the noise by using better hardware system, remove pileup and detect the NCC shapes of neutron and gamma rays using advanced techniques.

To my amma and naina, relatives, friends, mentors, professors, I couldn't have done this without you.

Thank you all for your support along the way.

ACKNOWLEDGEMENTS

I would like to thank my advisor Dr. Keith E. Holbert for his guidance throughout the course of my Master's program. He has been a constant source of inspiration and his advice has been invaluable to me.

I also thank my defense committee members Dr. Andreas Spanias and Dr. Umit Y. Ogras, and my graduate advisor Ms. Christina Sebring for their help.

My sincere thanks to Dr. Erik B. Johnson, Sam Vogel, and Arindam Dutta. This work would not have been possible without their support.

TABLE OF CONTENTS

Page

CHAPTER Page

LIST OF TABLES

LIST OF FIGURES

Figure Page

Figure Page

Figure Page

Figure Page

Figure Page

CHAPTER 1. INTRODUCTION

Nuclear energy is a form of potential energy which is important to mankind. It has been used to generate electricity, power rockets, propel ships and used in other civilian applications. At the same time, it has potential to wipe out mankind if not used in the right way. Due its enormous destructive potential, nuclear resources are heavily protected and controlled by the governments across the world. In order to promote the safe, secure and peaceful use of nuclear technologies, the International Atomic Energy Agency (IAEA) has been formed with 165 nations as its members. The IAEA requires its members to maintain a State System of Accounting for and Control (SSAC) of nuclear material. The IAEA emphasizes nuclear material safeguards such as physical protection, export controls and combating the illicit trafficking of nuclear materials. According to the IAEA [1], nuclear material accounting refers to "activities carried out to establish the quantities of nuclear material present within defined areas and the changes in those quantities within defined periods."

One of the important instruments in nuclear material accounting is the neutron detector. Neutrons do not have electrical charge so neutron detectors rely upon a conversion process where an incoming neutron interacts with a nucleus to produce secondary charged particles. These charged particles are then directly detected and from them the presence of neutrons is confirmed. As described in [1], there are three main categories of neutron detectors such as proportional detectors, scintillation detectors and semiconductor detectors. Helium-3 proportional detectors are the gold standard

for neutron detection because of their high neutron detection efficiency, nontoxicity and insensitivity to gamma rays.

Helium-3 is generally produced as a byproduct of radioactive decay of tritium. The ceasestation of tritium production has led to a decrease in the stock of Helium-3. However, the increase in the demand for neutron detectors drove the cost of Helium-3 high. It is estimated that the worldwide demand for Helium-3 is 65,000 L with an annual supply of 15,000 L [2]. It was estimated in 2010 that the current stock of helium-3 was ~50,000 L within the U.S. [3].

All these factors led to focusing on other neutron detectors. Scintillator detectors use solid or liquid scintillating materials, which are materials that emit light when struck by an incoming ionizing particle. The conversion material is incorporated in the scintillator. When the conversion material absorbs neutrons, the resulting charged particles deposit energy in the scintillating material, which causes the scintillator to emit light that can be converted to an electric signal. References [3], [4], [5] and [6] identified CLYC (Cs_2LiYCl_6), a scintillation material, as a promising candidate which can replace He-3. Radiation Monitoring Devices (RMD), a Watertown based company, is fabricating ^{6}Li enriched CLYC, where the ^{6}Li (n,α) ^{3}H reaction has a large neutron cross section, and with a high density of ^{6}Li, the material exhibits a high detection efficiency.

The disadvantage of CLYC compared to Helium-3 is its sensitivity to gamma rays. In order to distinguish neutrons from gamma rays, pulse shape discrimination (PSD) methods are employed to separate the two radiations based on their pulse shape. The research effort reported in this thesis is focused on finding suitable PSD techniques to discriminate neutron and gamma rays at high event rates. The CLYC material emits light over many microseconds, limiting the ability to distinguish gammas from neutrons when the gamma event rates are high (> 200 kHz), as the light pulses will pile up on each other. As a result of this, traditional PSD methods such as the charge comparison method, pulse gradient analysis, and frequency gradient analysis fail to discriminate neutrons and gamma rays. An alternative PSD method based on the normalized cross correlation (NCC) has been evaluated and tested using the hardware developed by RMD.

Chapter 2 outlines the different PSD techniques to discriminate neutron and gamma rays based on their pulse shape and CLYC based neutron detection system. Chapter 3 describes the NCC method, Marrone's neutron and gamma ray pulse modelling and explains the metrics to compare different PSD techniques. Chapter 4 explains the experimental setup to produce the neutron and gamma ray data for different event rates and also shows the application of the NCC method discussed in Chapter 3. Chapter 5 discusses the results of the NCC method and provides a comparison of the NCC method with other PSD methods. Finally, Chapter 6 summarizes the results of the research and future scope.

CHAPTER 2. BACKGROUND

2.1. Overview

Advancements in digital electronics are an incentive to use digital signal processing (DSP) techniques to differentiate between neutron and gamma ray pulses. Pulses from neutrons exhibit a longer decay time than pulses from gamma rays [7] as shown in Fig. 2.1. Pulse shape discrimination (PSD) techniques that distinguish neutrons from gamma rays based on the shape of the pulses are available. Some of the well-known PSD techniques include the charge comparison method, pulse gradient analysis, frequency gradient analysis, simplified digital charge collection, neutron gamma model analysis, zero-crossing method, similarity method, bipolar trapezoid pulse shaping technique, wavelet transform based method and normalized cross correlation method [8], [9], [10], [11], [12], [13], [14]. These PSD methods and their efficacy are discussed in this chapter.

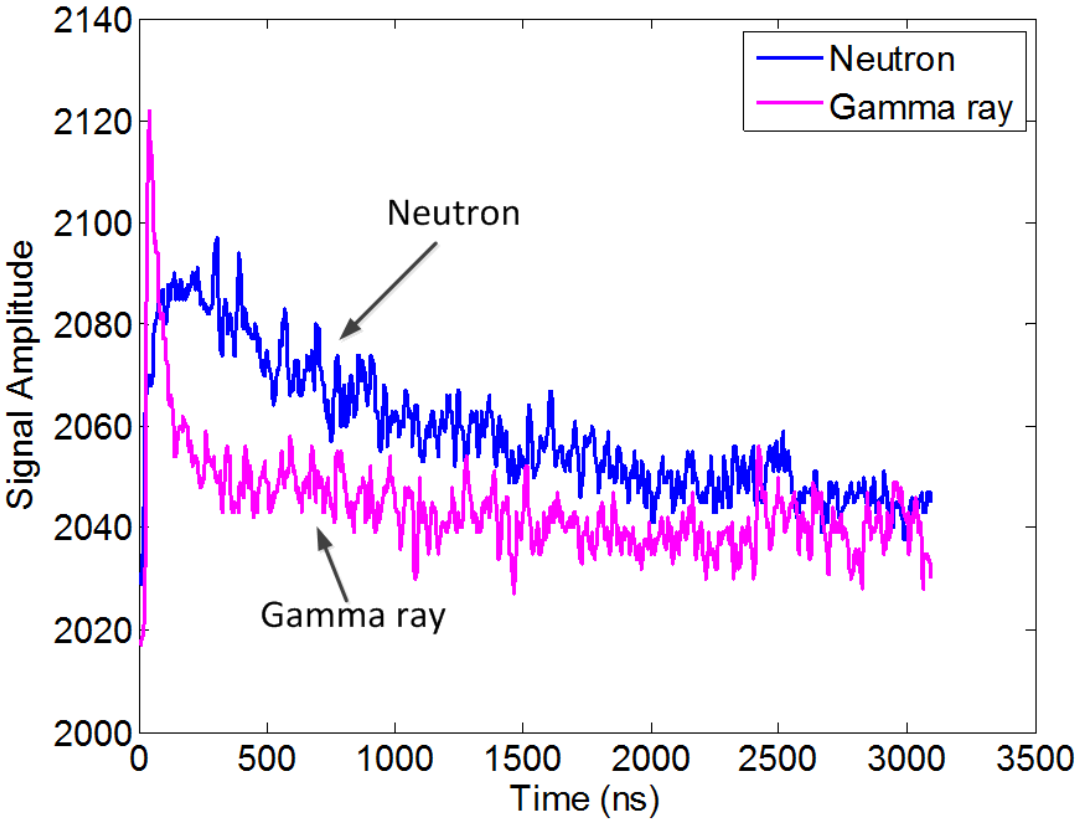

Fig. 2.1 Representative Neutron and Gamma Ray Pulses from CLYC.

2.2. Charge Comparison Method

The charge comparison method is based on a comparison of the integrals under a pulse, over two different intervals often referred to as the long integral and the short integral [8]. The long integral corresponds to the area of the entire pulse whereas the short integral corresponds to only a part of the tail area. This approach is very popular in the analog domain. In the digital domain, short and long integral are sums of samples over the two different periods. The start and end times for the long integral are the same as the start and the end of the pulse, whereas for the short integral, an optimum value after the peak is chosen as the start time and the end of the pulse is the end time. Neutrons and gamma rays are discriminated by using this method because the neutron pulse decays slowly and it has a larger short integral for the same long integral compared to a gamma ray. Pulse shape discrimination is obtained by plotting the short integral value against long integral value. Fig. 2.2 shows the neutron-gamma pulse shape discrimination using the CCM as reported in [8]. In Fig. 2.2, the upper and lower plumes correspond to neutron and gamma events, respectively. It is evident from the discussion above that the CCM depends on the time domain features of the pulses. Often pulses from PMT are very noisy and the time domain features are affected by this noise. This makes this method to be dependent on additional de-noising algorithms. Even with this, the method is observed to be failing at very high event rate and in mixed radiation environment.

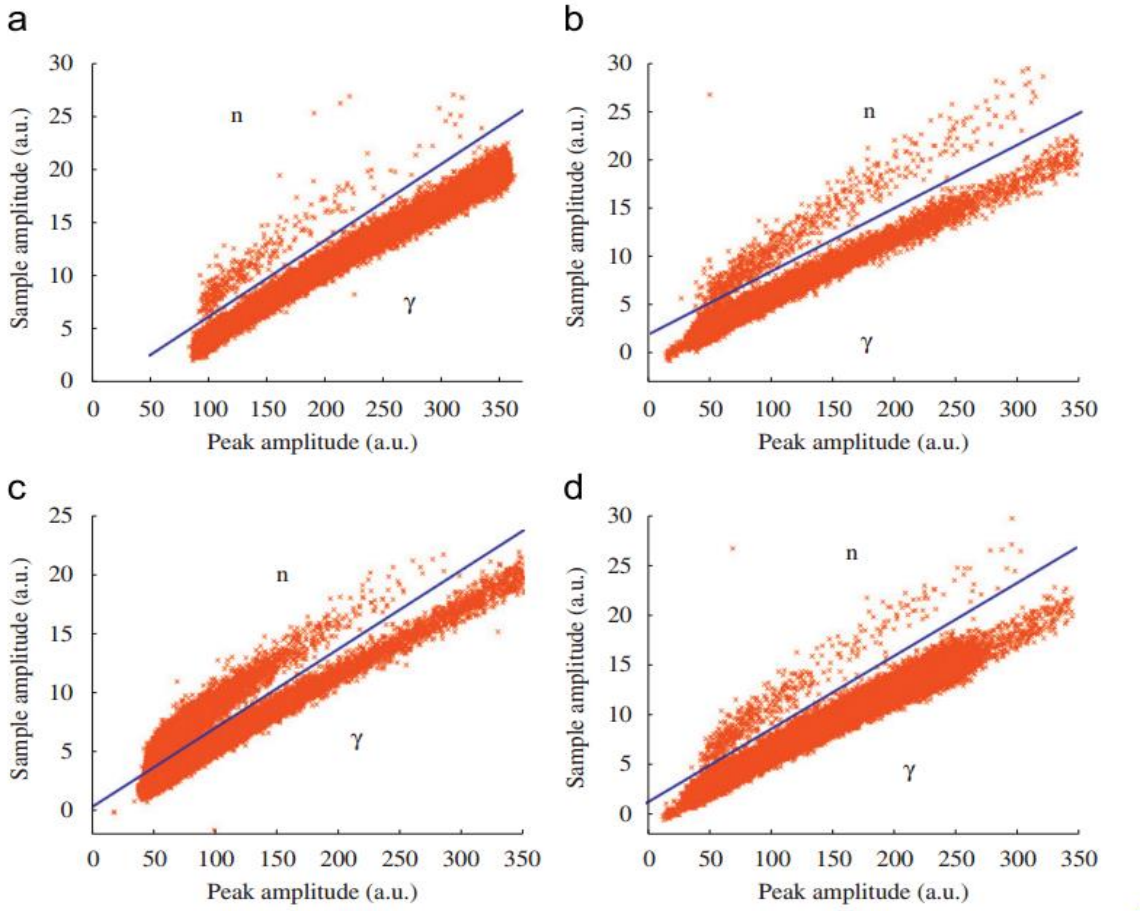

Fig. 2.2 Neutron-Gamma Discrimination Using CCM [8] for a) AmBe*, b)* AmLi*, c)* ^{252}Cf*, d)* PuLi.

2.3. Simplified Digital Charge Collection (SDCC)

As discussed in [8], SDCC is based on the peak amplitude and a discrimination parameter (D), which is calculated using the short integral via

$$D = log(\sum_{n=a}^{n=b} x_n^2) \quad (1)$$

Where x_n is the sample amplitude of the n^{th} sample, and a and b are the indexes associated with the start and the end, respectively, of the short integral. In particular, a and b correspond to the sample values at the three-sixteenths and one-half of the pulse,

respectively. The discrimination parameter is plotted against the peak amplitude to get the pulse shape discrimination plot as shown in Fig. 2.3.

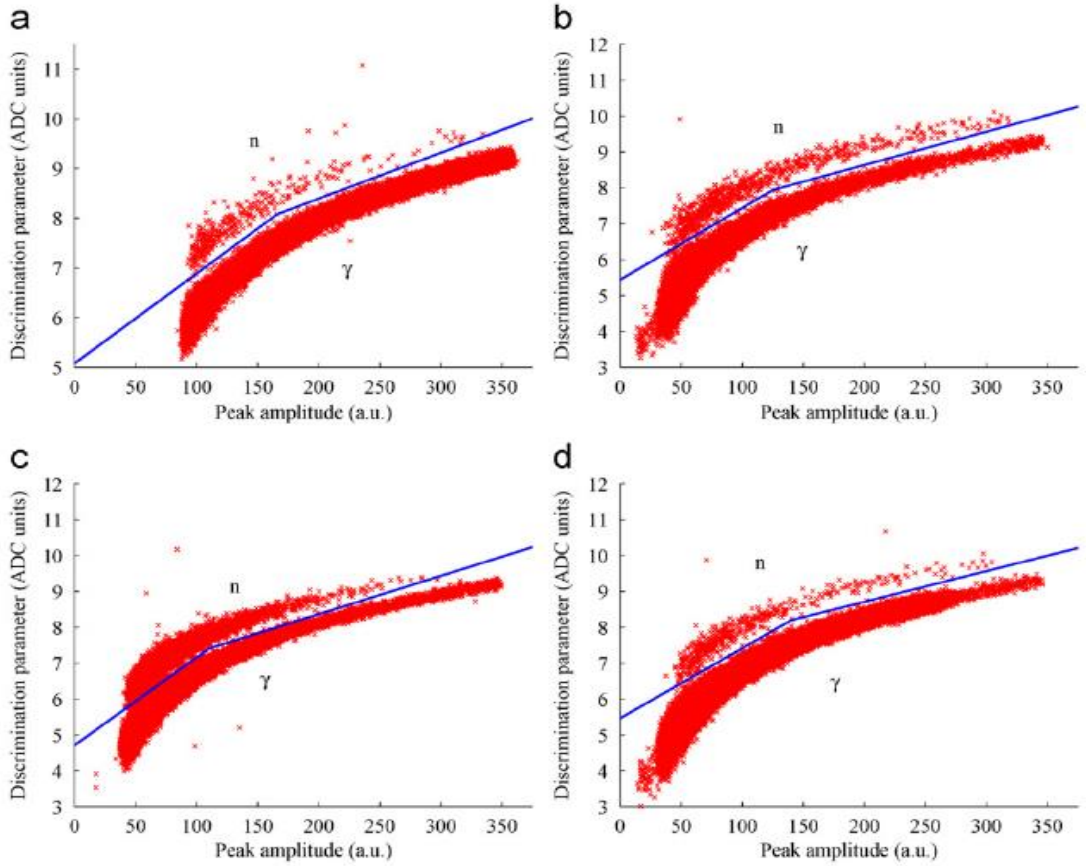

Fig. 2.3 Neutron-Gamma Pulse Shape Discrimination Plot Using SDCC [8] for a) AmBe*, b)* AmLi*, c)* ^{252}Cf*, d)* PuLi.

2.4. Pulse Gradient Analysis

Pulse gradient analysis (PGA) exploits the characteristic that the slope is lower on the trailing edge of the pulse as a result of slower decay to the baseline exhibited by a neutron signal. PGA compares the peak amplitude and amplitude of a sample occurring at a defined time interval after the peak amplitude to discriminate the pulse associated with neutrons and gamma rays. The optimum time for the second sample

should be determined for the apparatus used, as it is dependent on the properties of the scintillator and the photomultiplier tube (PMT). The pulse shape discrimination of the PGA method is obtained by plotting the peak amplitude with the amplitude of the second sample. Reference [9] estimates the Figure Of Merit (FOM), a metric for the separation of neutron and gamma rays, of the PGA method and reports it to be 1.23 when the signal-to-noise ratio (SNR) is 36.5 dB, infinity in the absence of noise, and zero when the SNR is 20 dB based on simulation analysis.

Reference [9] also discusses the experimental results obtained for an americium-beryllium (AmBe) source. Fig. 2.4 shows a sample PGA plot. From Fig. 2.4, we can observe two distinct groups of events, the right group corresponds to neutrons and the left corresponds to gamma rays. If the ratio of peak amplitude to the second sample is 11.41, it is regarded as a gamma ray and a neutron if it is below 11.41. Considerable research needs to be conducted in determining this ratio. Fig. 2.5 shows the neutron-gamma discrimination plot using the charge comparison method (CCM). From Fig. 2.4, which corresponds to PGA, we can observe that neutron and gamma events are better separated when compared to, Fig. 2.5 which corresponds to CCM. From this, it is evident that PGA out performs CCM. It was observed in [9] that the PGA method shows 11.9% improvement over the charge comparison method.

Sometimes when the noise level is very high, the PGA technique might fail to show sufficient discrimination. In order to reduce the noise we may have to use digital filters

before analyzing the data with PGA. Reference [8] presents the PGA plot as shown in Fig. 2.6 for different sources such as AmBe, AmLi, ^{252}Cf, and PuLi. A neutron-induced pulse has higher discrimination amplitude for the same peak amplitude, compared to a gamma ray due to its pulse's slower decay rate. Hence, neutrons correspond to the events in the upper plume and gamma rays correspond to the events in the lower plume in these plots. Reference [9] concludes that PGA is a fast and stable digital technique for discriminating neutron and gamma ray events within an organic scintillator. CLYC is an inorganic scintillator.

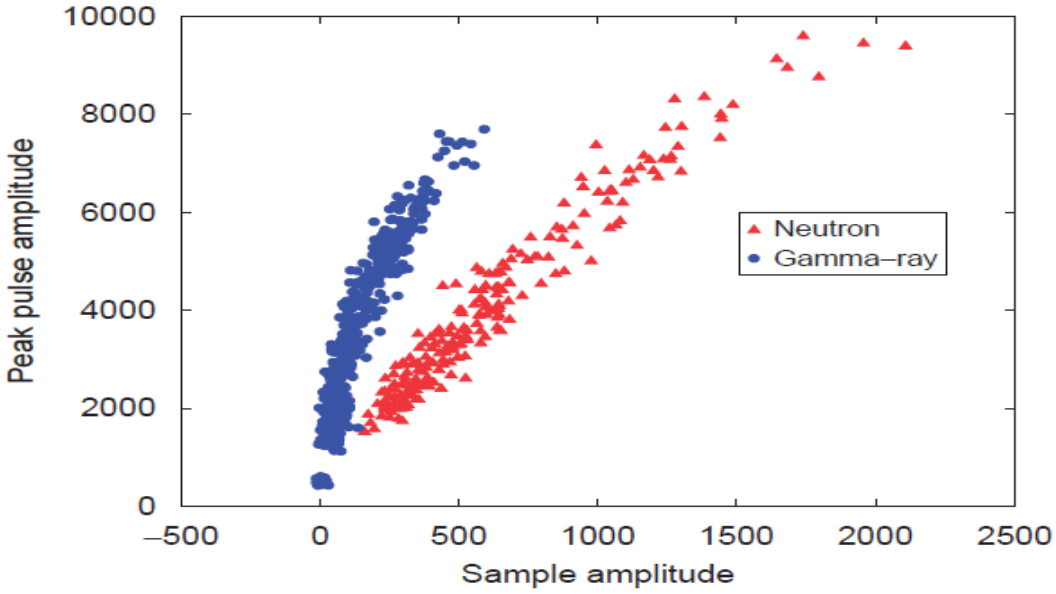

Fig. 2.4 Neutron-Gamma Discrimination Using PGA [9].

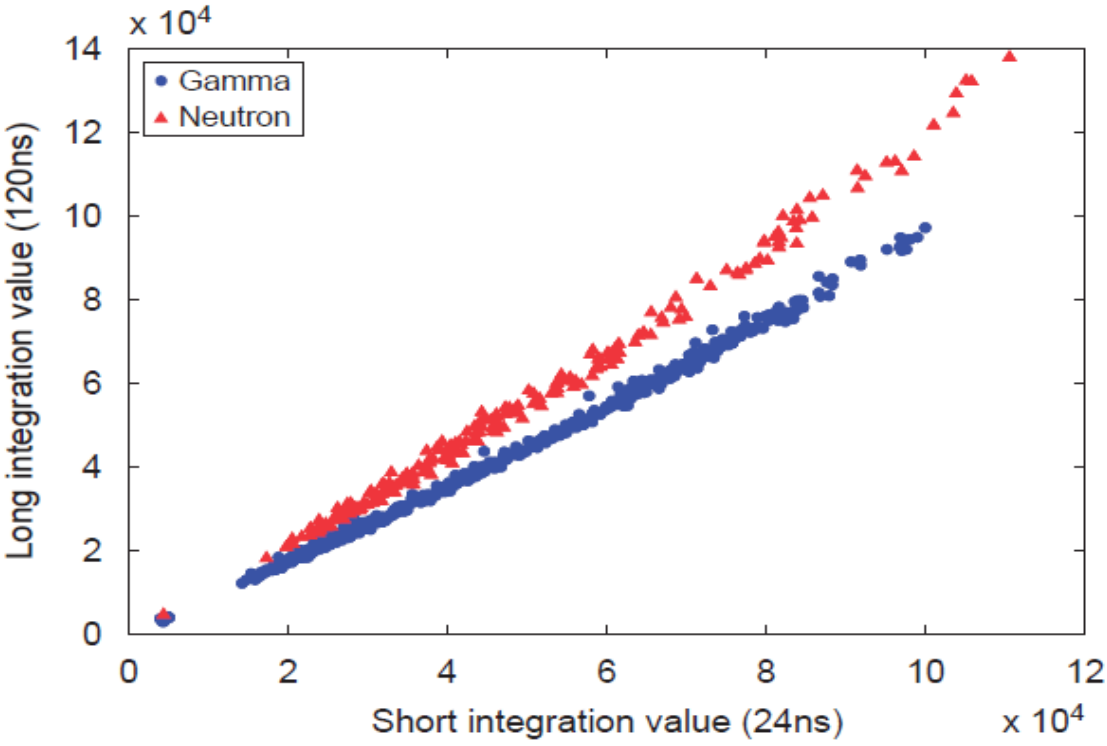

Fig. 2.5 Neutron-Gamma Discrimination Using CCM [9].

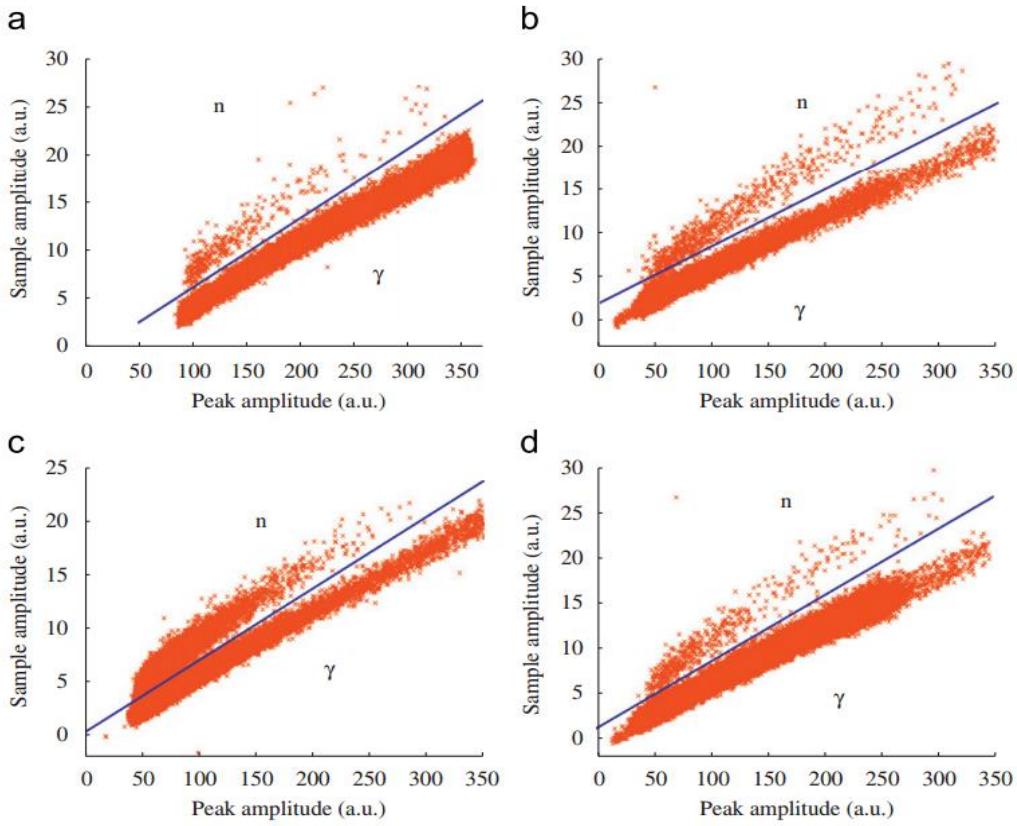

Fig. 2.6 Neutron-Gamma Discrimination Plot Using PGA[8] for a) AmBe*, b)* AmLi, *c)* ^{252}Cf*, d)* PuLi.

2.5. Frequency Gradient Analysis (FGA)

In this method, the pulse shapes of neutron and gamma rays are converted into the frequency domain using the discrete Fourier transform. A distinct difference in the magnitude spectrum of neutron and gamma rays is observed. This has been used as a basis for discriminating neutron and gamma pulses. Fig. 2.7 shows the pulse shapes of neutrons and gammas in the frequency domain. From Fig. 2.7, we observe that the two waveforms intersect at 13.9 MHz. Below this frequency the amplitude of each frequency component of the neutron pulse is greater than that of the gamma pulse, and the

magnitude spectrum of the neutron pulse decreases more sharply than that of the gamma-ray pulse. However, above this frequency the magnitude spectra of both pulses have nearly identical amplitude so it is impossible to discriminate. The gradient used by FGA is defined as the difference between the zero-frequency component and the first frequency component of the Fourier transform of the acquired signal, which is extracted from the frequency domain. FGA has an advantage over PGA, as it is less sensitive to high frequency components responsible for variation in pulse shape. Reference [10] compares FGA with PGA in detail. It concludes that compared to time domain methods such as CCM, PGA, the frequency domain method FGA is more robust to variations in pulse shape response from the PMT. It further states that even though FGA is computationally more laborious than PGA, it demonstrated improvement in the FOM. Thus, FGA provides a fast and stable discrimination of neutron and gamma ray from organic scintillators.

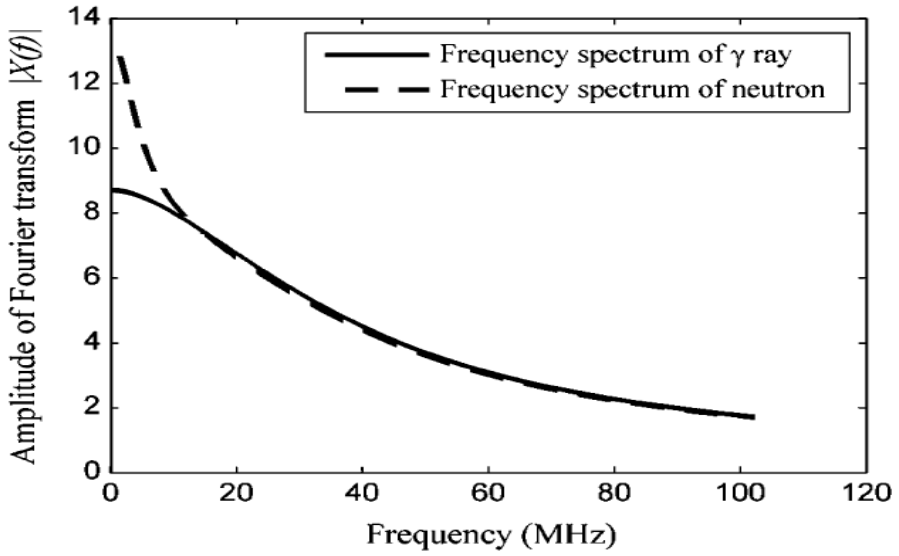

Fig. 2.7 Pulse Shapes of Neutron and Gamma Ray in the Frequency Domain [10].

2.6. Neutron Gamma Model Analysis (NGMA)

As discussed in [8], neutron and gamma ray pulse shapes are modelled and compared with the pulses obtained from the source. The modelling was performed using a set of known gamma ray and neutron pulses. The neutron and gamma ray pulses are distinguished by calculating the difference between the chi-squared (χ^2) for the gamma ray model and neutron model. If the difference $\left(\chi_\gamma^2 - \chi_n^2\right)$ is negative, the pulse is consistent with gamma ray model, and if the difference is positive, it corresponds to the neutron model. The following equations are used in this modeling

$$\chi_\gamma^2 = \sum_{i=1}^{n} \frac{\left(\frac{Am_g}{Ap_u} p_{u(i)} - m_{g(i)}\right)^2}{m_g(i)} \tag{2}$$

$$\chi_n^2 = \sum_{i=1}^{n} \frac{\left(\frac{Am_n}{Ap_u} p_{u(i)} - m_{n(i)}\right)^2}{m_n(i)} \tag{3}$$

$$\Delta\chi^2 = \chi_\gamma^2 - \chi_n^2 \tag{4}$$

Where Ap_u , Am_g and Am_n are the areas of the sampled pulse, the model gamma pulse, and the model neutron pulse, respectively, for the i^{th} sample. Fig. 2.8 shows the discrimination using NGMA. In Fig. 2.8, the lower branch corresponds to gamma events and upper branch corresponds to neutron events.

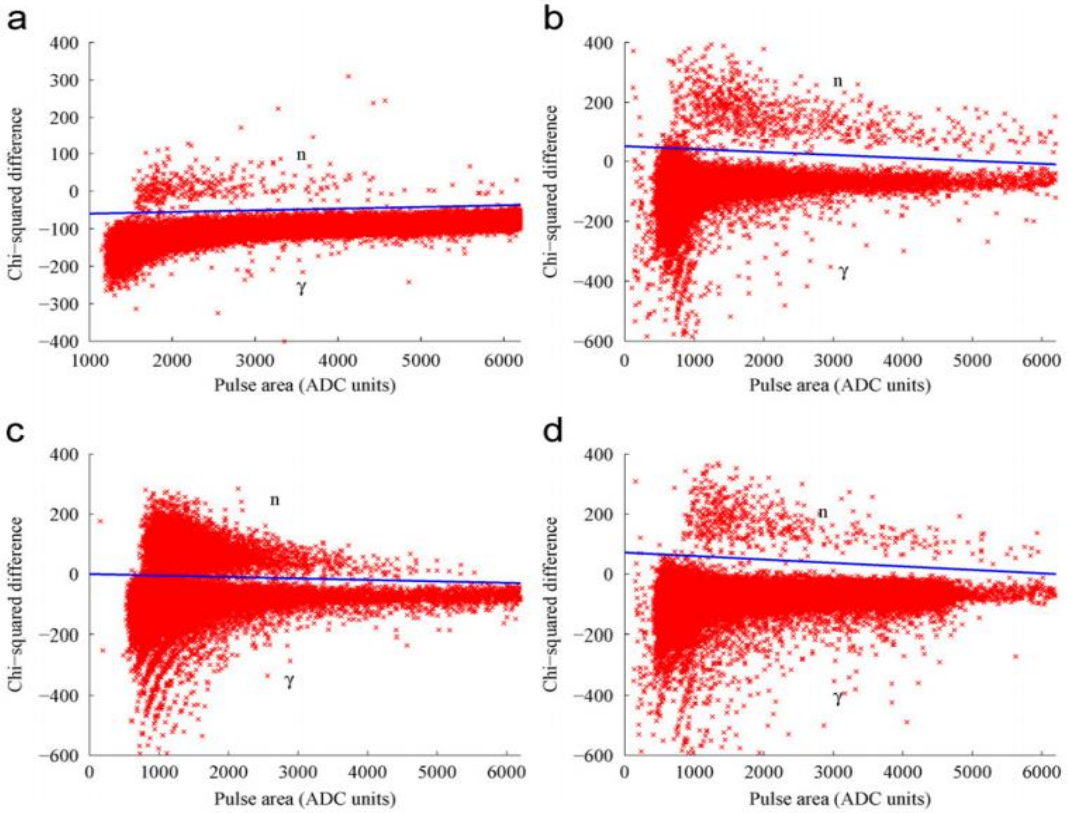

Fig. 2.8 NGMA Technique [8] for a) AmBe*, b)* AmLi*, c)* ^{252}Cf*, d)* PuLi.

2.7. Wavelet Transform Based Method

This technique uses frequency domain features of neutron and gamma pulses for discrimination. It is efficient in neutron-gamma discrimination when compared to the time-domain methods, particularly in the mixed radiation environment with high noise level. The wavelet transform is computed using [11]

$$W_f(a,b) = \langle f, \psi_{a,b} \rangle = \int_{-\infty}^{\infty} f(t) \frac{1}{\sqrt{a}} \varphi^* \left(\frac{t-a}{b} \right) dt \qquad (5)$$

$\psi \in L^2(\boldsymbol{R})$ is the wavelet function with zero average and unit L norm $\|\psi\| = 1$.

Before applying the wavelet transform, we must normalize the input pulses to a unit peak-to-peak signal to remove the dependency on the amplitude of the pulses.

A new function $p(a)$ is computed using the equation below. $p(a)$ is defined as the energy of the wavelet transform of the signal at a specific scale and with different shifts.

$$P(a) = \frac{1}{1+ n_b}\sum_{j=0}^{n_b}\left|W_{\psi}^{s}(a, b_j)\right|^2 \quad (6)$$

This scale function provides a good separation between gamma and neutron pulses. The values of the scale function at two scales are selected as a discrimination parameter. Typically, the selected scale numbers are in a power of 2, which is easily implemented in the discrete wavelet transform. The f1 calculated at one scale value is plotted with f2, which is a division of scale function of scale value 1 and scale value 2.

This method provides better separation capability than PGA and FGA. The gamma–neutron discrimination is obtained by defining simple boundaries, which makes it easy when compared to PGA and FGA where the separation is defined by a nonlinear discriminator line.

2.8. Bipolar Trapezoidal Pulse Shaping Technique

In this method [12], the input pulse is converted to a bipolar trapezoidal pulse using a shaping function. Application of the shaping function on a neutron pulse produces a bipolar trapezoidal pulse with an undistorted top, whereas the gamma pulse produces a bipolar trapezoidal pulse with a distorted top. This difference in the pulse top is used as the discrimination criterion for identifying neutron and gamma pulses. Fig. 2.9 shows the

bipolar trapezoidal waveforms of neutron and gamma pulses.

The shaping function that is composed of rectangular and ramp functions is computed using [12]

$$d[j] = (x[j] - x[j-k] - x[j-l] + x[j-k-l]) - (x[j-(k+l)] - x[j-k-(k+l)] - x[j-l-(k+l)] + x[j-k-l-(k+l)]) \quad (7)$$

$$p[j] = p[j-1] + d[j] \quad (8)$$

$$r[j] = p[j] + (M * d[j]) \quad (9)$$

$$s[j] = s[j-1] + r[j] \quad (10)$$

Where $x(n)$, $p(n)$ and $s(n)$ are zero for $n < 0$.

The duration of the rising edge of the trapezoidal shape is given by the minimum of *k* and *l*; the duration of the flat top of the trapezoid is given by the absolute value of the difference between *k* and *l*; and the duration of the bipolar trapezoid is given by the sum of *k* and *l*. The parameter *M* depends only on the decay time constant of the detector and sampling rate of the digitizer, and is different for neutron and gamma ray pulses. *M* is calculated using [12]

$$M = \tau * (sampling\ rate\ of\ ADC) \quad (11)$$

The *M* parameter of pulse shaping is matched to the decay time of the neutron pulse. As a result, the gamma ray pulse is distorted in the flat top, and the neutron pulse flat top is

undistorted when bipolar pulse shaping is applied. The correlation of the trapezoid flat top with the reference pulse is the main idea of this discrimination algorithm [12].

$$R_{xy} = \sum_{i=1}^{n} \frac{(x_i - \bar{x})(y_i - \bar{y}) s_x s_y}{(n-1)} \quad (12)$$

Where $\overline{x}$ and $\overline{y}$ are the sample means of *X* and *Y;* and s_x and s_y are the sample standard deviations of *X* and *Y*. The correlation coefficient is +1 in the case of a perfect positive increasing linear relationship between the reference pulse and the neutron-gamma ray bipolar trapezoid pulses and –1 in the case of a perfect negative decreasing linear relationship. A correlation coefficient of 0 indicates that the two pulses, the reference and the neutron-gamma pulses, are uncorrelated.

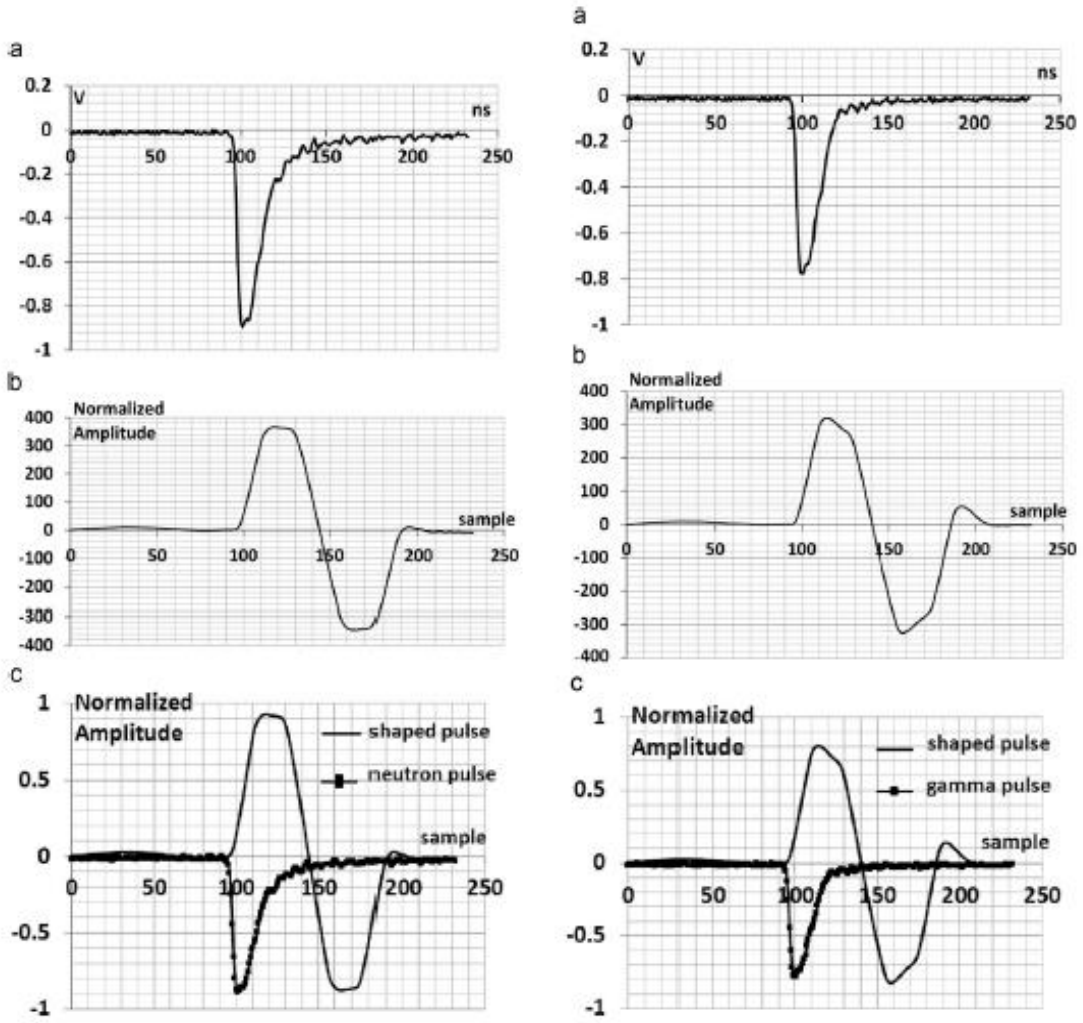

Fig. 2.9 Neutron-Gamma Pulse and Its Corresponding Bipolar Pulses [12].

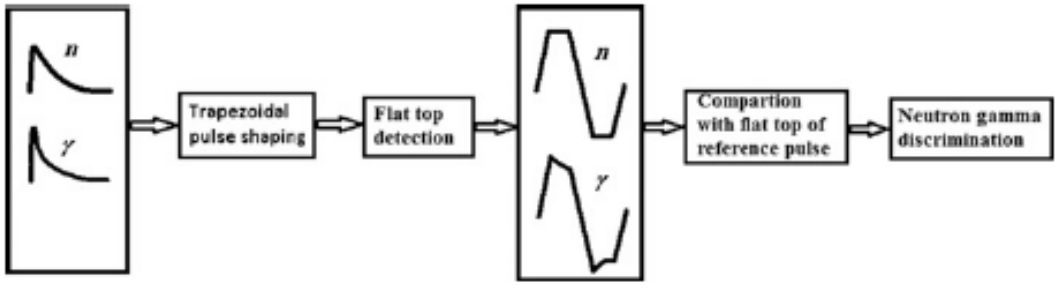

Fig. 2.10 Illustration of Bipolar Trapezoid Pulse Shaping Technique [12].

The shaping function considers factors such as short width pulse for correcting pileup effects and bipolar shaping to eliminate the baseline shift effect and also it eliminates the effect of ballistic deficit. This is the major advantage of this method. Fig. 2.10 outlines the entire procedure.

2.9. Similarity Method

The similarity method can be used to determine the closeness of two pulse shapes, when each pulse is represented by a vector. This technique can be employed in neutron-gamma ray pulse discrimination as the two pulses are different in shapes. The similarity function is defined as [13]

$$S(X,Y) = \frac{(X,Y)}{|X||Y|} = \cos\theta \tag{13}$$

Where X is a pattern vector to be identified and Y is a reference vector or discriminator vector, $|X|$ and $|Y|$ are norms of the vectors X, Y, and θ is the angle between the two vectors. The vector of a pulse is the set of sampled data measured by a digitizer representing the pulse.

By using Eq. (13), the θ value is calculated between the reference vector and the input pulse vector. The reference vector can be either a neutron pulse or a gamma ray pulse. Vector points are chosen from the point where the neutron and gamma ray pulses start showing the difference in the pulse shapes.

2.10. Zero-Crossing Method

This method exploits the property that a neutron pulse decays slower than the gamma ray pulse. In this method, a differentiator-integrator-integrator network is applied to the input pulse to convert it into a bipolar pulse. The difference in the decay time is reflected in the zero-crossing time of this bipolar pulse. The time interval between the start of the bipolar pulse and the time it crosses the zero line is different for neutrons and gamma rays and this has been used as a discrimination criterion for neutron and gamma ray pulse separation.

The start time of the pulse is determined using a parameter digital constant fraction discriminator (CFD). The CFD finds the two sampled points around the threshold, which is a predefined fraction of pulse maximum and then calculates the start time using a linear interpolation as below [14].

$$T_s = x_i + \left(\frac{threshold - |y_i|}{|y_{i+1}| - |y_i|}\right) \tag{14}$$

Where x_i is the time of the sample before threshold, y_i is the signal sample before threshold and y_{i+1} is the signal sample after threshold. Similarly, the zero crossing time can determined by taking two samples before and after zero level, and the zero crossing time is calculated using the above equation. The time delay is calculated between start time and the time it crosses the zero line. This time delay is used to discriminate gamma and neutron pulses. In this method, the integrator and differentiator time constants and CFD plays an important role in neutron-gamma separation so attention must be paid while choosing these values. Reference [14] claims that the zero crossing method

performs better in neutron-gamma ray discrimination than the conventional charge comparison method. Fig. 2.11 shows the procedure using the zero-crossing method.

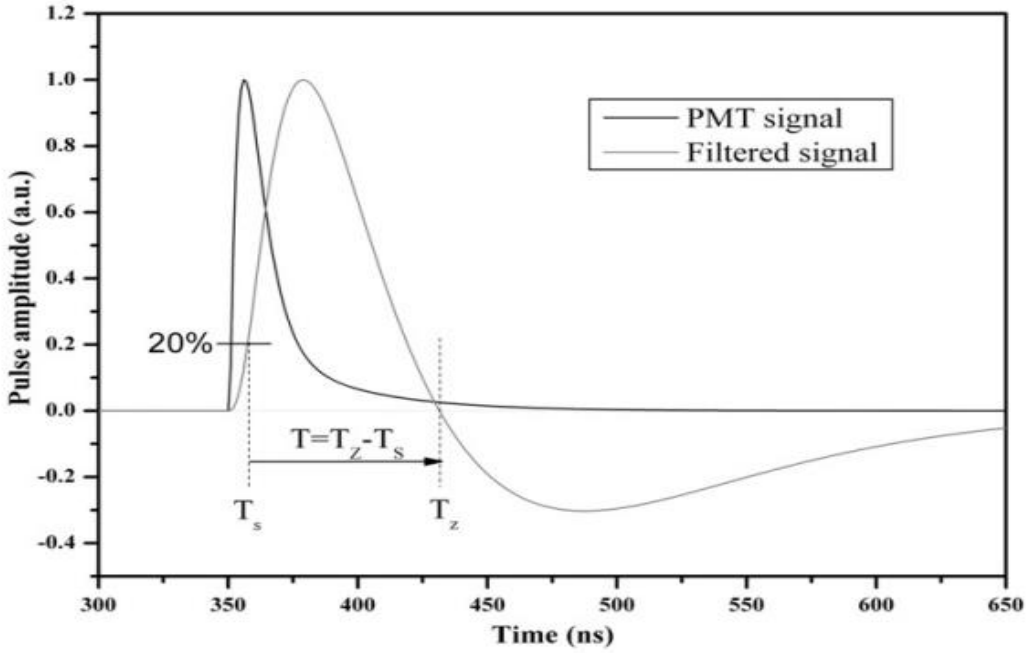

Fig. 2.11 Neutron-Gamma Ray Discrimination Using Zero-Crossing Method [14].

2.11. Correlation Based PSD Technique

Neutron and gamma ray discrimination using the correlation-based technique is based on comparing a sampled pulse from the detector with a template of a neutron or gamma ray pulse. The normalized cross correlation of template u_i with signal y_i is calculated using [15]

$$r_{uy}(k) = \frac{C_{uy}(k)}{\sqrt{C_{uu}(0)\, C_{yy}(0)}} \tag{15}$$

$$c_{uy}\,(k) =$$

$$\begin{cases} \frac{1}{N}\sum_{i=1}^{N-k}(u_i - \bar{u})(y_{i+k} - \bar{y}) \ [k = 0,1, \dots] \\ \frac{1}{N}\sum_{i=1}^{N+k}(y_i - \bar{y})(u_{i-k} - \bar{u}) \ [k = 0,-1, \dots] \end{cases} \quad (16)$$

Where $r_{uy}(k)$ is the normalized cross correlation function; $c_{uy}(k)$ is the cross correlation function of u and y; N is the series length, $\bar{u}$ and $\bar{y}$ are the sample means; k is the lag; $c_{uu}(0)$ and $c_{yy}(0)$ are the sample variance of u_i and y_i .

The NCC reveals the commonalities between the incoming pulse and a reference pulse, so care must be taken in choosing the appropriate template. A significant feature of this technique is that it compares the shapes of the template and input signal but not the amplitudes.

2.11.1. Average Template

This type of template is generated by binning the pulses according to the type and energy, and then averaging the pulses in each bin. The averaged pulses should be normalized and one of the averaged pulses is selected as a template pulse.

2.11.2. Square Template

The square template takes the value of 1 for a given amount of time, also called pulse width and 0 otherwise. The performance of the correlation technique depends on this pulse width, so attention is required in choosing the pulse width. According to reference [15], this technique is easier to implement in FPGA when compared to the average template.

2.12. Metrics to Compare PSD Methods

A few metrics are used to compare PSD methods. One gauge is the Figure Of Merit (FOM), defined as

$$FoM = \frac{S}{FWHM_\gamma + FWHM_n} \tag{17}$$

Where S is the separation between the peaks of the two events, $FWHM_\gamma$ is the full width half maximum (FWHM) of the spread of events classified as gamma rays, and $FWHM_n$ is the FWHM of the spread in the neutron peak. Another is the R-factor, which is the ratio of number of gamma-ray counts to the number of neutron counts as shown in Eq. (18). It is very important in determining the effectiveness of the neutron detector system.

$$R = \frac{\sum_\gamma}{\sum_n} \tag{18}$$

2.13. Comparison of PSD Techniques

Reference [8] compares four of these methods, specifically the CCM, PGA, NGMA and SDCC, for the data produced using a BC501 organic liquid scintillator detector and radiation produced from sources such as AmBe, AmLi, ^{252}Cf, and PuLi. The R-factor and FOM have been used to compare these techniques. Fig. 2.12 [8], shows the results of the analysis. Reference [8] concludes that SDCC is better when compared to the other three PSD methods (PGA, CCM and NGMA) in terms of the FOM.

Table 1
R-factor measurements for mixed radiation fields for each the four different neutron-γ discrimination algorithms investigated in this research.

Source	Method	γ-rays	Neutrons	FWHM (γ)	FWHM (*n*)	FOM	R-factor
Am/Be	PGA	28851	358	2.69 ± 0.01	3.98 ± 0.01	0.831 ± 0.002	81 ± 4
	CCM	28856	353	109 ± 1	170 ± 1	0.753 ± 0.005	82 ± 4
	NGMA	28866	343	41 ± 1	86 ± 1	0.93 ± 0.01	84 ± 5
	SDCC	28852	357	0.39 ± 0.01	0.60 ± 0.01	0.97 ± 0.02	81 ± 4
Am/Li	PGA	49993	716	1.76 ± 0.01	4.01 ± 0.01	0.839 ± 0.003	70 ± 3
	CCM	49887	822	74 ± 1	184 ± 1	0.915 ± 0.006	61 ± 2
	NGMA	49839	870	63 ± 1	201 ± 1	0.806 ± 0.006	57 ± 2
	SDCC	49917	792	0.47 ± 0.01	0.59 ± 0.01	1.05 ± 0.02	63 ± 2
^{252}Cf	PGA	56377	9278	1.08 ± 0.01	1.97 ± 0.01	1.007 ± 0.006	6.08 ± 0.07
	CCM	56373	9282	45 ± 1	66 ± 1	1.04 ± 0.02	6.07 ± 0.07
	NGMA	56698	8957	51 ± 1	98 ± 1	1.05 ± 0.01	6.33 ± 0.07
	SDCC	56394	9261	0.36 ± 0.01	0.45 ± 0.01	1.19 ± 0.02	6.08 ± 0.07
Pu/Li	PGA	65291	513	2.67 ± 0.01	2.98 ± 0.01	0.889 ± 0.003	127 ± 6
	CCM	65265	539	87 ± 1	197 ± 1	0.870 ± 0.006	121 ± 5
	NGMA	65283	521	75 ± 1	180 ± 1	0.855 ± 0.006	125 ± 6
	SDCC	65278	526	0.35 ± 0.01	0.64 ± 0.01	1.14 ± 0.02	124 ± 5

Fig. 2.12 Table Showing the Comparison of Different PSD Methods [8].

CHAPTER 3. EXPERIMENTAL SETUP AND DATA ACQUISITION

3.1. Overview

Scintillation counting which uses the combination of a scintillator and a photomultiplier tube is one of the most commonly used radiation detection methods. It has many advantages as compared to other methods, such as high detection efficiency, fast response time, wide choice of scintillator material and wide area for detection [16]. In this chapter, scintillation based detector system design using CLYC, photomultiplier tube and Xilinx Zynq field programmable gate array (FPGA) is presented.

3.2. Experimental Setup

CLYC, an organic scintillator, is used in this project. The sponsor of this project, Radiation Monitoring Devices (RMD) is a manufacturer of this material. The goal of this project is to design a detector system using CLYC so other scintillation materials were not examined. The CLYC material along with the cylindrical package is placed on the silicone oil coated faceplate of the super-bialkali photomultiplier tube (PMT) supplied by Hamamatsu.

A super-bialkali PMT was selected because RMD demonstrated best response for CLYC using these photomultipliers. Since a PMT is sensitive to external light, it is shielded using plastic tape wrapped around the tube. The PMT has two external connections, one is the signal output and the other is the high voltage supply which is typically -1000 V. A voltage regulation board was designed to convert +5 V to -1000 V. The signal output of

the PMT is connected to the analog-to-digital converter (ADC) board through a differential amplifier. The output of the ADC is differential and it is connected to a Xilinx Zynq system on-chip (SOC) field programmable gate array (FPGA). The Zynq SOC has programmable logic (PL) and processing system (PS). The PL is used to collect the data and the PS, which has an advanced RISC machine (ARM) processor, is used to process the data using PSD algorithms. The block diagram of entire system is shown in Fig. 3.1.

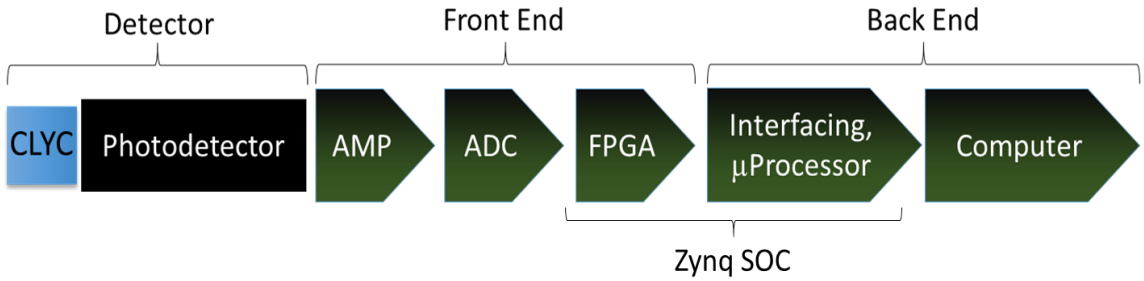

Fig. 3.1 Block Diagram of Detector System.

A photomultiplier is a light signal amplifier. It consists of a faceplate, a photocathode, a focusing electrode, a series of dynodes and an anode sealed into a vacuum tube. Light is detected by the photomultiplier and converted into an electrical signal through a series of steps. First, light, which is collected through the faceplate, excites an electron in the photocathode to produce photoelectrons. These photoelectrons are accelerated and focused on the first dynode by the focusing electrodes. The dynode multiplies the photoelectrons using secondary electron emission. The same step is repeated in the successive dynodes and finally, all the photoelectrons are collected by the anode. The anode then outputs the electron current to the external circuit. Fig. 3.2 shows a PMT. A stable high voltage source is required to operate a PMT. Peripheral devices of a PMT

include a voltage divider circuit for distributing an optimum voltage to each dynode, a housing for external light shield, a shield case for protecting PMT from magnetic or electric fields. Fig. 3.3 shows the socket assemblies that include a PMT socket and a matched divider circuit. The photocathode material used in our PMT is bialkali. It has higher sensitivity to wide range of light and lower dark current.

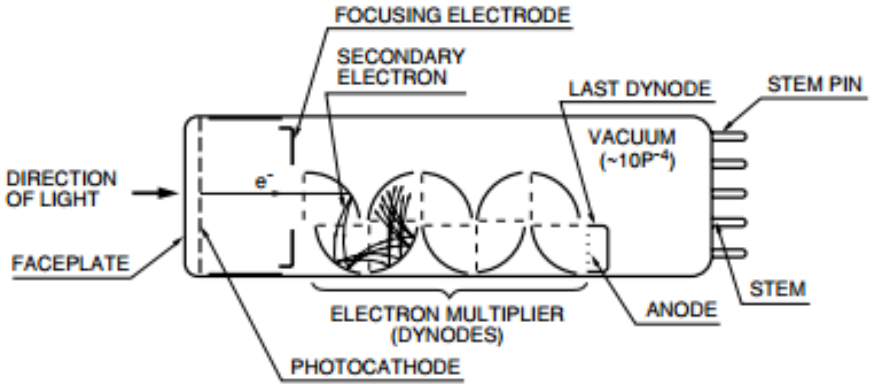

Fig. 3.2 Photomultiplier Tube (PMT) [16].

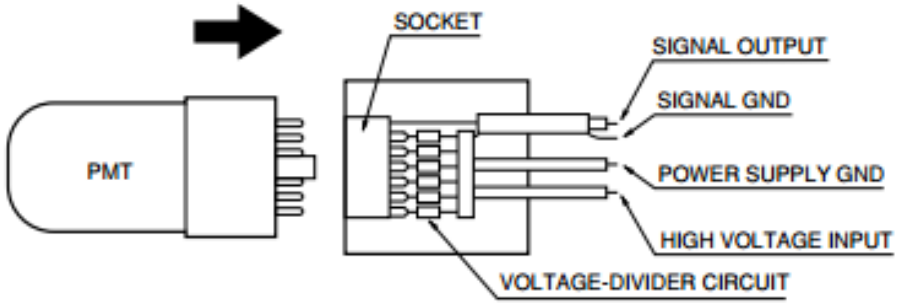

Fig. 3.3 PMT Socket Assembly [16].

The PMT is connected to an analog-to-digital converter (ADC) through a

differential amplifier. The differential amplifier accepts the single ended output signal from the PMT and amplifies it. The ancillary circuits of the differential amplifier consist of input resistors and capacitors to block DC and match impedance. The differential output of the amplified signal is then fed to the ADC. The ADC digitizes the signal and sends it to the Zynq FPGA.

3.3. Interfacing ADC to ZYNQ FPGA

The digital components of the system consist of the ADC, a MicroZed board and an interface board to the MicroZed board. A picture of the MicroZed board, chip carrier board, and interface board is shown in Fig. 3.4. The ADC is mounted on the interface board, sandwiched with the amplifier board. Digital signals from the interconnect board are sent into the chip carrier board with ribbon cable, which connects to the MicroZed via a mezzanine connector. The chip carrier board is used for rapid development of the system, where it is used to ensure that the power and connections to the MicroZed board are done correctly. The voltage regulators supply the correct voltages.

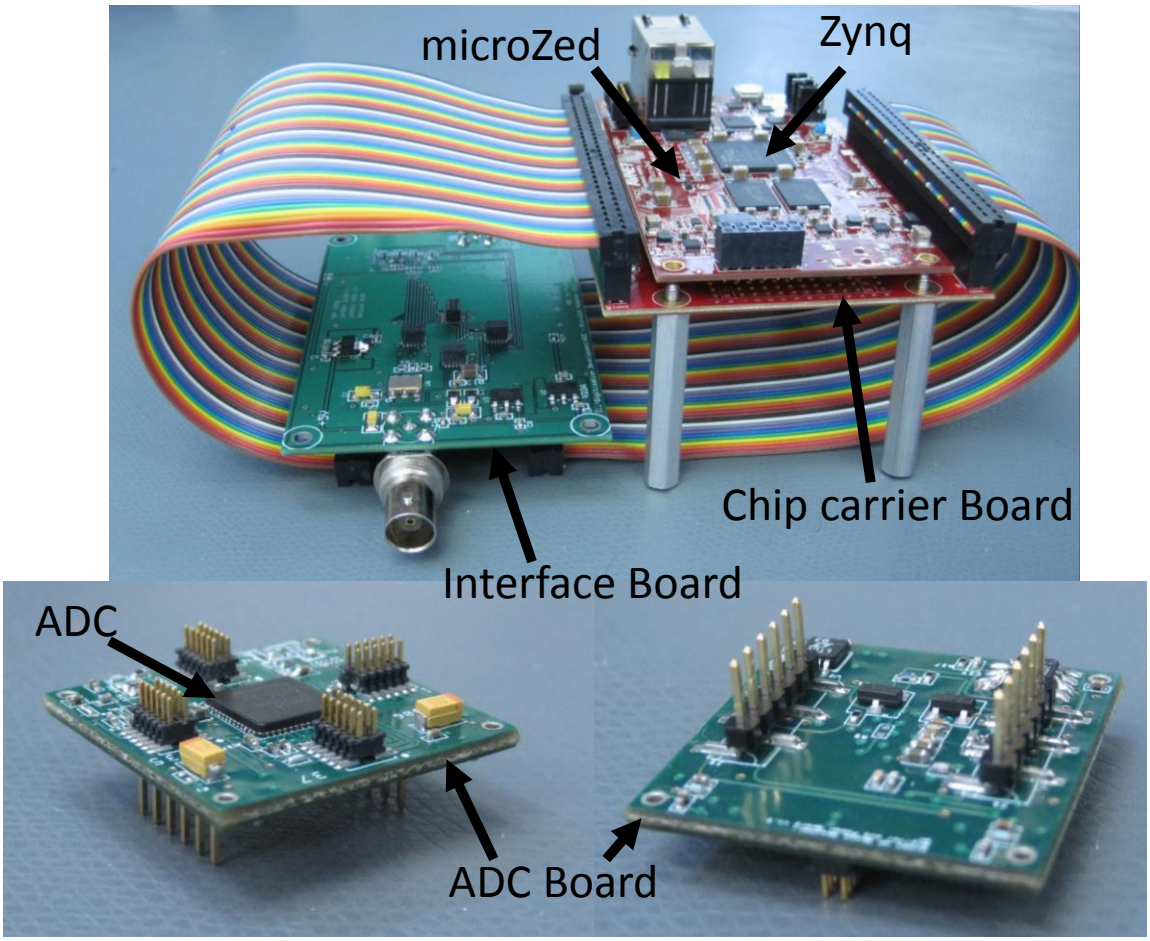

Fig. 3.4 Interface Board That Connects the ADC to FPGA Through a Chip Carrier Board.

3.4. Data Acquisition

To acquire actual neutron and gamma ray pulses for analysis, the detector system discussed above with super bialkali photomultiplier tube (PMT) and CLYC crystal was exposed to neutrons from either a ^{252}Cf or an AmBe source located a few centimeters from the crystal. A ^{137}Cs or ^{22}Na or ^{57}Co source was also placed above the crystal to subject it to additional gamma rays. The distance from the gamma source to the crystal

was varied to control the event rate detected, while the position of the neutron source was fixed. As summarized in Table 3.1, nine data sets were acquired for about 0.3 s to 1.4 s each using a sampling frequency of 250 MSPS (mega samples per second). From the mixed radiation environment consisting of ^{137}Cs and ^{252}Cf, the neutron and gamma pulses were obtained at event rates from 1 kHz to 5.3 MHz. In another experiment, 15 data sets summarized in Table 3.2 were acquired for about 0.3 s to 1.4 s each using a sampling frequency of 250 MSPS. In data set II, three sources are used. Some of the data were acquired using two gamma rays sources and one neutron source, and some of them using three gamma ray sources. In both the cases only one gamma ray source was moved to control the event rate. At high event rates, above 600 kHz, neutron and gamma ray pulses are distorted because of the significant presence of pileup.

Table 3.1 Data Set I Used for Cross Correlation Analysis

File	Event Rate (kHz)	Gamma Source	Neutron Source	Gamma Source to CLYC Distance	Data Use for NCC Analysis
1	5	—	AmBe	—	ref. neutron
2	10	^{137}Cs	—	16.5 inch	ref. gamma
3	1	^{137}Cs	^{252}Cf	—	n & γ pulses
4	60	^{137}Cs	^{252}Cf	7.5 inch	n & γ pulses
5	120	^{137}Cs	^{252}Cf	11.75 inch	n & γ pulses
6	180	^{137}Cs	^{252}Cf	4.50 inch	n & γ pulses
7	600	^{137}Cs	^{252}Cf	3.25 inch	n & γ pulses
8	2400	^{137}Cs	^{252}Cf	2.25 inch	n & γ pulses
9	5300	^{137}Cs	^{252}Cf	1.25 inch	n & γ pulses

Table 3.2 Data Set II Used for Cross Correlation Analysis

File	Event Rate (kHz)	Gamma Source 1	Gamma Source 2	Gamma Source 3	Neutron Source	Gamma Source to CLYC Distance	Data Use for NCC Analysis
1	1	^{22}Na	^{137}Cs	—	—	—	γ pulses
2	6	^{22}Na	^{137}Cs	—	AmBe	15.625 inch	n & γ pulses
3	13	^{22}Na	^{137}Cs	—	AmBe	9 inch	n & γ pulses
4	92	^{22}Na	^{137}Cs	—	AmBe	2 inch	n & γ pulses
5	191	^{22}Na	^{137}Cs	—	AmBe	1 inch	n & γ pulses
6	370	^{22}Na	^{137}Cs	—	AmBe	0.5 inch	n & γ pulses
7	583	^{22}Na	^{137}Cs	—	AmBe		n & γ pulses
8	1390	^{22}Na	^{137}Cs	—	AmBe		n & γ pulses
9	1660	^{22}Na	^{137}Cs	—	AmBe		n & γ pulses
10	531	^{22}Na	^{137}Cs	^{57}Co	—	—	γ pulses
11	736	^{22}Na	^{137}Cs	^{57}Co	—	1.5 inch	γ pulses
12	948	^{22}Na	^{137}Cs	^{57}Co	—	1.125 inch	γ pulses
13	1100	^{22}Na	^{137}Cs	^{57}Co	—	0.875 inch	γ pulses
14	1390	^{22}Na	^{137}Cs	^{57}Co	—	0.625 inch	γ pulses
15	1650	^{22}Na	^{137}Cs	^{57}Co	—	0.125 inch	γ pulses

CHAPTER 4. PULSE SHAPE DISCRIMINATION THEORY

In this chapter, features of neutron and gamma ray pulse shapes and the cross correlations between them will be presented. Also, issues such as pile up and baseline shift will be discussed.

4.1. Features of Neutron and Gamma Ray Pulses

Neutron pulses have a short, blunt peak and a long decay time. A typical neutron pulse is shown in Fig. 4.1. On the other hand, gamma ray pulses have a tall, sharp peak and short decay time as shown in Fig. 4.2. The pulse shape of the neutron and gamma rays are dependent on the type of scintillator used. The pulse amplitude also depends on the radiation energy. These unique characteristics that define neutron and gamma ray pulses can be used to discriminate each other. However, it is difficult to acquire perfect neutron and gamma ray pulses using a detector system, as the noise from the electronics will distort the pulses, particularly at high event rates. This forces the scientific community to use different PSD techniques discussed in Chapter 2 to distinguish neutrons and gamma rays. One among the techniques, the NCC will be discussed in detail.

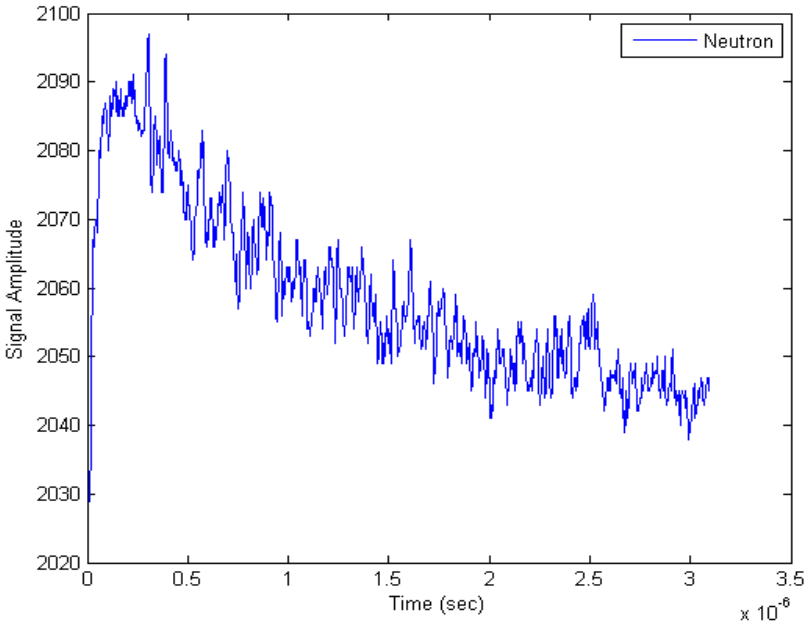

Fig. 4.1 Neutron Pulse from CLYC.

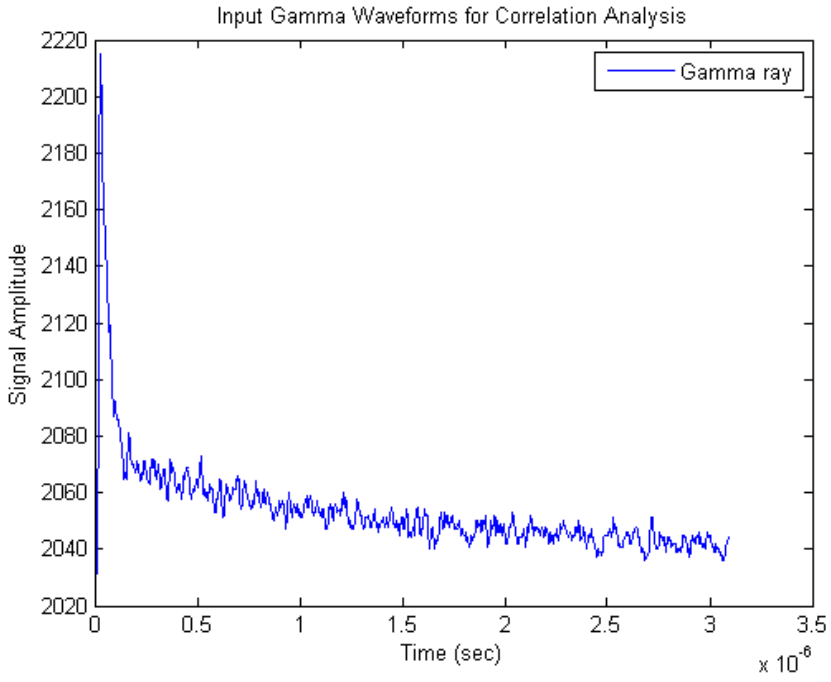

Fig. 4.2 Gamma Ray Pulse from CLYC.

4.2. Normalized Cross Correlation

As discussed in Chapter 2, the normalized cross correlation of template u_i with signal y_i is calculated using [17]

$$r_{uy}(k) = \frac{C_{uy}(k)}{\sqrt{C_{uu}(0)\, C_{yy}(0)}} \tag{19}$$

$$c_{uy}\,(k) = \begin{cases} \frac{1}{N}\sum_{i=1}^{N-k}(u_i - \bar{u})(y_{i+k} - \bar{y}) \; [k = 0,1, \dots] \\ \frac{1}{N}\sum_{i=1}^{N+k}(y_i - \bar{y})(u_{i-k} - \bar{u}) \; [k = 0,-1, \dots] \end{cases} \tag{20}$$

Where $r_{uy}(k)$ is the normalized cross correlation function; $c_{uy}(k)$ is the cross correlation function of *u* and *y*; *N* is the series length, $\bar{u}$ and $\bar{y}$ are the sample means; *k* is the lag; $c_{uu}(0)$ and $c_{yy}(0)$ are the sample variance of u_i and y_i . If template u_i and signal y_i are one and the same, then the output $r_{uy}(k)$ is called the auto correlation. The normalized cross correlation normalizes the correlation values so that the correlation equals unity at zero lag. Normalized cross correlation values range from -1 to 1. Identical signals have correlation value of 1. A correlation value of -1 signifies that two signals are anti correlated. There are permutations of Eq. (19), including

$$r_{uy,biased}(k) = \frac{C_{uy}(k)}{N} \tag{21}$$

$$r_{uy,unbiased}(k) = \frac{C_{uy}(k)}{N-|m|} \tag{22}$$

Where $r_{uy,biased}(k)$ gives the biased estimate of cross correlation values, and $r_{uy,unbiased}(k)$ gives the unbiased estimate of cross correlation values. For the NCC analysis in the project, Eq. (19) is used. Eq. (21) will give similar results as Eq. (19) if the input pulses have the mean subtracted.

A neutron pulse shows a very high NCC value (> 0.8), particularly at zero lag when correlated with another neutron pulse. Fig. 4.3 shows the neutron pulse to neutron pulse correlation. The NCC was calculated for 20 positive lags and 20 negative lags. Any number of samples (*N*) can be selected to depict a neutron or gamma ray pulse. However, *N* should be such that the pulse has all the characteristics of a neutron or gamma ray pulse. In this project, the number of samples (*N*) taken to depict any pulse is 773.

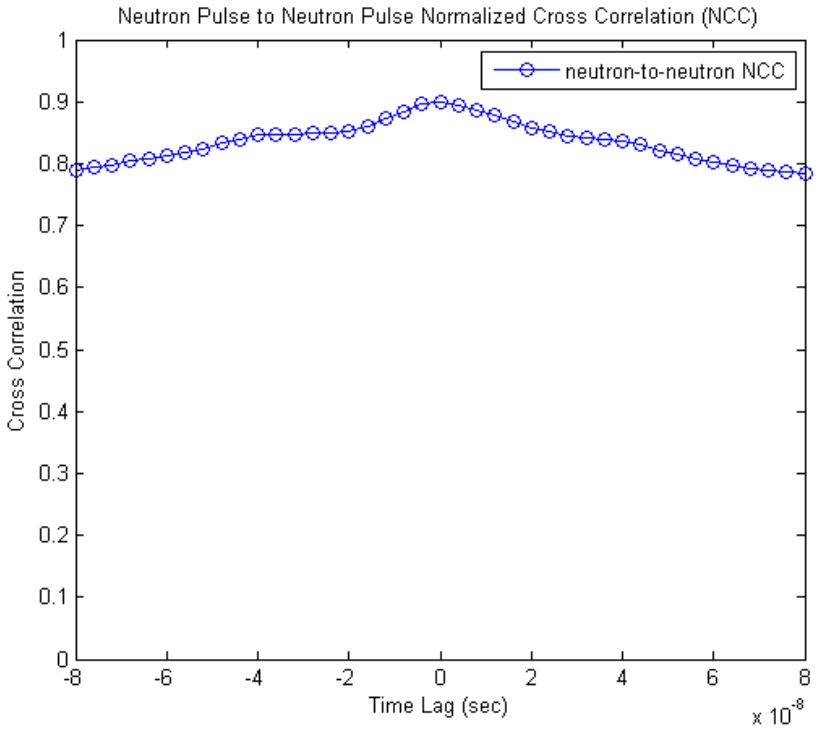

Fig. 4.3 Neutron Pulse Cross Correlated with Another Neutron Pulse.

As shown in Fig. 4.3, the neutron-to-neutron NCC plot exhibits a very high NCC at zero lag and slightly decreases both in the positive and negative lags. However, overall it retains a NCC value higher than 0.8. Similarly, a gamma ray pulse shows highest NCC value (> 0.8) at zero lag when cross correlated with another gamma ray pulse as shown in

Fig. 4.4. However, the NCC value decreases significantly for both positive and negative lags. In both the cases, the two pulses used for correlation have similar features so they are expected to have a near unity NCC value at zero lag.

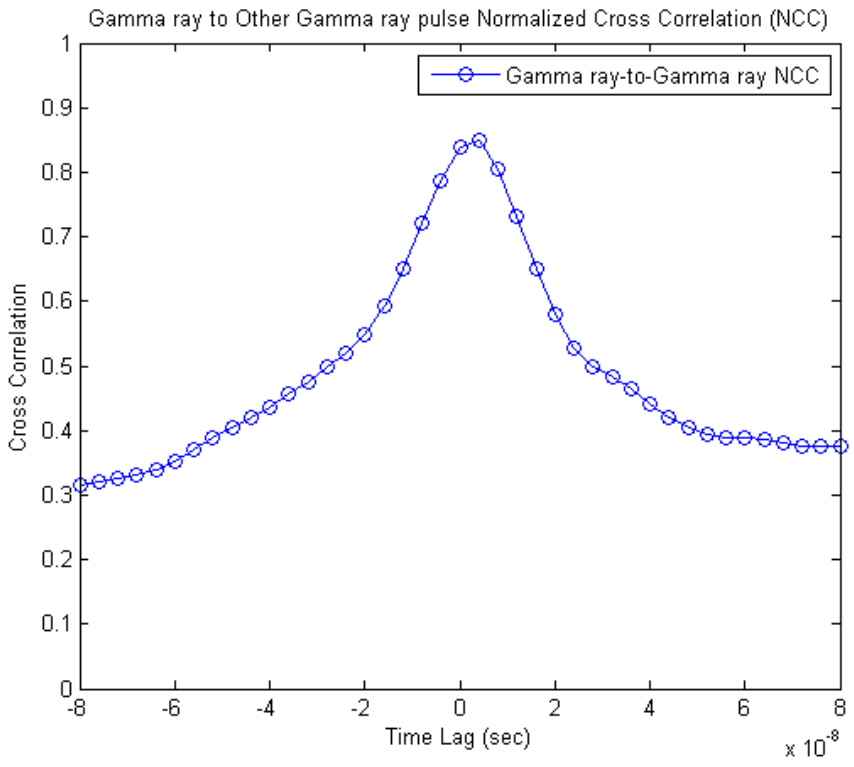

Fig. 4.4 Gamma Ray Pulse Cross Correlated with Another Gamma Ray Pulse.

On the other hand, a neutron pulse when correlated with a gamma ray pulse shows reduced NCC value (< 0.7), particularly at zero lag. Fig. 4.5 shows the neutron pulse to gamma ray pulse correlation. As shown in Fig. 4.5, the NCC values drop significantly from the zero lag as the lag increases in the positive direction. However, NCC values stay constant for negative lags. The opposite is seen when a gamma ray pulse is correlated with neutron pulse as shown in Fig. 4.6. Here, the NCC values stay constant for positive

lags when compared to zero lag and decrease significantly for negative lags near the zero lag and then stay low and constant for further increase in negative lags. It is to be noted here that the neutron-to-gamma ray correlation plot is not the same as, but rather a mirror image of, the gamma ray-to-neutron correlation plot as shown in equation below.

$$C_{uy}(k) = C_{yu}(-k) \tag{23}$$

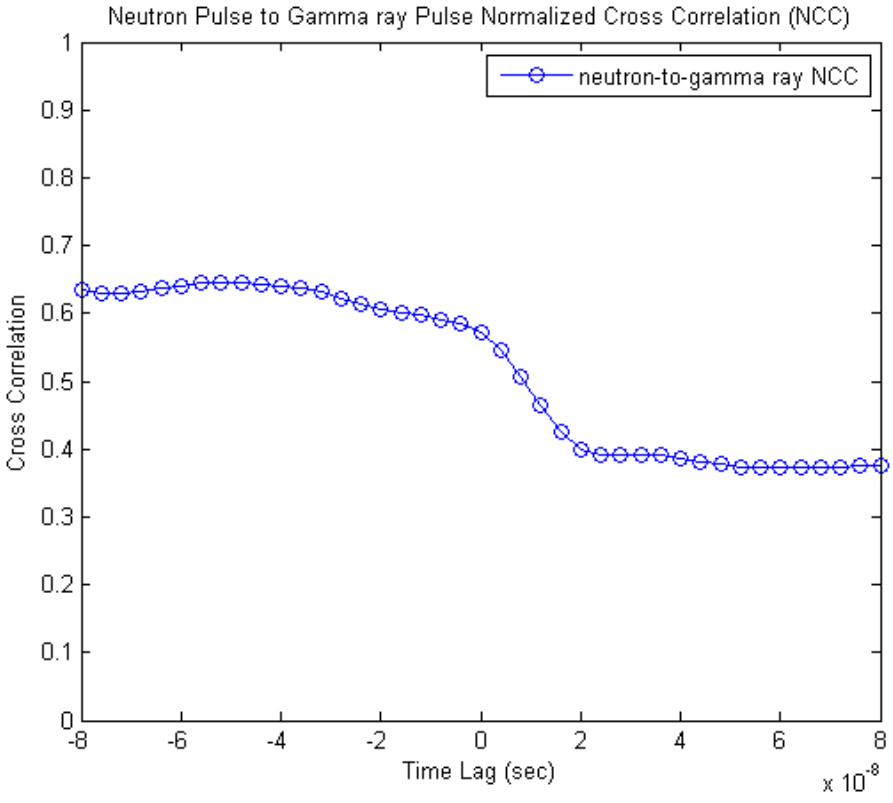

Fig. 4.5 Neutron Pulse Cross Correlated with Gamma Ray Pulse.

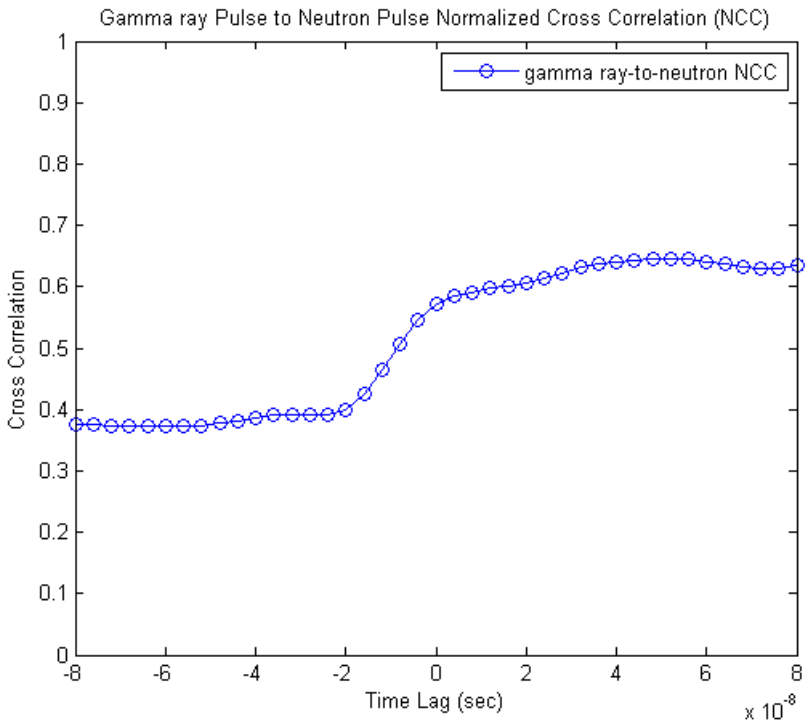

Fig. 4.6 Gamma Ray Pulse Cross Correlated with Neutron Pulse.

The difference in the neutron-to-neutron correlation plot and the neutron-to-gamma correlation plot, or, the gamma ray-to-gamma ray correlation plot and the gamma ray-to-neutron correlation plot give confidence that this method could be used to discriminate neutron and gamma ray pulses. Further analysis is required to demonstrate whether this method works well.

The best neutron pulses and gamma ray pulses, which do not have any noise and have the features described in Section 4.1, from all data files in Table 3.1 are taken and cross correlated with the template gamma ray and neutron pulses. Fig. 4.7 shows the NCC plots of the template neutron to a neutron and the template neutron to six different gamma ray

pulses. As discussed above, the template neutron-to-neutron cross correlation showed a large value at zero lag and stayed high for positive lags whereas all the template neutron-to-gamma ray cross correlations are low at zero lag and fall sharply for positive lags after zero lag and then maintain low values for further increases in positive lags. This kind of trend differentiates neutron and gamma ray pulses. Fig. 4.7 is intended to verify the template neutron-to-gamma ray cross correlation is consistent across any gamma ray pulse that has typical features of gamma ray pulse discussed above. Fig. 4.8 shows the NCC plots of one template neutron to a gamma ray and the template neutron to six neutron pulses. As expected, neutron-to-neutron cross correlations are high from zero lag to the end of the positive lags whereas neutron-to-gamma ray cross correlations fall sharply after zero lag. This confirms the similar behavior among neutron pulses taken from different data sets when cross correlated with the template neutron pulse.

Similar analysis is also done with template gamma ray pulse. Fig. 4.9 shows NCC plots of the template gamma ray to a gamma ray and the template gamma ray to six different neutron pulses. As discussed above, the template gamma ray-to-gamma ray cross correlations show a NCC value of 1 at zero lag and decreases as lags increase in both positive and negative directions, whereas template gamma ray-to-neutron cross correlations start small and increase approaching zero lag, attain maximum value at zero lag and maintain the same value as lag increases in the positive direction. The maximum NCC value exhibited by all the gamma ray-to-neutron cross correlation plots is less than 0.7, thus differentiating neutron and gamma ray pulses. Fig. 4.10 shows NCC plots of the

template gamma ray to a neutron cross correlation and the template gamma ray to six different gamma ray pulses taken from all the data files in Table 3.1. It is reinforced from Fig. 4.10 that all template gamma ray-to-gamma ray cross correlations exhibit a similar trend that is high NCC value > 0.7 at or near zero lag, whereas the template gamma ray-to-neutron cross correlation plot shows a NCC value < 0.7 at zero lag. There is shift in the peak of gamma ray-to-gamma ray cross correlation, this is because of shift in the rising edge of the cross correlated pulses. This explains that a template gamma ray can also be used to discriminate neutron and gamma ray pulses. This confirms the trend what was seen with cross correlation of neutron and gamma ray pulses with template neutron pulse.

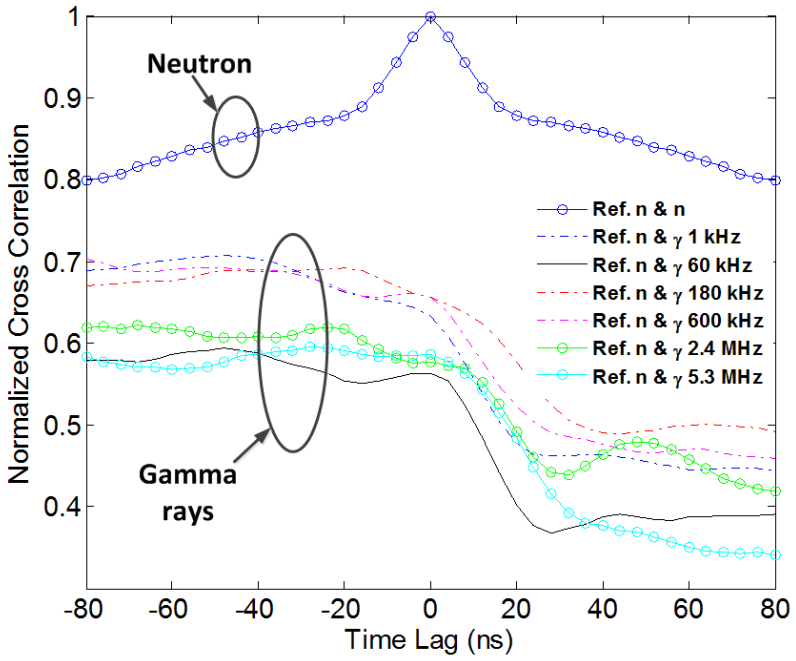

Fig. 4.7 NCC of the Neutron Pulse Template with a Gamma Pulse and Other Neutron Pulses Acquired at Different Event Rates.

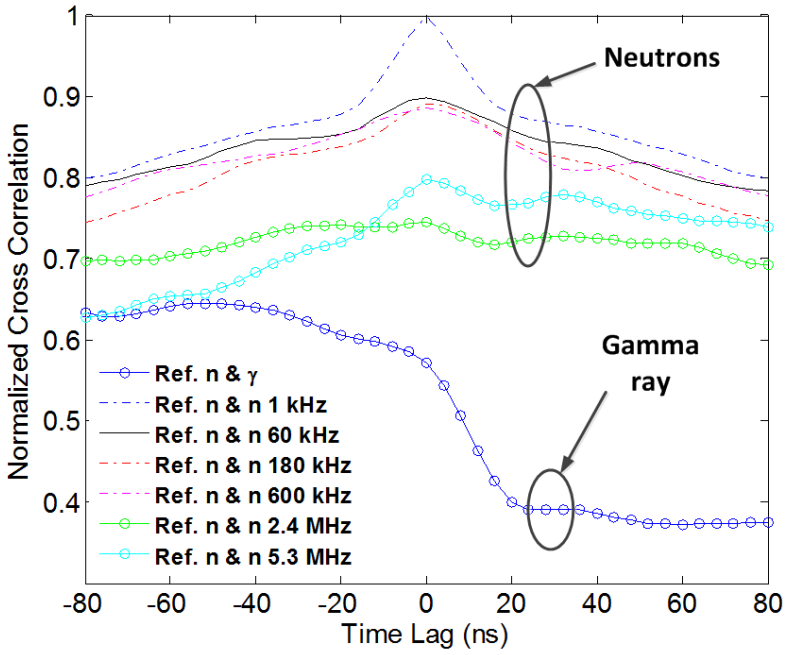

Fig. 4.8 NCC Of The Neutron Pulse Template with a Neutron Pulse and Gamma Pulses Obtained at Different Event Rates.

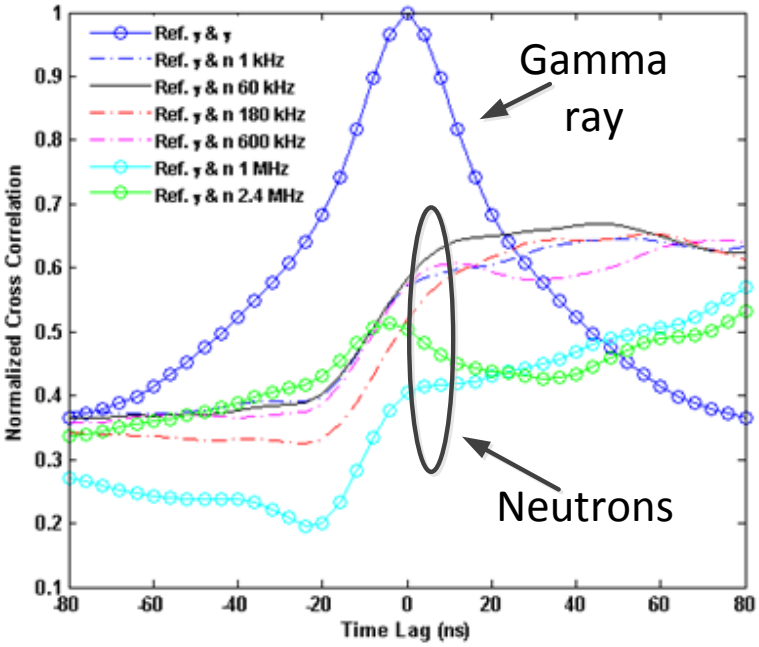

Fig. 4.9 NCC Of The Gamma Ray Pulse Template with a Gamma Pulse and Neutron Pulses Obtained at Different Event Rates.

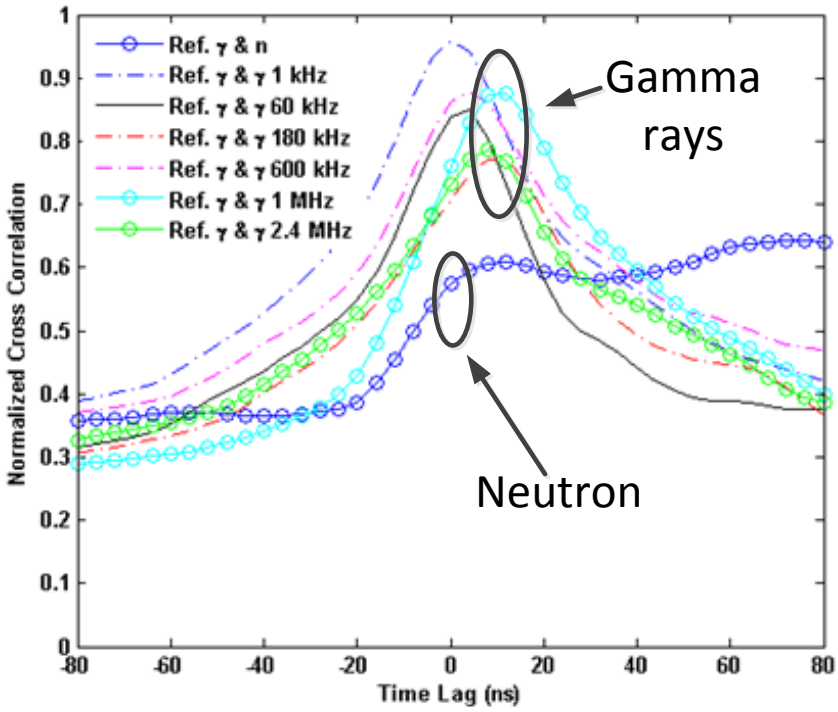

Fig. 4.10 NCC of the Gamma Ray Pulse Template with a Neutron Pulse and Other Gamma Ray Pulses Acquired at Different Event Rates.

4.3. Analytical Modelling

In the mixed radiation environment where neutron and gamma rays are present, one each of the neutron and gamma ray pulses is preselected and thereafter correlated with neutron and gamma ray pulses sampled from the mixed radiation. The predetermined pulse is called a template pulse. Rather than use a template which is a sampled pulse that retains features such as noise, a better reference signal for NCC analysis was sought by creating a numerical model. The neutron and gamma templates required for NCC can be modeled using Marrone's equation [10], [19]

$$P(t) = A(e^{\frac{-(t-t_0)}{\theta}} - e^{\frac{-(t-t_0)}{\lambda_s}} + Be^{\frac{-(t-t_0)}{\lambda_l}}) \quad (24)$$

Where *A* and *B* are amplitudes of the short and long decay components, respectively; θ is the decay time constant; λ_l and λ_s are the time constants for the long and short decay components, respectively; and t_0 is a time reference for the start of the signal. Equation (24) can be used to represent the reference pulse for any detector. For instance, Liu et al. employed Equation (24) to model neutron and gamma ray pulses for a liquid scintillation detector [10].

Marrone employed an ensemble of pulses to determine the fitting parameters, while in our work, one particular neutron and one specific gamma ray pulse were utilized to create the reference models. The template neutron and gamma pulses from the CLYC detector and their reference models created using Matlab curve fitting tool are shown in Fig. 4.11 and Fig. 4.12, and Table 4.1 lists the fitted constants. The values of neutron and gamma ray pulses are obtained by manually adjusting the initial values of the parameters obtained from Matlab curve fitting tool to match the template pulses with the reference pulses.

Table 4.1 Parameters Obtained Using Marrone Equation Fit to Data

Pulse	*A*	*B*	λ_l (ns)	λ_s (ns)	t_0 (ns)	θ (ns)
Gamma ray	9878	4.375×10^{-3}	725.8	5.425	2.613	5.601
Neutron	43.79	0.5432	1231.1	5.004	144	4.999

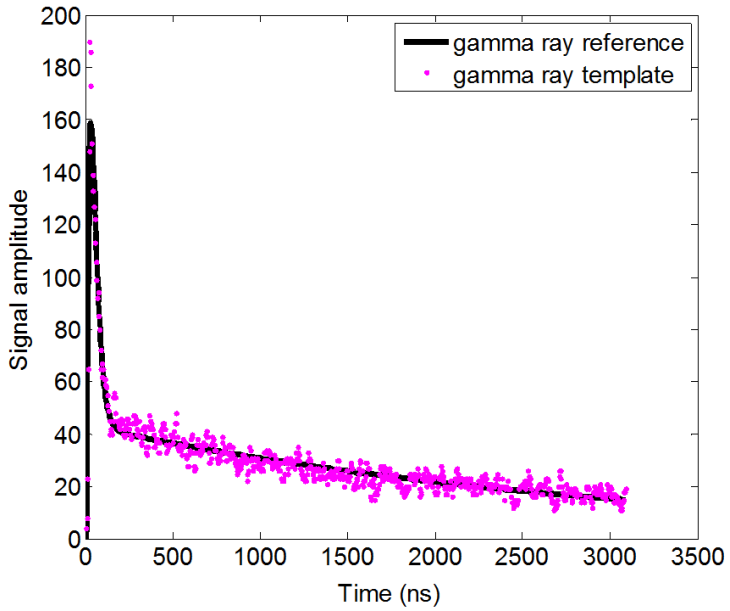

Fig. 4.11 Experimentally Obtained Gamma Ray Template Pulse and Its Reference Model.

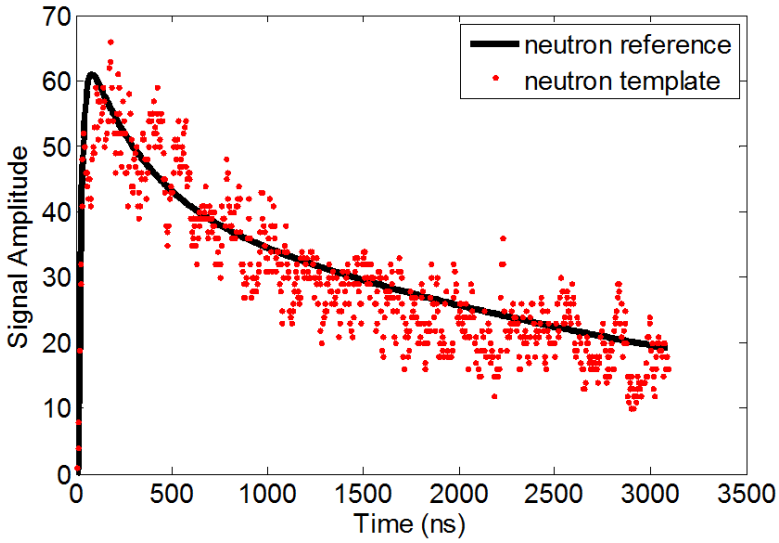

Fig. 4.12 Experimentally Obtained Neutron Template Pulse and Its Reference Model.

These fitted neutron and gamma pulses are deemed ideal and are cross correlated with one another to obtain the ideal normalized cross correlation plots of gamma ray-to-

gamma ray, gamma ray-to-neutron, neutron-to-gamma ray and neutron-to-neutron.

Fig. 4.13 plots the auto correlation of the modelled neutron with itself and the auto correlation of the experimentally obtained neutron pulse with the same experimentally obtained neutron pulse. Fig. 4.14 graphs the auto correlation of the modelled gamma ray with itself and the auto correlation of the experimentally obtained gamma ray with the same experimentally obtained gamma ray pulse. Fig. 4.15 shows the cross correlation of the modelled gamma ray with the modelled neutron and cross correlation of the experimentally obtained gamma ray with the experimentally obtained neutron pulse. The cross correlation of the modelled neutron with modelled gamma ray plot will be a mirror image of Fig. 4.16 according to Eq. (23). Similarly, the cross correlation of the experimentally obtained neutron with the experimentally obtained gamma ray will be a mirror image of Fig. 4.16. as per Eq. (23). It is clear from Fig. 4.13, Fig. 4.14, Fig. 4.15 and Fig. 4.16 that the auto and cross correlations of modelled pulses are very close to those of experimentally obtained pulses. This enables us to use the modelled pulses for the rest of the analyses. For the remainder of the NCC analyses, the modelled neutron and gamma ray pulses will be used and they are referred to as reference pulses. The experimentally obtained pulses are referred to as template pulses. Fig. 4.17 shows the NCC plot of the modelled pulse with the experimentally obtained pulse for neutron-to-neutron, gamma-to-neutron and gamma-to-gamma. It also reveals that neutron-to-neutron and gamma-to-neutron correlations are different, and this is the basis for differentiating neutron and gamma pulses.

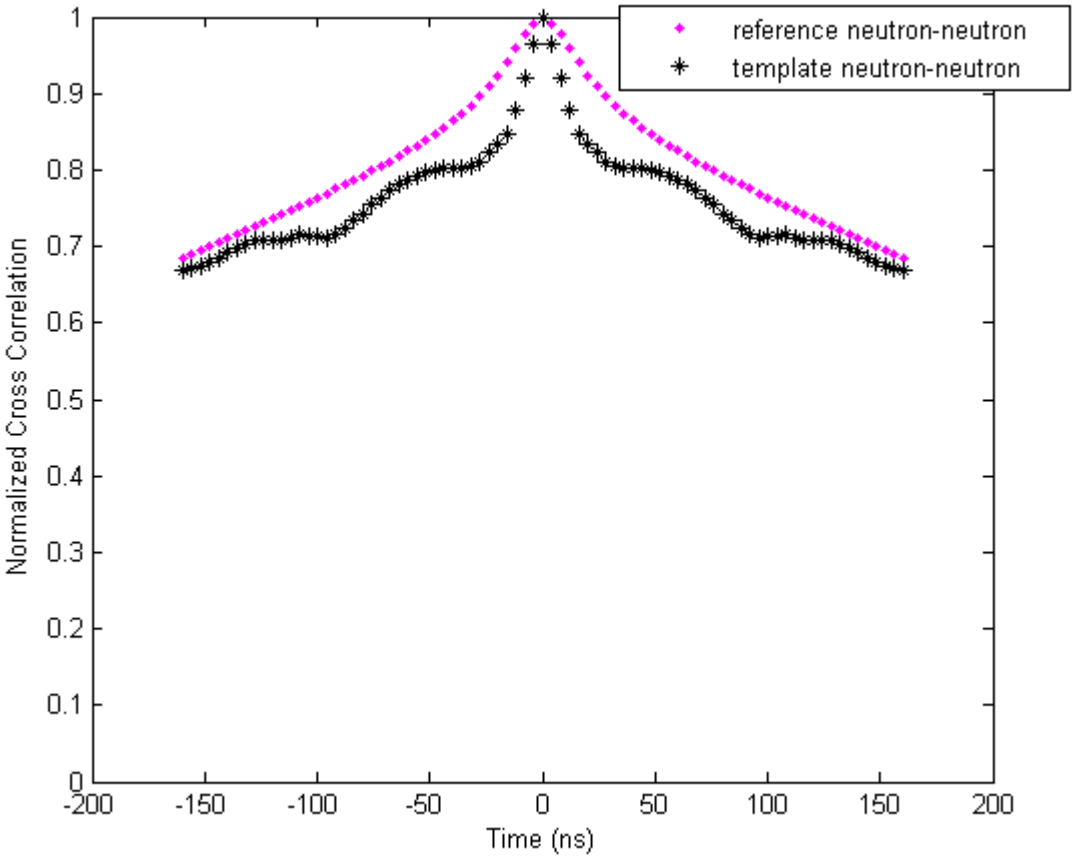

Fig. 4.13 NCC Plot of Experimentally Neutron Pulses and Modelled Neutron Pulses.

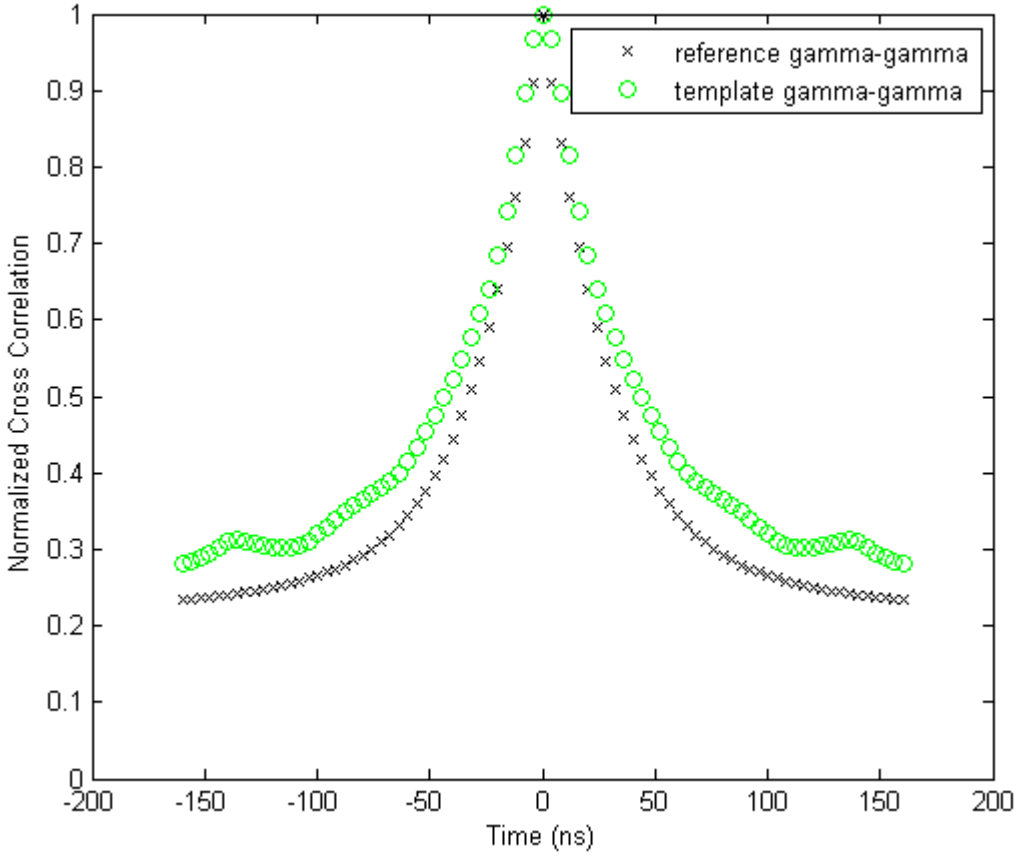

Fig. 4.14 NCC Plot of Experimentally Gamma Ray Pulses and Modelled Gamma Ray Pulses.

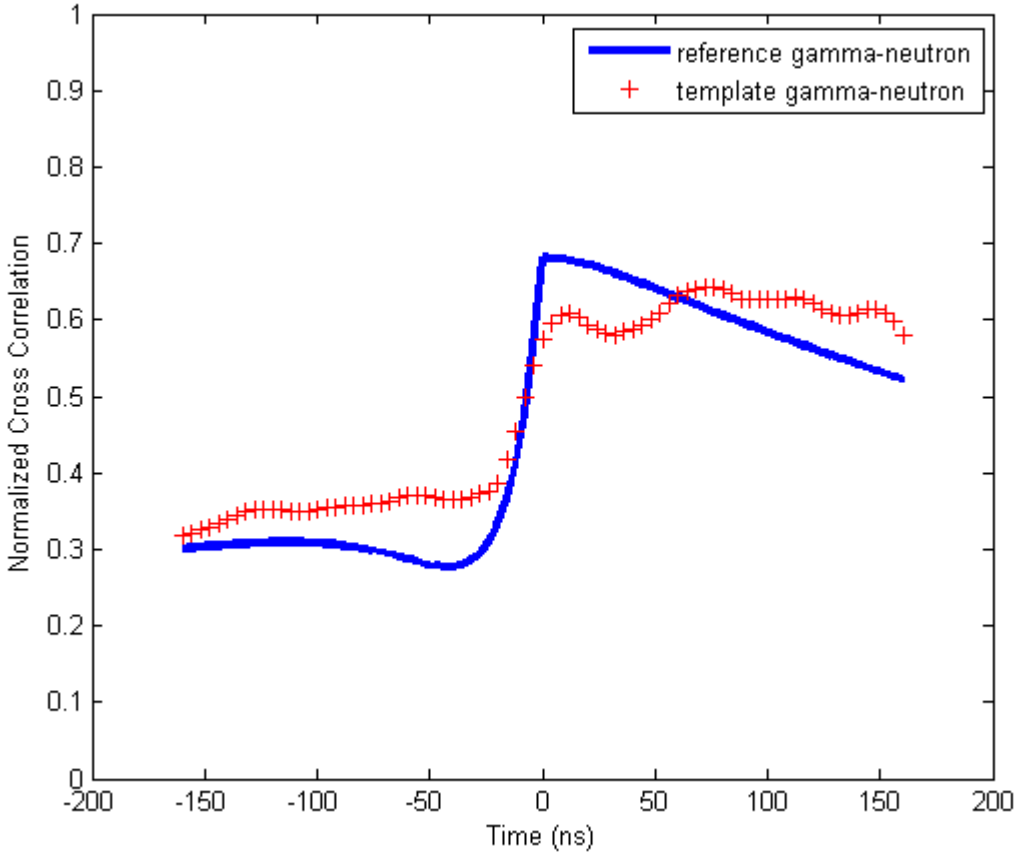

Fig. 4.15 NCC Plot of Experimentally Gamma Ray and Neutron Pulses and Modelled Gamma Ray and Neutron Pulses.

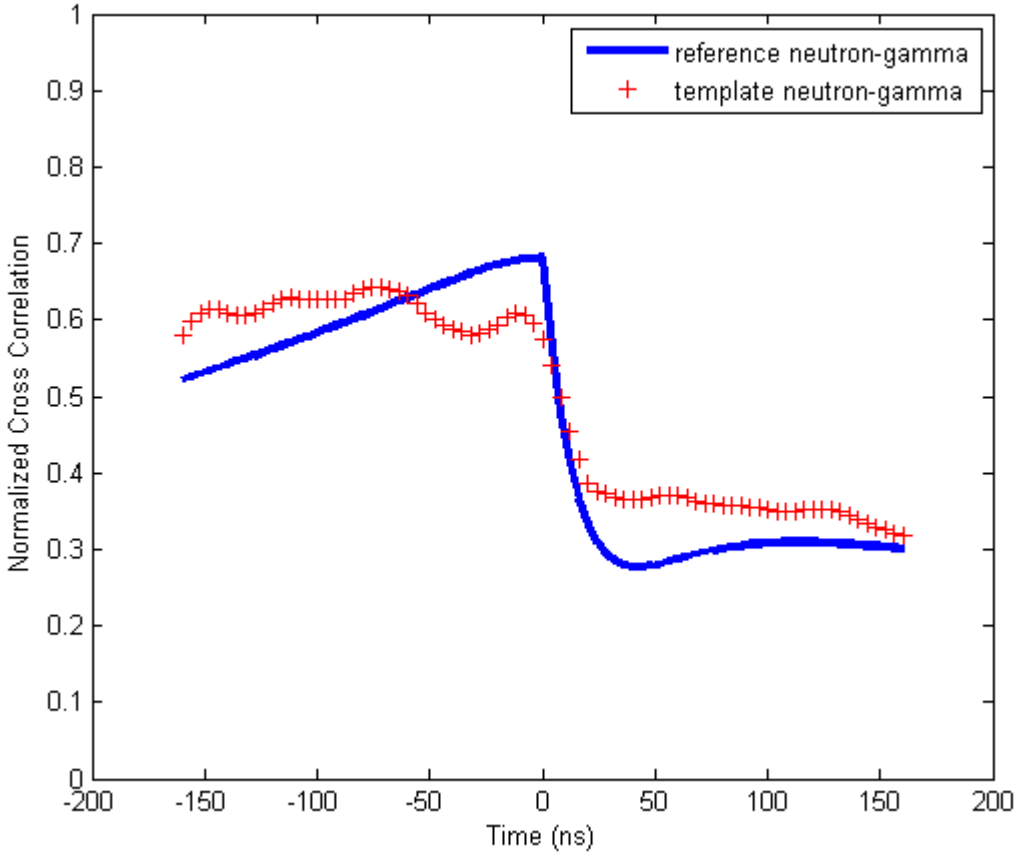

Fig. 4.16 NCC Plot of Experimentally Neutron and Gamma Ray Pulses and Modelled Neutron and Gamma Ray Pulses.

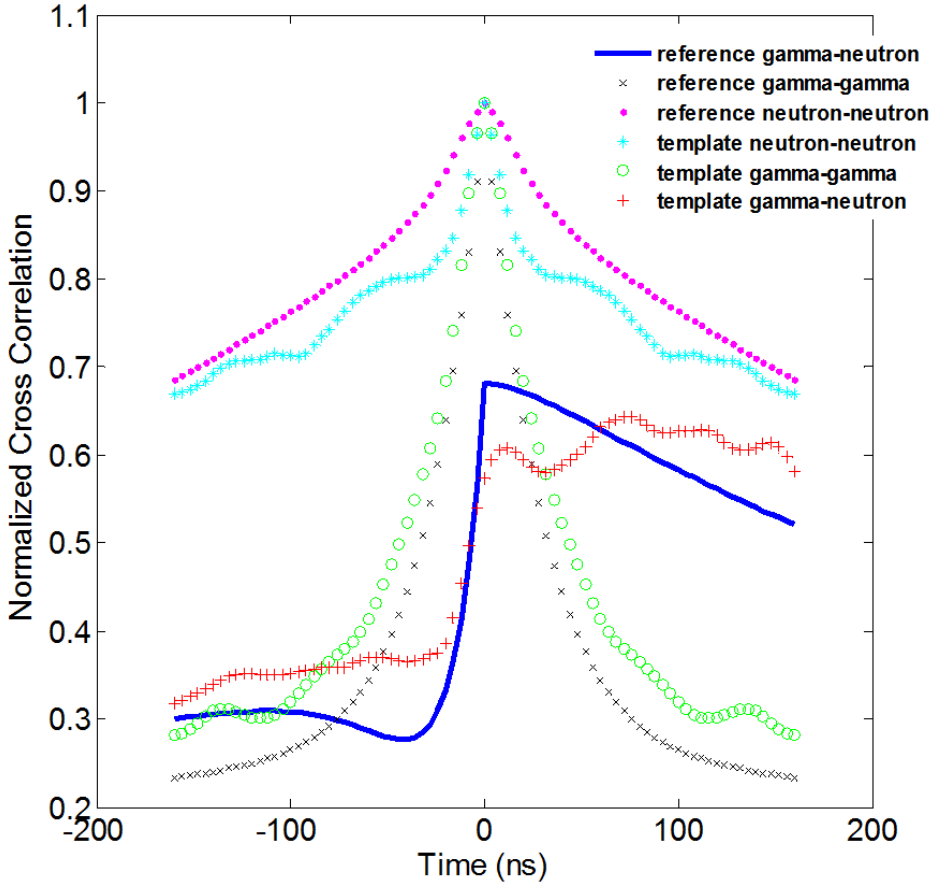

Fig. 4.17 NCC Between the Reference Neutron Pulse and Other Pulses, and NCC Between Template Neutron Pulse and Other Pulses.

4.4. Pileup and Baseline Shift

As the event rate increases, the task of discriminating the neutron and gamma ray pulses becomes more difficult as they are affected by pileup and baseline shift which alter the typical shape of the neutron and gamma ray pulses. Pileup occurs when two or more pulses overlap each other. Fig. 4.18 shows a pileup event where a neutron pulse is seen trailed by two gamma ray pulses. Pileup usually occurs at high event rates. A shift in the

baseline is illustrated in Fig. 4.19. Pileup and baseline shift make it difficult to discriminate neutron and gamma ray pulses as both neutron and gamma ray pulses will have some features of gamma ray and neutron pulses, respectively.

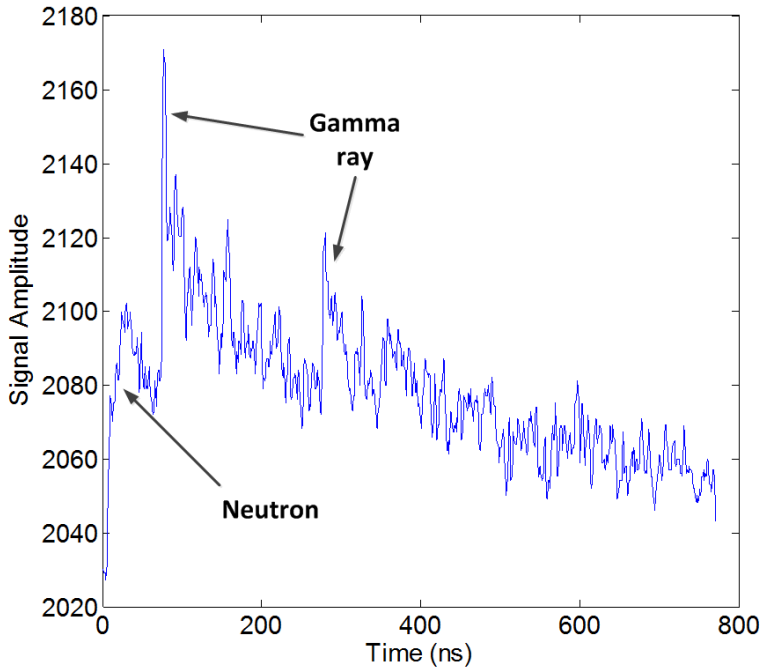

Fig. 4.18 Effect of Pileup of a Neutron and Gamma Ray Pulses.

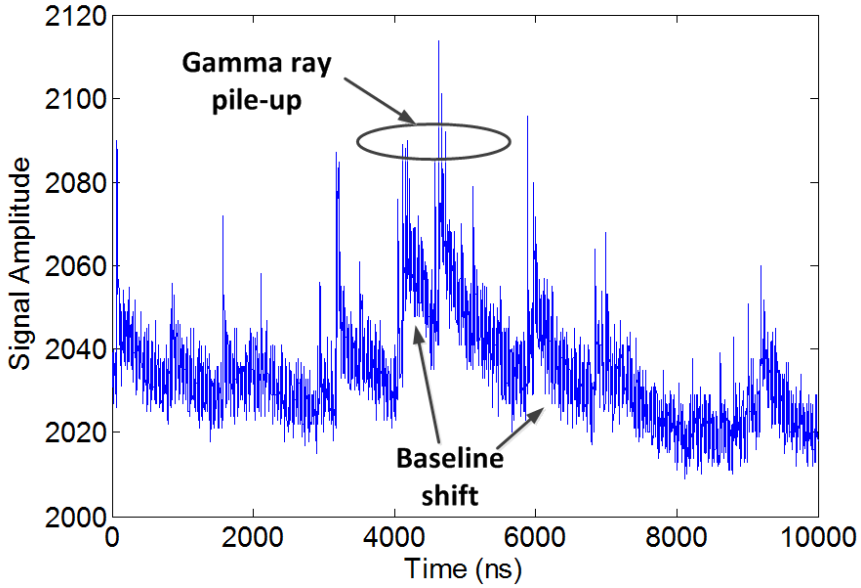

Fig. 4.19 Effect of Baseline Shift.

4.5. Different Cases of Correlation and Examples

In this section, peculiar cases of neutron and gamma ray pulses with pileup will be presented. Fig. 4.20 shows three gamma ray pulses pileup on a neutron pulse. As shown in Fig. 4.21, the NCC plot with reference neutron pulse also reveals this by showing three peaks on plot that look like a NCC plot of template neutron-to-neutron pulse seen in Fig. 4.13 as NCC values across both positive and negative lags are above 0.5 and attain maximum value > 0.7 at zero lag.

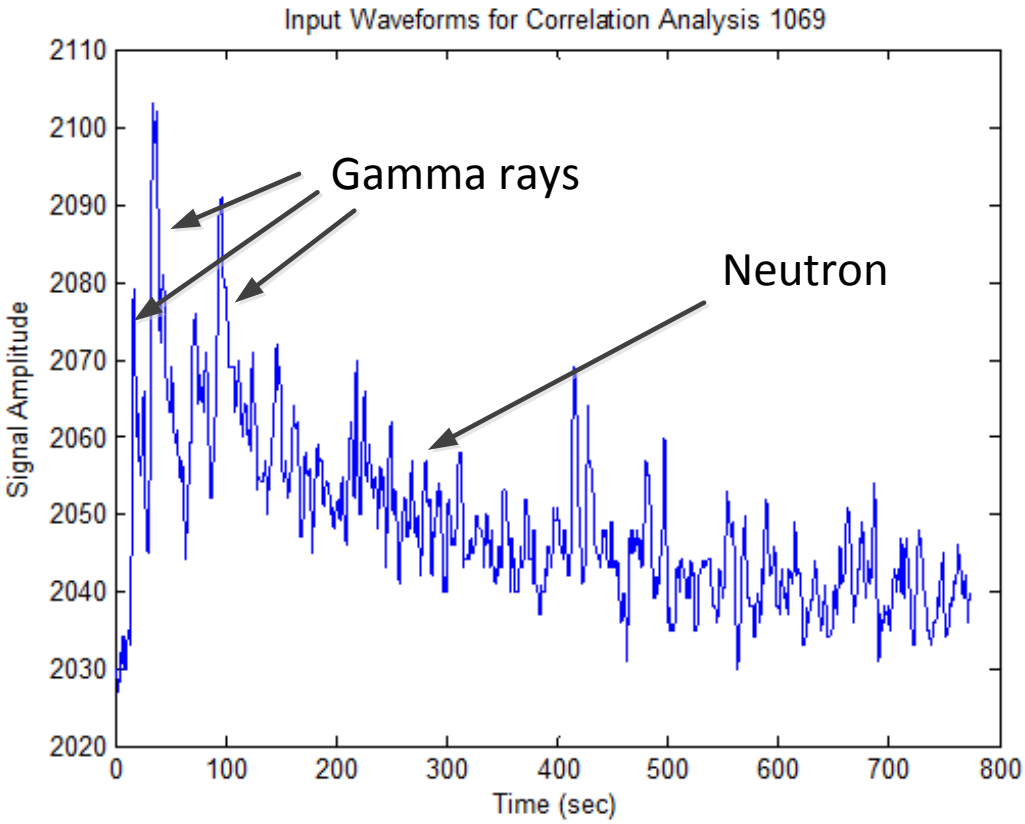

Fig. 4.20 Three Gamma Ray Pulses Pileup on Neutron Pulse.

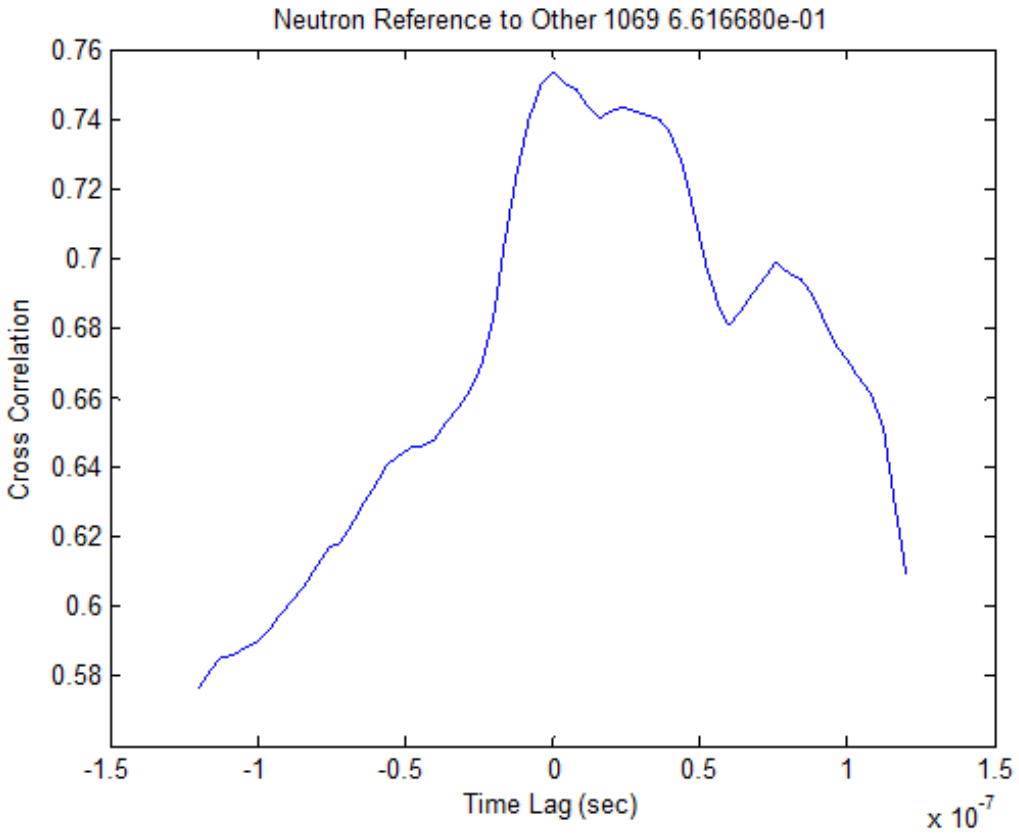

Fig. 4.21 NCC Plot of Template Neutron to Pulse Shown in Fig. 4.20.

Fig. 4.22 shows two gamma ray pulses pileup on a neutron pulse. The NCC plot with template neutron pulse shown in Fig. 4.23 shows two peaks which confirm the presence of gamma ray features but the overall shape resembles a template neutron-neutron NCC plot. Also, the steep decrease in NCC value near zero lag makes it look like a template neutron-to-gamma ray cross correlation plot. This confirms the trouble pileup causes in discriminating neutron and gamma ray pulses.

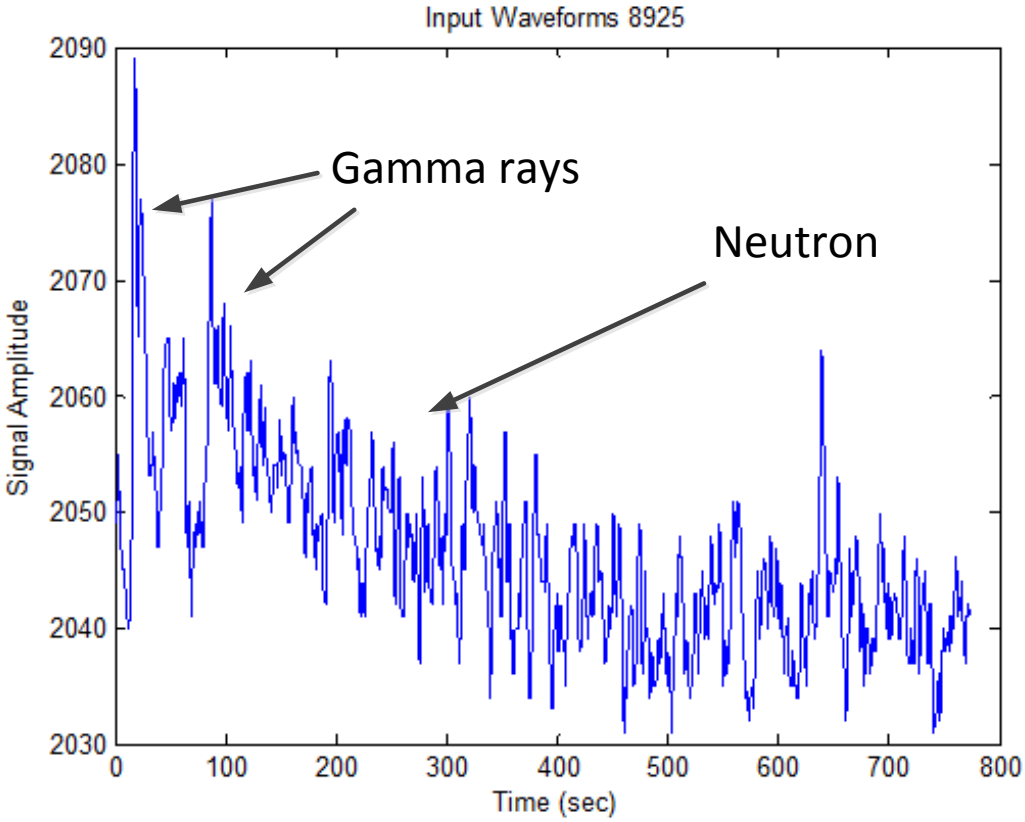

Fig. 4.22 Three Gamma Ray Pulses Piled-Up on Neutron Pulse.

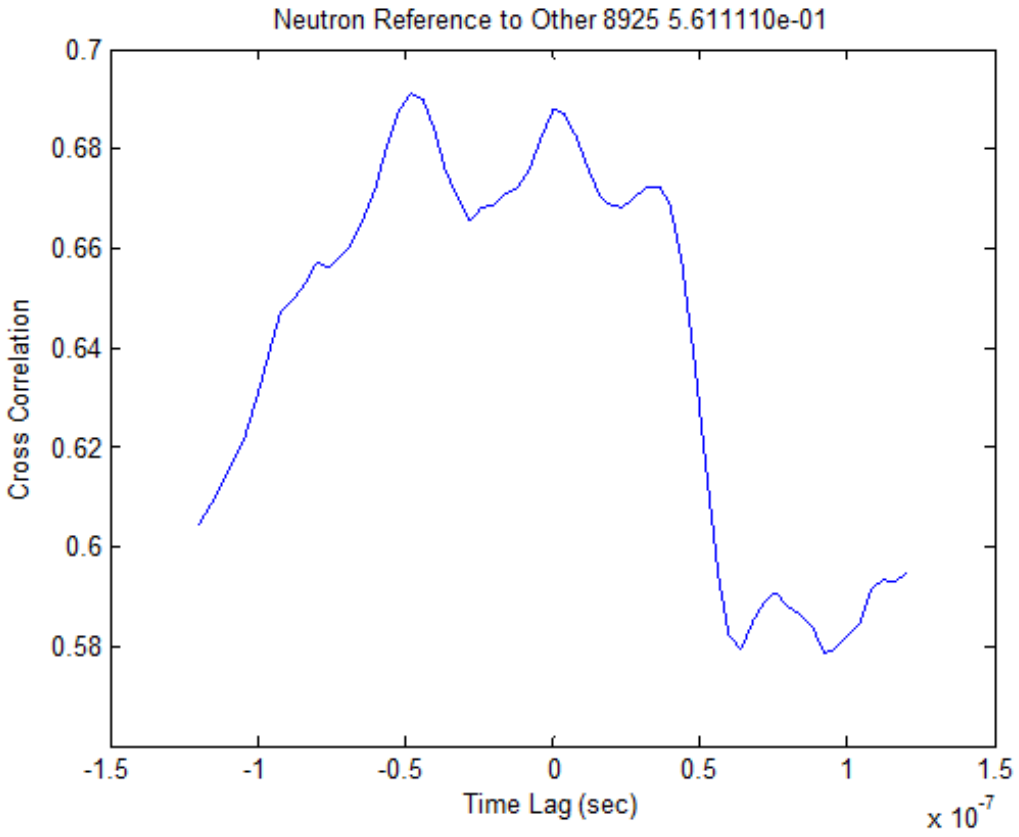

Fig. 4.23 NCC Plot of Template Neutron to Pulse Shown in Fig. 4.22.

Fig. 4.24 shows a gamma ray trailed by a gamma ray and a neutron pulse. This is confirmed by the presence of two peaks, one at zero lag and another at a negative lag of -80 ns in Fig. 4.25. Again, the overall NCC shape looks like a template neutron-to-neutron cross correlation plot. However, a steep decrease in NCC value around zero lag shows a template neutron-to-gamma ray pulse.

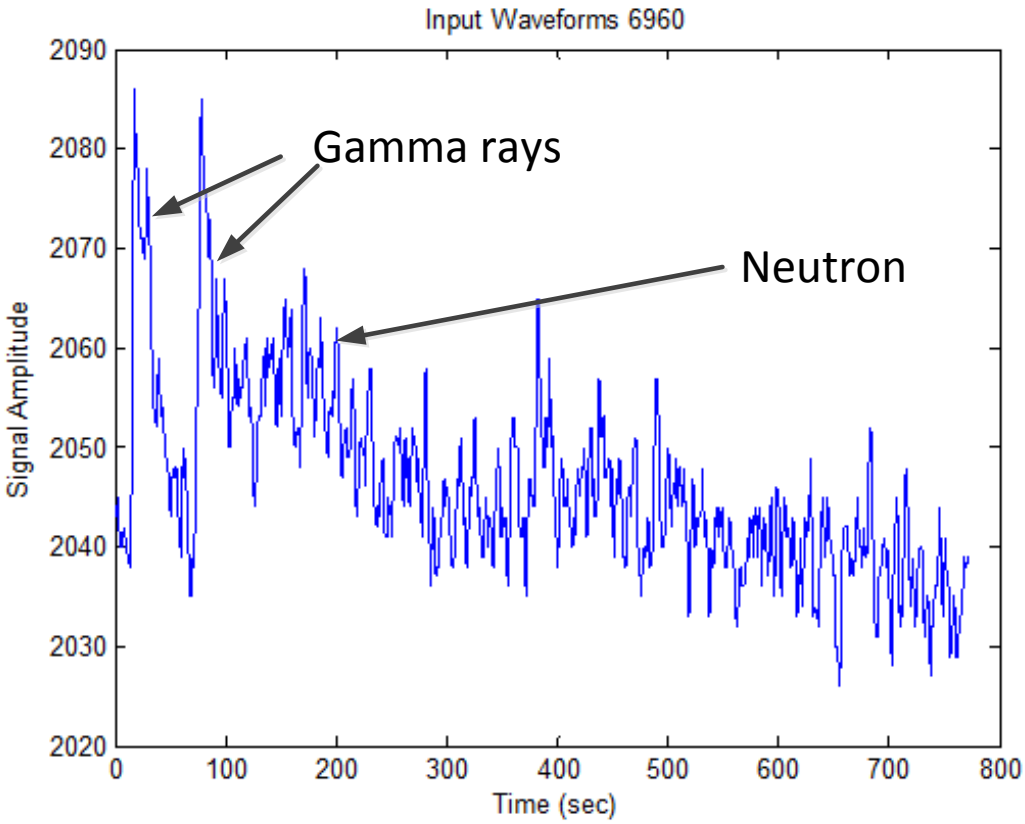

Fig. 4.24 Two Gamma Ray Pulses Piled-Up on a Neutron Pulse.

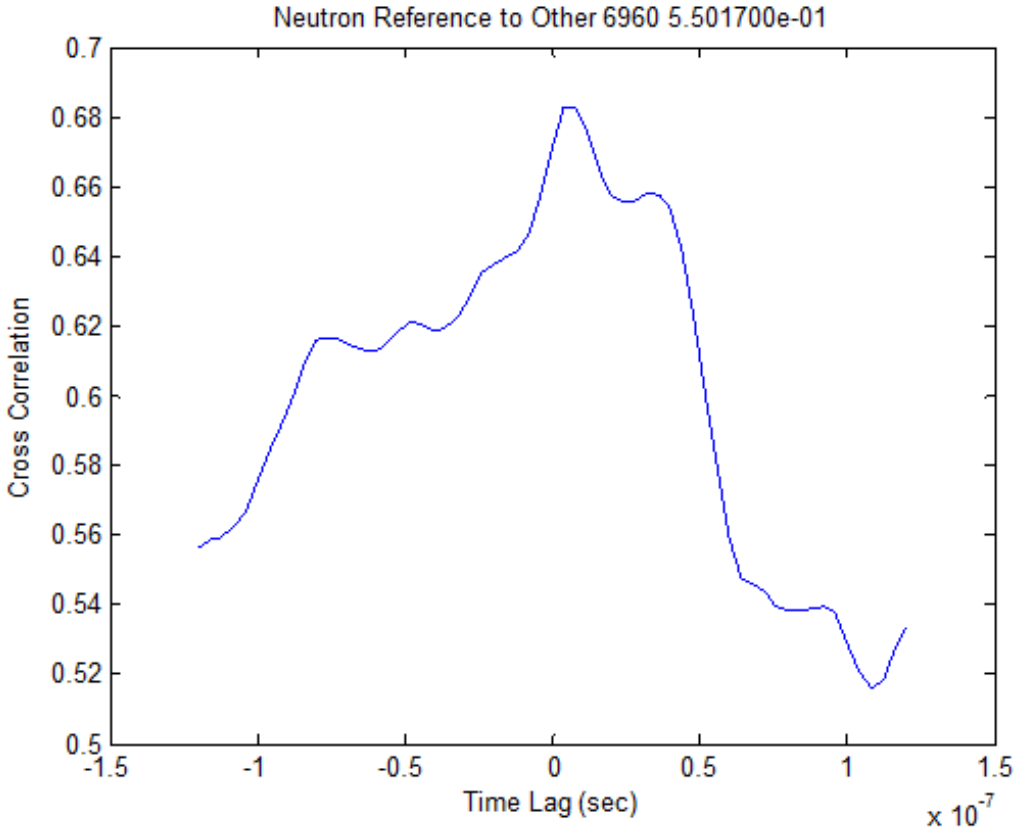

Fig. 4.25 NCC Plot of Template Neutron-To-Neutron Pulse Shown in Fig. 4.24.

4.6. Integral Method

The integral method, also called as CCM, is a well-established PSD method implemented in scintillation counting. Gamma rays have longer decay time as compared to neutrons. This has been used as a basis for differentiating neutron and gamma rays. According to this method, an integral of the pulse tail which is called the short integral, is divided by the integral of the entire pulse which is termed as a long integral. The result of the division is different for neutron and gamma rays, thereby discriminating the two. In

this project, the long integral is taken for 680 ns and the short integral is taken for 280 ns.

$$PSD = I_S / I_L \tag{25}$$

$$Energy = 0.04684 * I_{LL} - 25.07021 \tag{26}$$

Where, I_S is the integral of 280 ns, I_L is the integral of 680 ns and I_{LL} is the integral of 4000 ns. The variables are illustrated in Fig. 4.26. Visually, one can see that the gamma pulse has a sharp peak whereas the neutron pulse does not have a sharp peak.

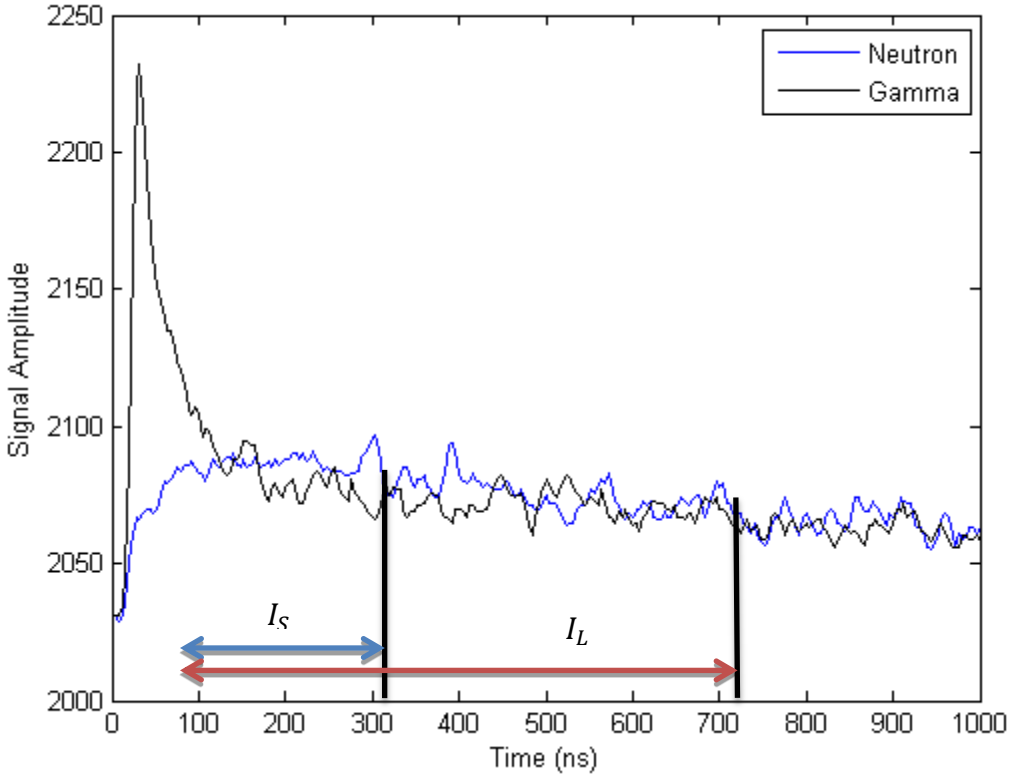

Fig. 4.26 Neutron and Gamma Ray Pulses Along with the Long and Short Integrals for Integral Method.

4.7. Filtered Method

The filtered method is similar to the integral method and the only difference is that radiation pulses are digitally filtered before integrating. A band pass filter is applied to remove long CLYC tails and a low pass filter is applied to obtain the tail information for the PSD. In this project, the long integral is taken for 400 ns and the short integral is taken for 200 ns.

$$PSD = IH_S/(I_L - I_{BL}) \tag{27}$$

$$Energy = 0.41685 * I_{3L} + 18.88835 \tag{28}$$

Where, IH_S is the integral of the band pass filtered signal of 200 ns, I_L is the integral of the 400 ns and I_{BL} is the baseline correction. I_{3L} is the integral of 300 ns. The variables are illustrated in Fig. 4.27. Before applying integral or filtered method, a baseline correction is done. All the samples are reduced by 2025.

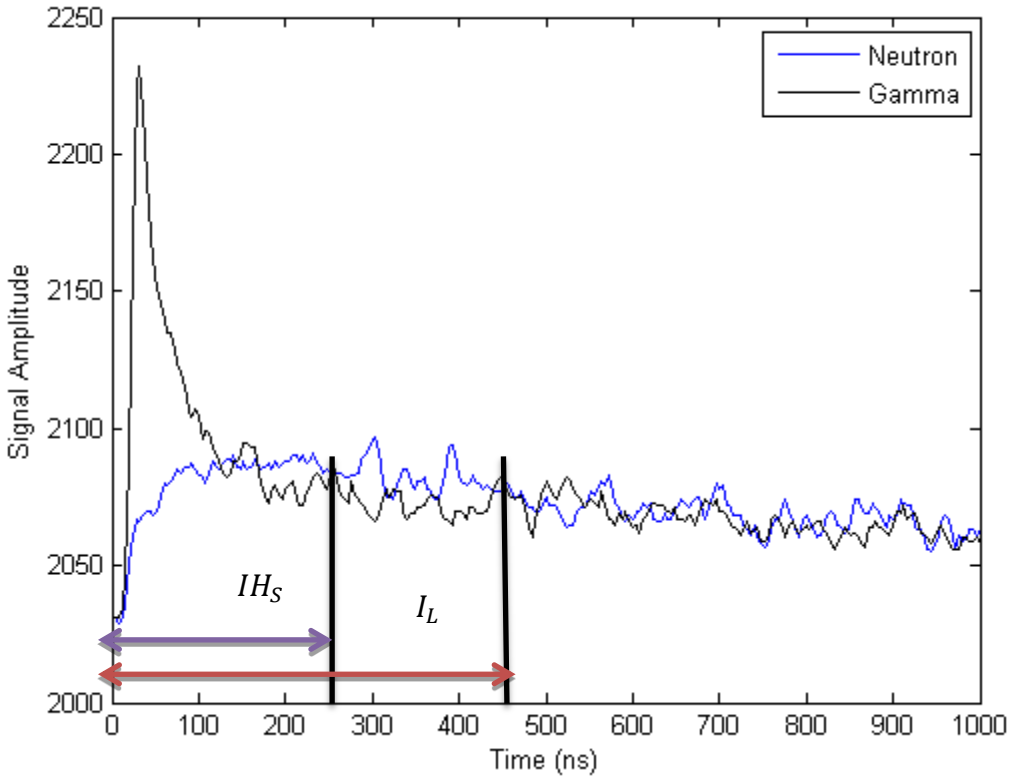

Fig. 4.27 Neutron and Gamma Ray Pulses Along with the Long and Short Integral for Filtered Method.

CHAPTER 5. ANALYSIS OF PSD RESULTS

Chapter 4 discussed how an individual neutron and gamma ray pulse can be discriminated by cross correlating it with either the reference neutron pulse or gamma ray pulse. In this chapter, the results of applying the NCC technique on the samples of neutron and gamma ray pulses acquired using the system discussed in Chapter 3 are presented.

5.1. NCC Data Analysis Using Neutron Reference

Pulses present in each of the data files in Table 3.1 and Table 3.2 are cross correlated with the reference neutron pulse. Data file 1 from Table 3.1 is acquired using only an AmBe source at a 5 kHz event rate. The AmBe source produces both neutron and gamma rays. Fig. 5.1 shows the NCC plot of neutron and gamma ray pulses using the reference neutron pulse for data file 1 in Table 3.1. As shown in Fig. 5.1 for the event rate of 5 kHz, the neutron-to-neutron correlation curves are different in shape and show high correlation when compared to the neutron-to-gamma correlation curves. Specifically, neutron-to-gamma curves exhibit a dip in correlation value for positive lags whereas the neutron-to-neutron curves maintain high correlation (NCC > 0.5) throughout. The separation between neutron-to-neutron and neutron-to-gamma NCC curves is significant at a lag of 72 ns as indicated by a green star in Fig. 5.1. Hence, pulses that have NCC value greater than 0.6 at a lag of 72 ns can be considered as neutron pulses while those below 0.6 are deemed gamma ray pulses. A similar trend can be also seen in Fig. 5.2.

Fig. 5.2 is the NCC plot of neutron and gamma ray pulses for data file 2 from Table 3.2. Data file 2 from Table 3.2 is acquired using two gamma sources ^{22}Na and ^{137}Cs and the AmBe neutron source at a 6 kHz event rate.

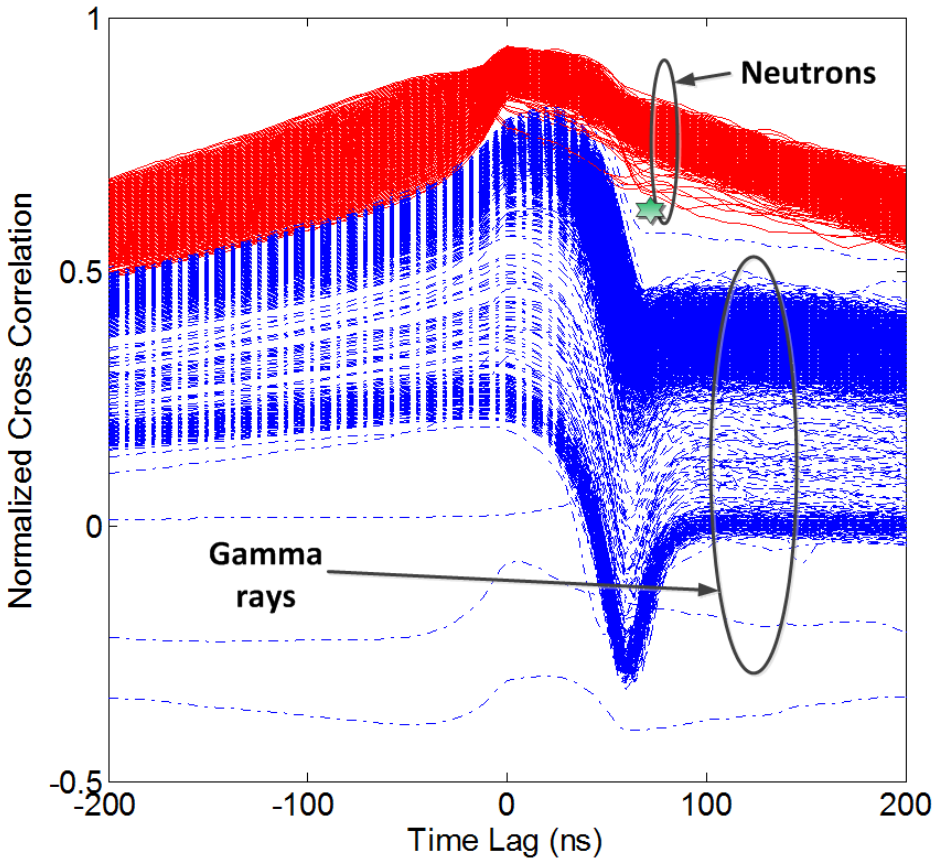

Fig. 5.1 NCC of the Reference Neutron Pulse and Other Pulses in Data File 1 from Table 3.1 at 5 kHz Event Rate.

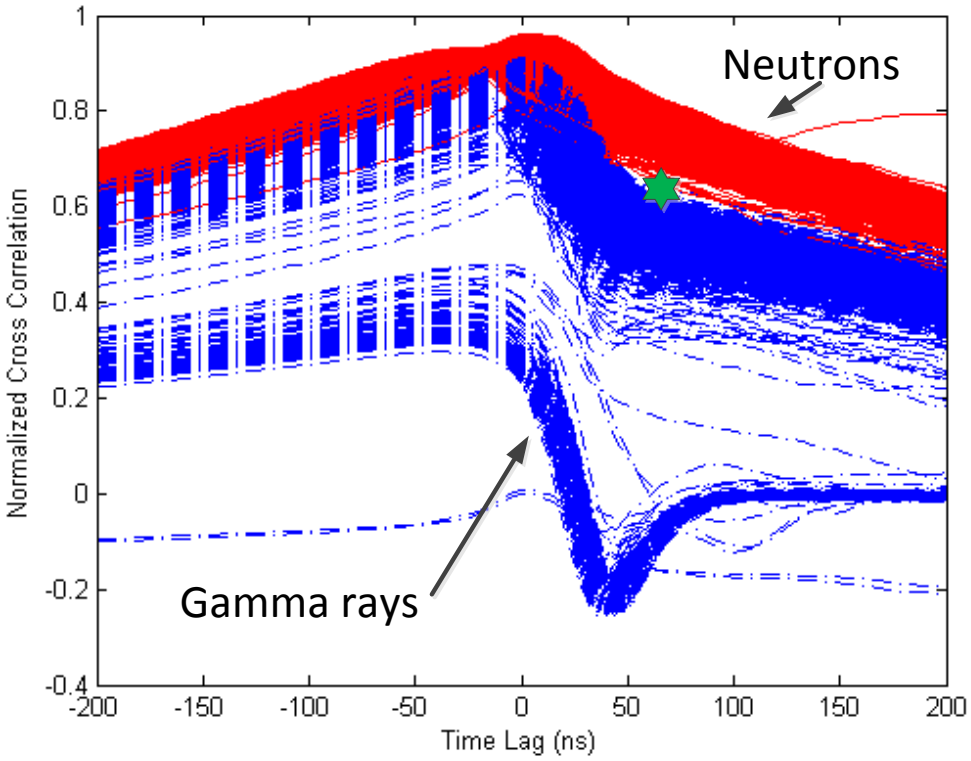

Fig. 5.2 NCC of the Reference Neutron Pulse and Other Pulses in Data File 2 from Table 3.2 at 6 kHz Event Rate.

Fig. 5.3 is the NCC plot of pulses for data file 2 from Table 3.1. Data file 2 from Table 3.1 is acquired using only a ^{137}Cs source at a 10 kHz event rate. ^{137}Cs produces only gamma rays and not neutrons. This is evident from Fig. 5.3 which is the NCC plot of pulses using reference neutron pulse for data file 2. Only few pulses produce a curve similar to the neutron-to-neutron correlation curve and high correlation (NCC > 0.7) at 72 ns and are considered to be neutron pulses. The rest of the pulses exhibit curves that look like the neutron-to-gamma correlation curve and hence are considered to be gamma ray pulses. Presence of few neutron pulses is expected because the AmBe source which generates neutrons is kept away from the detector but not taken out of experimental

system. Since the distance of the neutron source is not far away, few neutrons are expected to reach the scintillator and this is reflected in NCC curves. As discussed above, the separation between neutron-to-neutron and neutron-to-gamma NCC curves is significant at a lag of 72 ns as indicated by a green star in Fig. 5.3. A similar trend is also observed for data file 1 from Table 3.2 as shown in Fig. 5.4. Data file 1 from Table 3.2 is acquired using two gamma ray sources ^{22}Na and ^{137}Cs and without any neutron source. Only few curves look like the neutron-to-neutron cross correlation curves and rest of them look like neutron-to-gamma cross correlation curves. This confirms the presence of few neutron pulses and rest of them are gamma ray pulses.

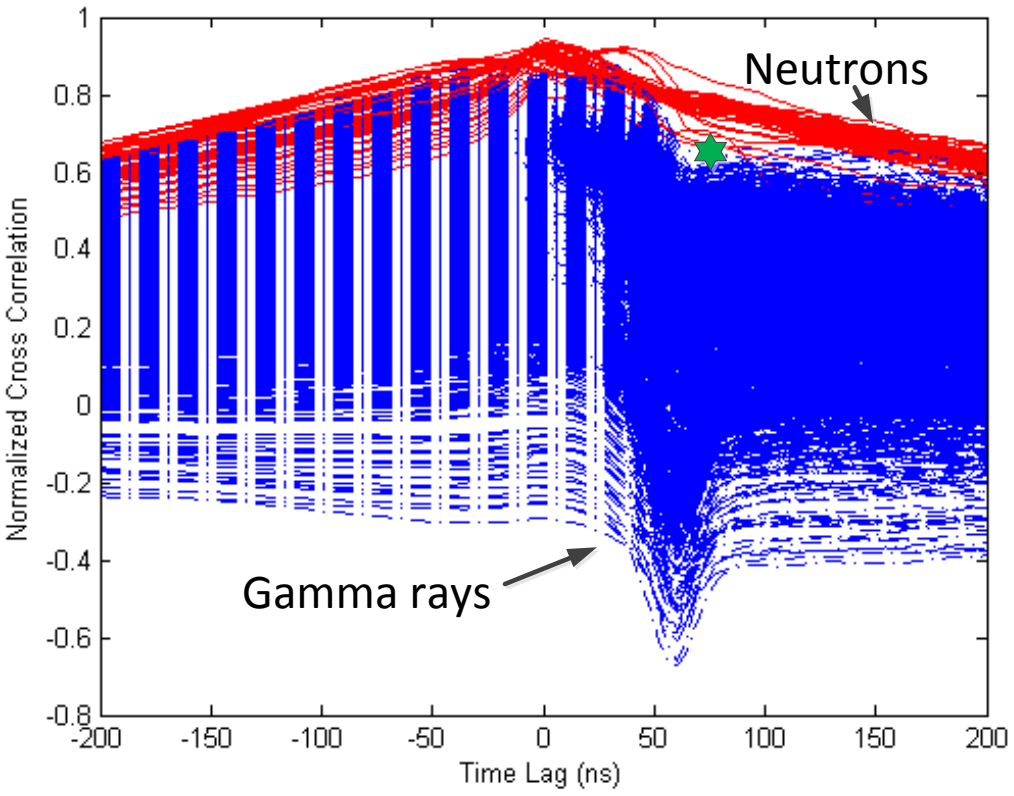

Fig. 5.3 NCC of the Reference Neutron Pulse and Other Pulses in Data File 2 from Table 3.1 at 10 kHz Event Rate.

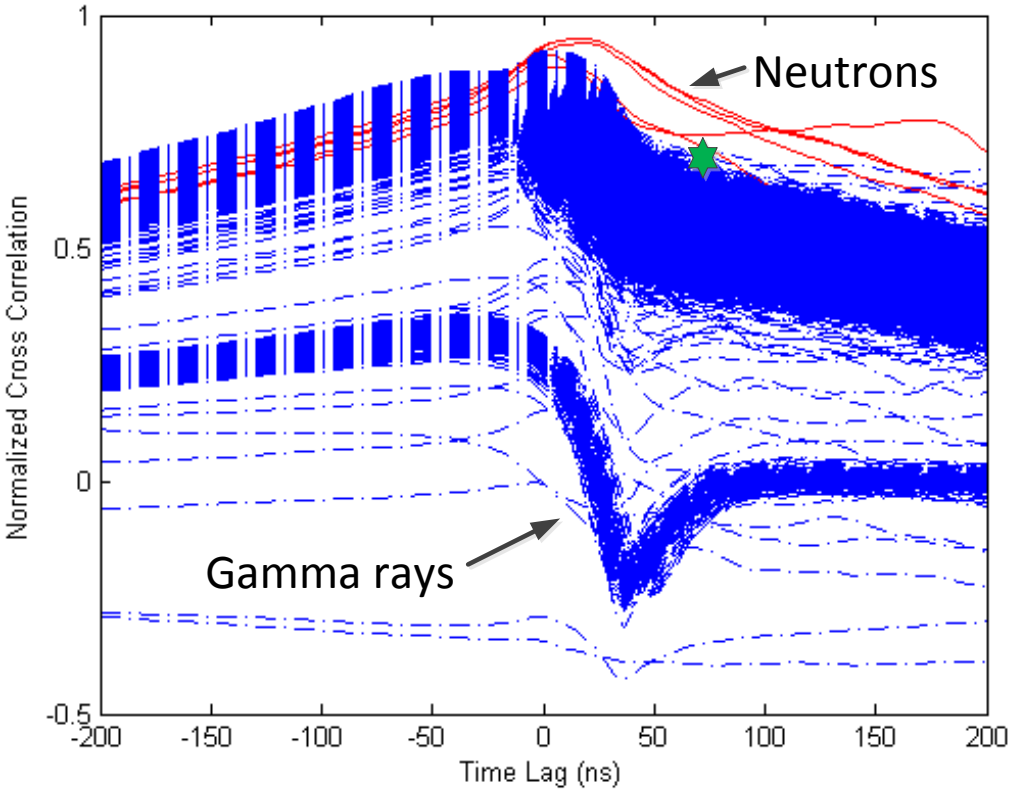

Fig. 5.4 NCC of the Reference Neutron Pulse and Other Pulses in Data File 1 from Table 3.2 at 1 kHz Event Rate.

Fig. 5.5, Fig. 5.6, and Fig. 5.7 show the NCC plots for the reference neutron with pulses for 120 kHz, 180 kHz, and 2.4 MHz, respectively, for data files 5, 6, 8 from Table 3.1 in Chapter 3. Fig. 5.8, Fig. 5.9, and Fig. 5.10 show the NCC plots for reference neutron with pulses for 92 kHz, 191 kHz, and 1390 kHz, respectively for data files 4, 5, 8 from Table 3.2 in Chapter 3. As the event rate further increases from 5 kHz, the separation between neutron-to-gamma and neutron-to-neutron curves decreases and eventually

disappears at event rates higher than 180 kHz due to pileup. Fig. 5.5 and Fig. 5.8 show the NCC plots at an event rate of 120 kHz and 92 kHz, respectively, where there is a very small separation between neutron and gamma ray pulses. At event rates of 180 kHz and 191 kHz, the NCC plots of neutron and gamma ray pulses overlap each other and the separation disappears as shown in Fig. 5.6 and Fig. 5.9. In an extreme case, the very high event rates of 2.4 MHz, and1390 kHz cause the neutron pulses to show a dip in NCC value (Fig. 5.7 and Fig. 5.10) because of gamma ray pileup.

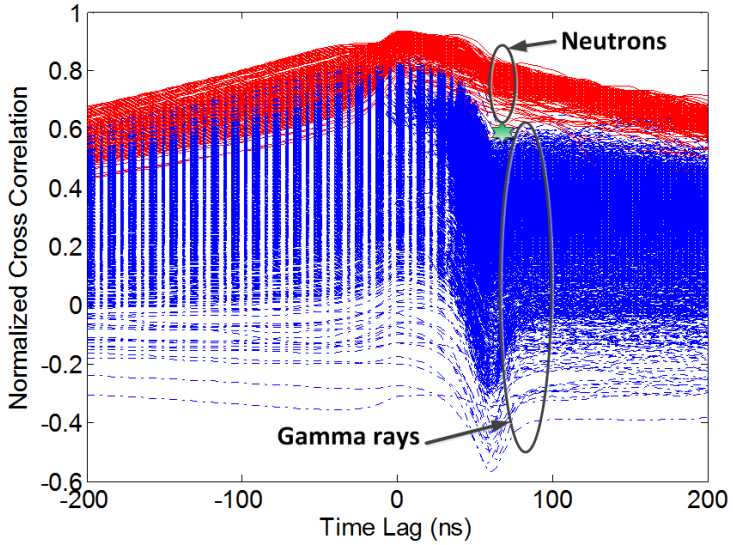

Fig. 5.5 NCC of the Reference Neutron Pulse and Other Pulses in Data File 5 from Table 3.2 at 120 kHz Event Rate.

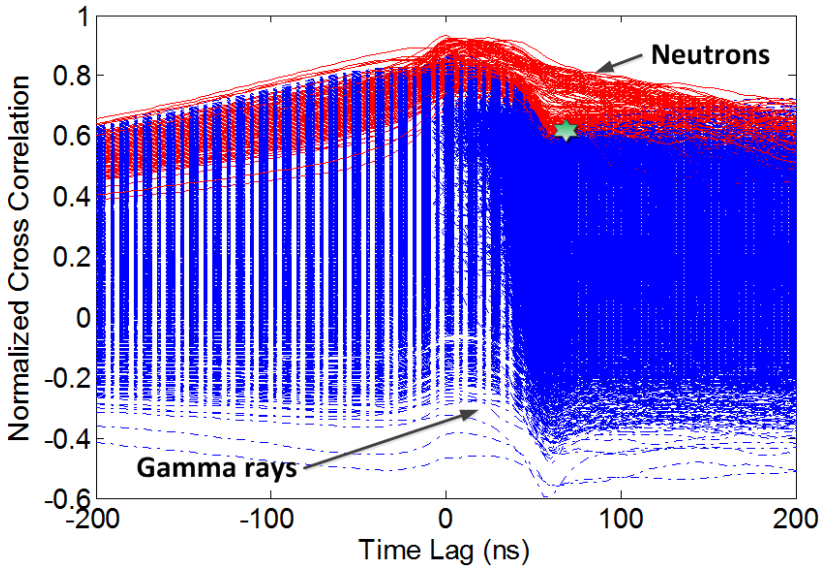

Fig. 5.6 NCC of the Reference Neutron Pulse and Other Pulses in Data File 6 from Table 3.1 at 180 kHz Event Rate.

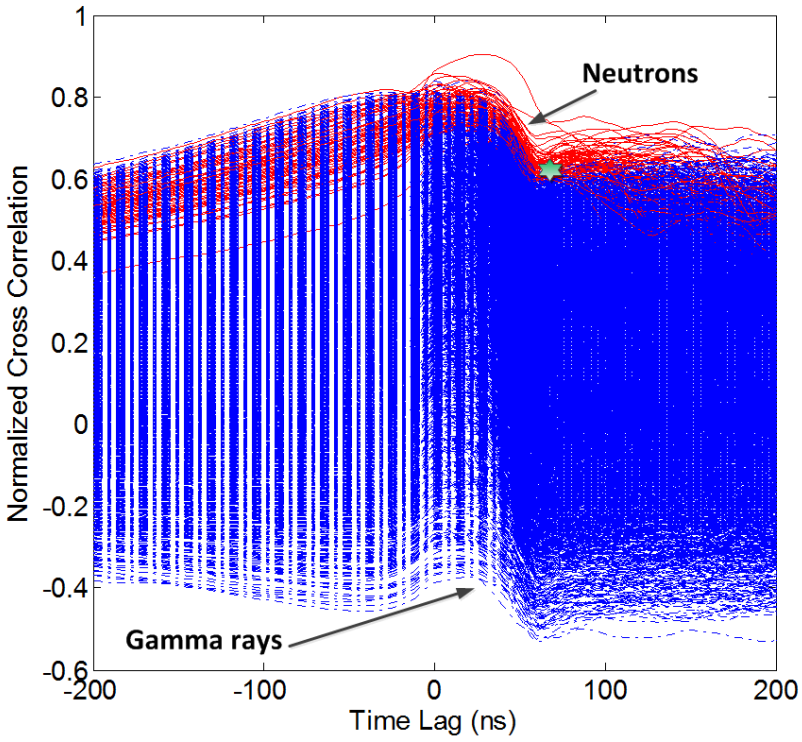

Fig. 5.7 NCC of the Reference Neutron Pulse and Other Pulses in Data File 8 from Table 3.1 at 2.4 MHz Event Rate.

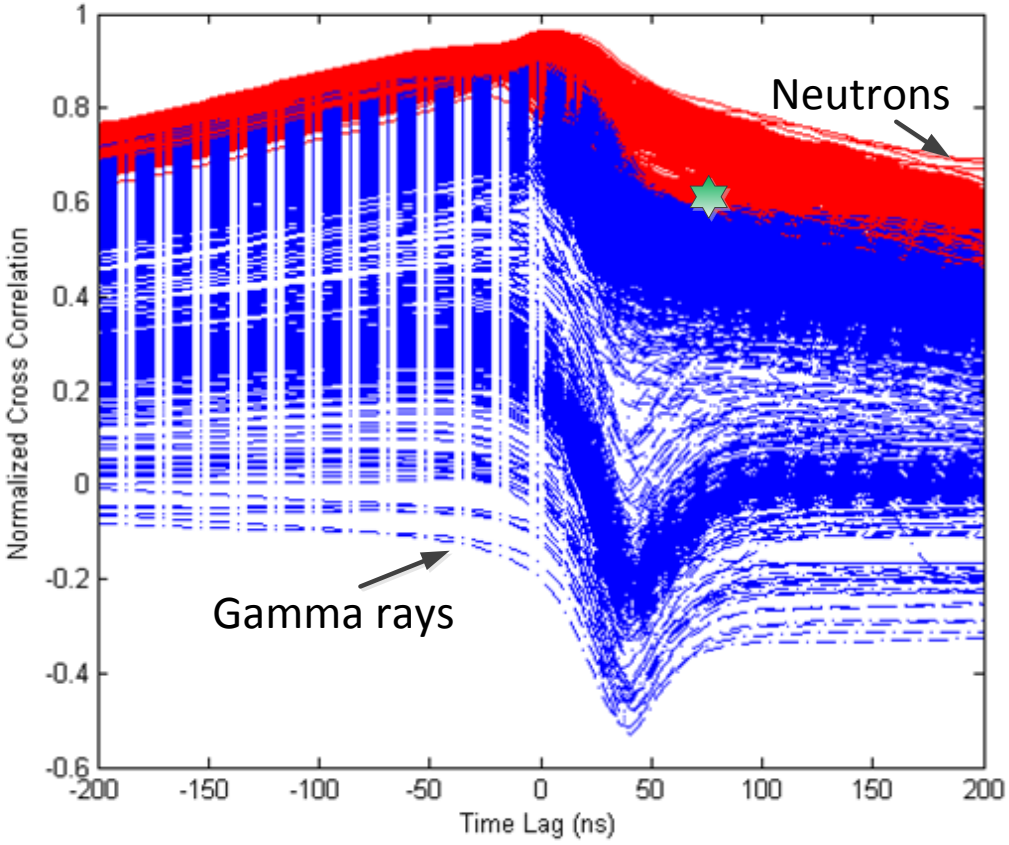

Fig. 5.8 NCC of the Reference Neutron Pulse and Other Pulses in Data File 4 from Table 3.2 at 92 kHz Event Rate.

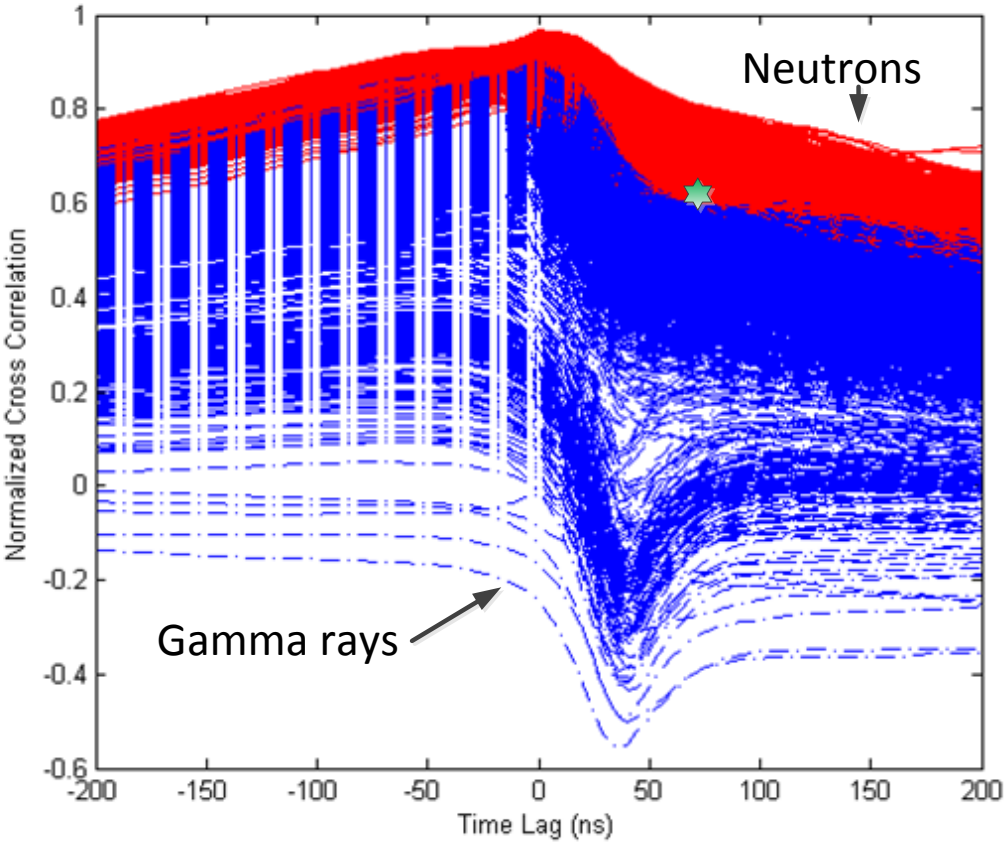

Fig. 5.9 NCC of the Reference Neutron Pulse and Other Pulses in Data File 5 from Table 3.2 at 191 kHz Event Rate

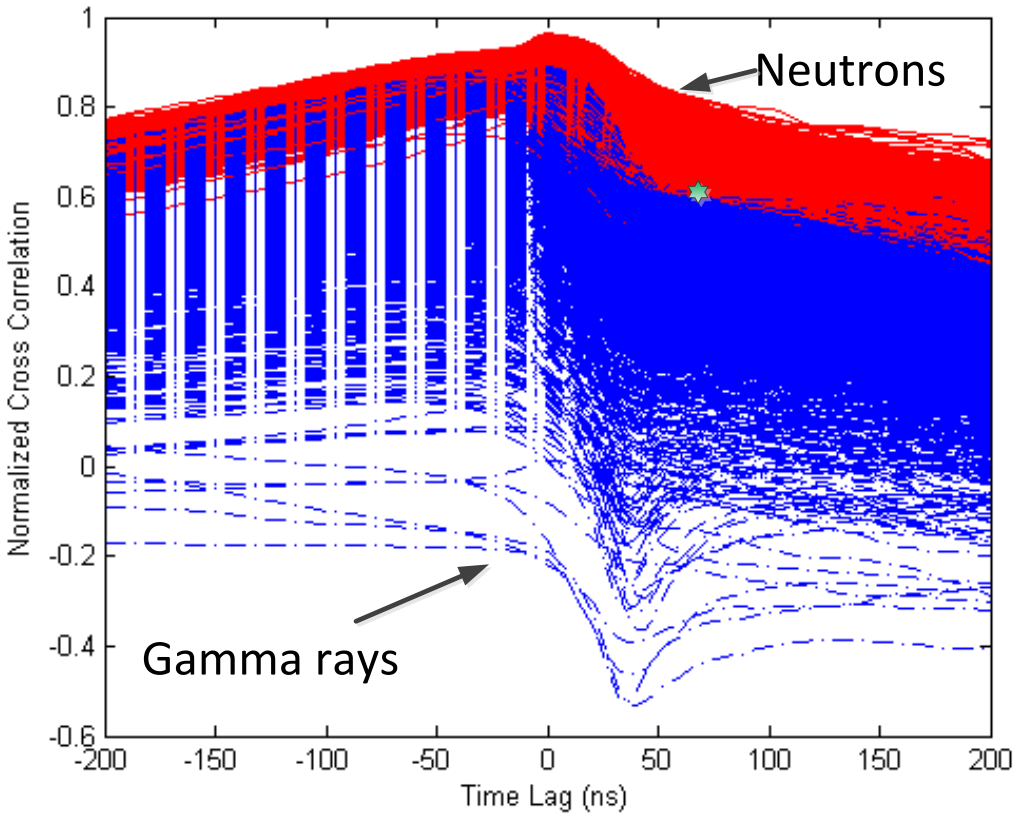

Fig. 5.10 NCC of the Reference Neutron Pulse and Other Pulses in Data File 8 from Table 3.2 at 1390 kHz Event Rate.

5.2. NCC Data Analysis Using Gamma Ray Reference

Analysis similar to Section 5.1 is carried out with the reference gamma ray pulse. Fig. 5.11 presents the NCC results using the reference gamma ray with data of data file 1 from Table 3.1 at 5 kHz. With the reference gamma ray pulse, gamma-to-neutron curves exhibit a sharp increase in correlation value near the zero lag and maintain their value (NCC > 0.4) for the positive lags. The gamma-to-gamma correlation curves also exhibit a

sharp rise in correlation value near the zero lag, however their correlation value decreases significantly as the time lag increases as shown in Fig. 5.11. Overall, the gamma-to-neutron curves exhibit a ‘S’ shape, whereas gamma-to-gamma curves display an ‘A’ shape. This difference can be used to discriminate neutron and gamma ray pulses. The distinction between gamma-to-neutron and gamma-to-gamma pulses is largest at a lag of 156 ns. Pulses that have correlation value greater than 0.46 can be considered as neutron pulses while those below are considered gamma ray pulses as indicated by a green star in Fig. 5.11. Fig. 5.12 shows the NCC plot with reference gamma ray pulse for data file 5 from Table 3.1. At the 120 kHz event rate, the “S” shape of gamma-to-neutron curves and the “A” shape of gamma-to-gamma curves are visible. Again, as the event rate increases, gamma-to-gamma and gamma-to-neutron curves merge due to pileup as shown in Fig. 5.13 and Fig. 5.14 for the 180 kHz and 2.4 MHz event rates, respectively.

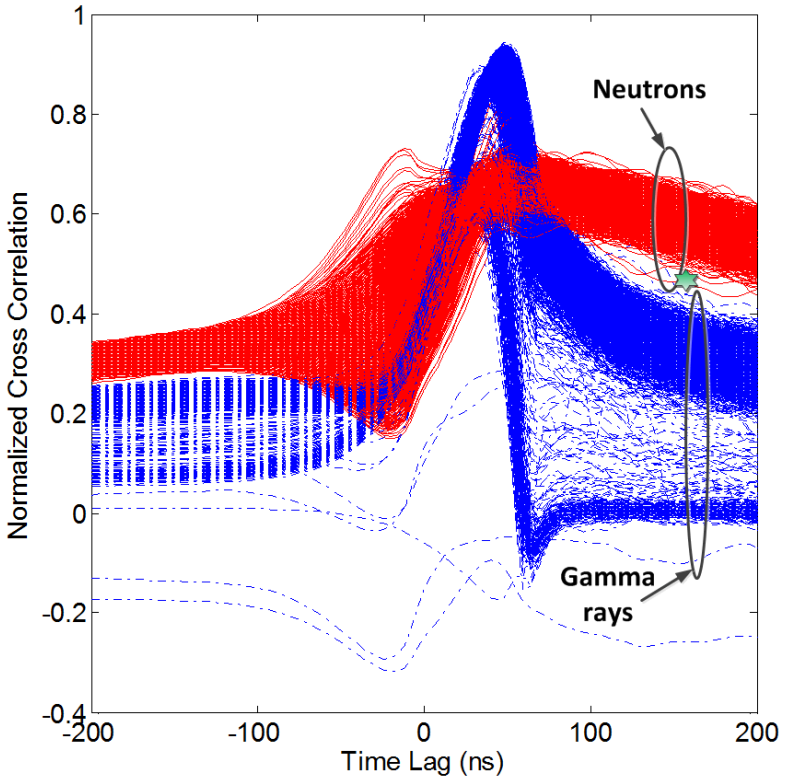

Fig. 5.11 NCC of the Reference Gamma Ray Pulse and Other Pulses in Data File 1 from Table 3.1 at 5 kHz Event Rate.

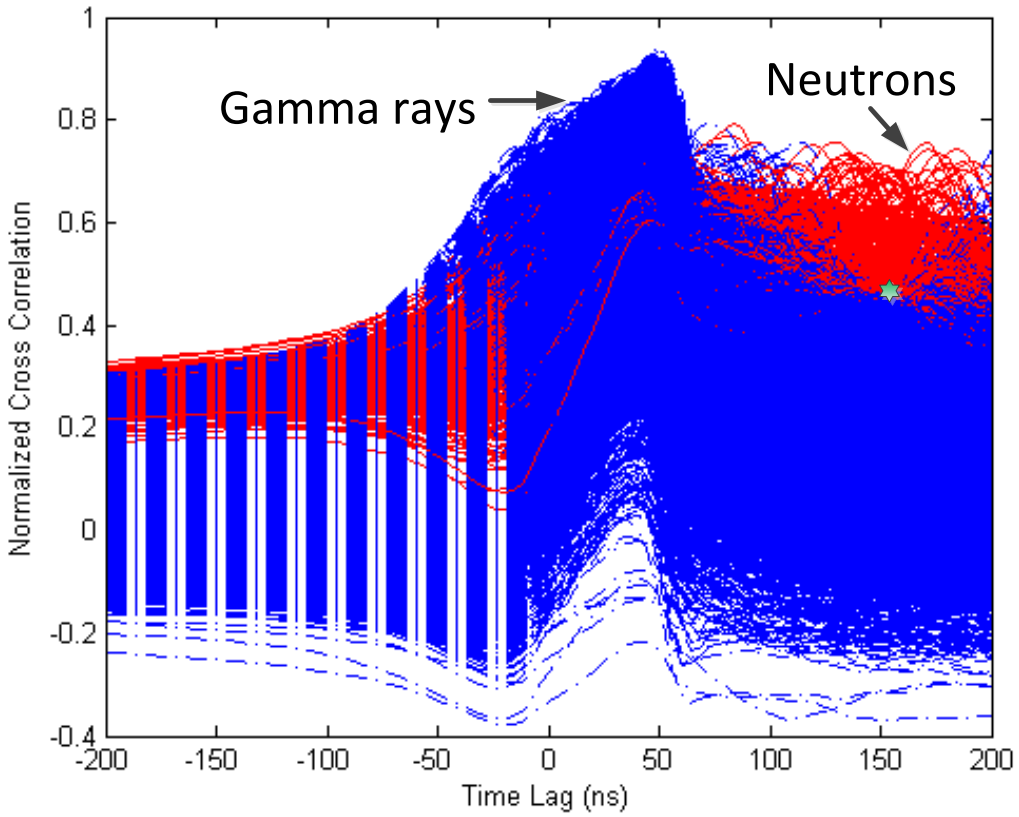

Fig. 5.12 NCC of the Reference Gamma Ray Pulse and Other Pulses in Data File 5 from Table 3.1 at 120 kHz Event Rate.

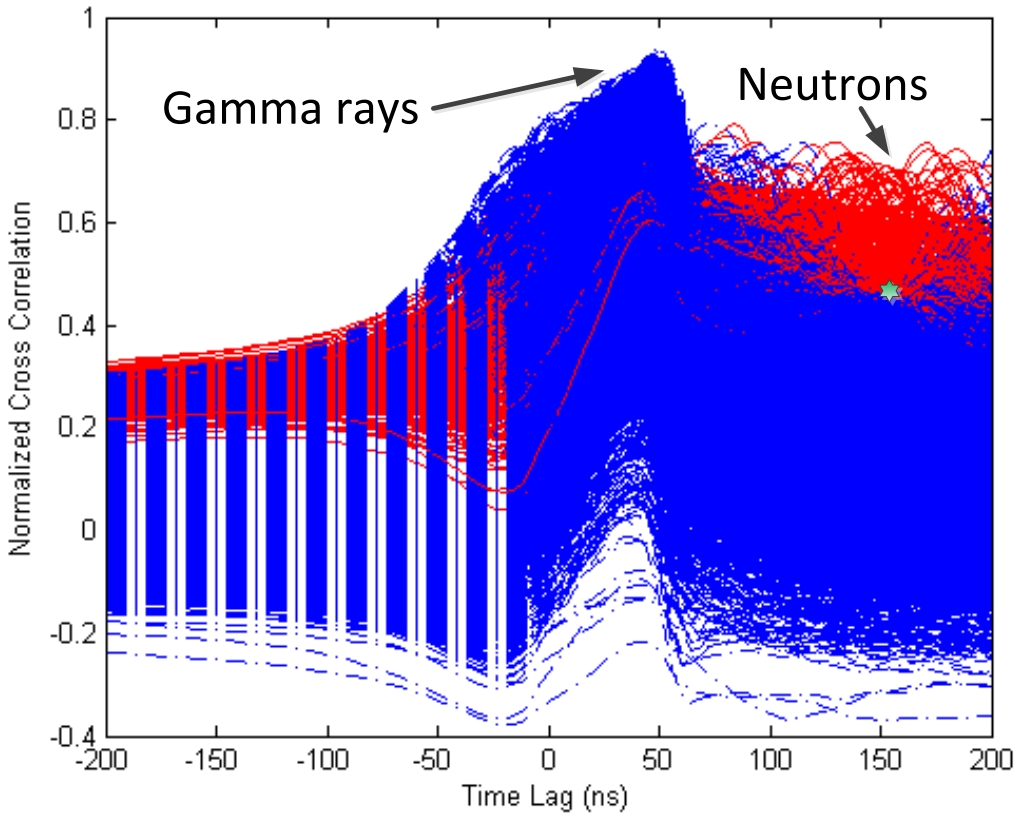

Fig. 5.13 NCC of the Reference Gamma Ray Pulse and Other Pulses in Data File 6 from Table 3.1 at 180 kHz Event Rate.

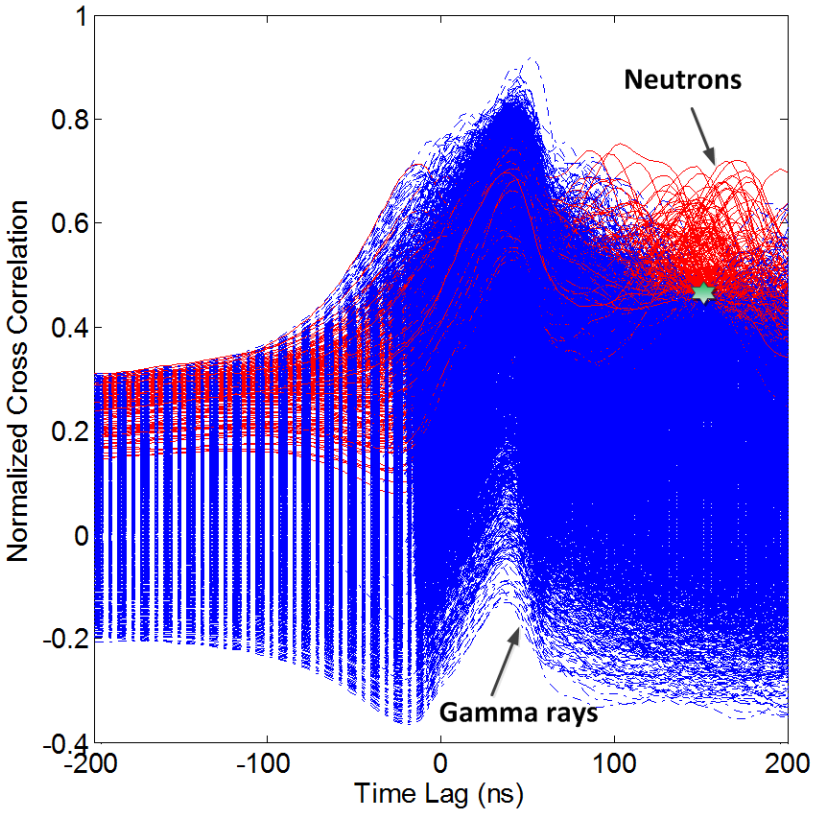

Fig. 5.14 NCC of the Reference Gamma Ray Pulse and Other Pulses in Data File 8 from Table 3.1 at 2.4 MHz Event Rate.

In the high event rate data sets, the probability of finding only neutron features in neutron pulses and only gamma features in gamma pulses is low. A pulse can have multiple gamma and neutron components due to pile up (see Section 4.5). In this situation, a pulse that is identified as a neutron has been observed to typically contain a high-energy neutron pulse as well as low-energy gamma ray pulses, and a pulse that is identified as a gamma ray pulse generally consists of a high-energy gamma ray and low-energy neutron pulses. These pulses when cross correlated with the reference neutron pulse exhibit a

reduction in NCC value compared to the NCC value of the pure neutron pulse. However, evaluation of a large number of such pulses shows that pulses which exhibit a NCC value higher than 0.8 at a lag of around 60 ns to 72 ns, where gamma ray pulses show a dip, with the reference neutron are typically neutron pulses. Fig. 5.1 to Fig. 5.10 show that some pulses fall between 0.6 and 0.8 NCC value. In order to discriminate these pulses a new method will be discussed in next section. A similar trend is observed when the reference gamma ray pulse is used for cross correlation. Neutron pulses typically have a NCC value greater than 0.46 at a lag of 156 ns when cross correlated with the reference gamma ray pulse. Typical cutoffs are shown in Table 5.1 for discriminating pulses using the NCC method with reference neutron and gamma ray pulses.

Overall, employing the reference neutron provides a better separation between neutron and gamma ray pulses as revealed by comparison of Fig. 5.1 and Fig. 5.11. Henceforth, all the analyses will be carried out using the reference neutron pulse.

Table 5.1 NCC Cutoff for Neutron and Gamma Ray References

Pulse	NCC cutoff with neutron reference	NCC cutoff with gamma ray reference
Gamma ray	< 0.6	< 0.46
Neutron	> 0.8	> 0.46
Lag time at which cutoff is taken	72 ns	156 ns

5.3. R-Square Method

From the above discussion, it is clear that neutrons produce NCC values that are linear and gamma rays produce nonlinear NCC curves from the maximum NCC value to the end of the positive lags when cross correlated with reference neutron pulse. This enables using the straightness of the line from the maximum NCC value to the end of the positive lags to discriminate neutrons and gamma rays. R2 is a statistical measure of how close the data are to the fitted regression line. The regression line in our case is a straight line modelled using polynomial of degree one. R2 is calculated from NCC values beginning from the maximum NCC value to the final NCC values in the positive lags. If R2 is greater than 0.95, the NCC plot is considered to be belonging to a neutron, and R2 less than 0.95 belongs to a gamma ray. Fig. 5.15 and Fig. 5.16 show the fitted neutron NCC curve and gamma ray NCC curve, respectively, using Eq. (29), a first degree polynomial. Fig. 5.15 also shows the regression line and R-square value of the neutron NCC curve is 0.97 which is above 0.95. Fig. 5.16 shows the regression line and R-square value of gamma ray NCC curve is 0.89 which is below 0.95. Eqs. (30) and (31) are employed to calculate slope and intercept of the line whose equation defined by Eq. (29). Eq. (32) is employed to calculate R2.

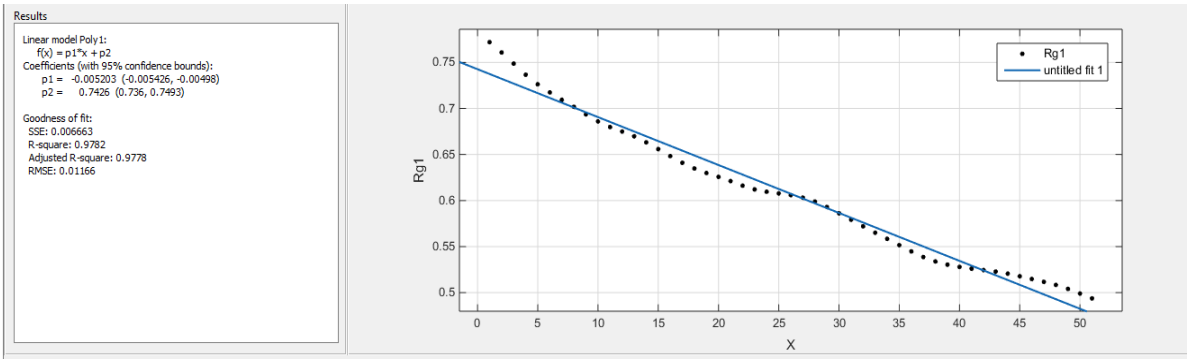

Fig. 5.15 Regression Line of NCC Values for an Arbitrary Neutron Pulse.

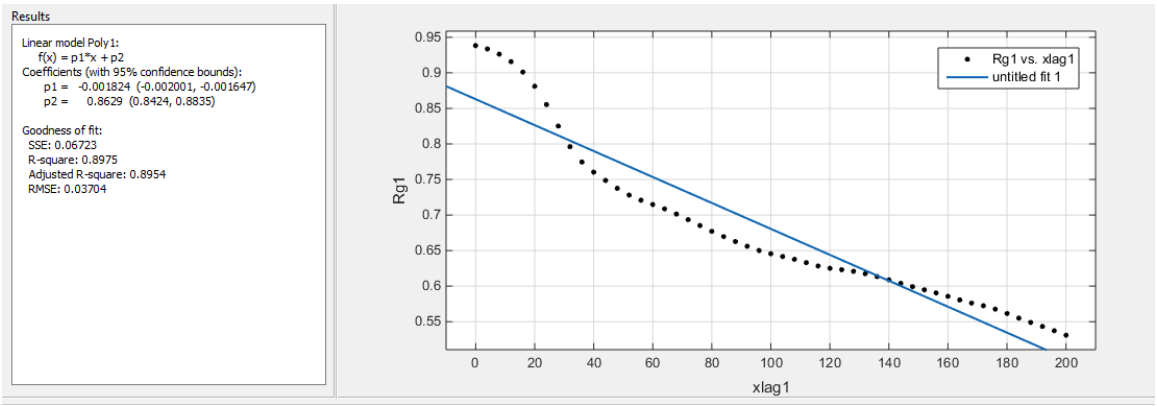

Fig. 5.16 Regression Line of NCC Values for an Arbitrary Gamma Ray Pulse.

$$\hat{y} = p2 + p1x \tag{29}$$

$$p1 = \frac{\sum(x-\bar{x})(y-\bar{y})}{\sum(x-\bar{x})^2} \tag{30}$$

$$p2 = y - px \tag{31}$$

$$R^2 = \frac{\sum(\hat{y}-\bar{y})}{\sum(y-\bar{y})^2} \tag{32}$$

Where, $\bar{y}$ is the mean of y, $\bar{x}$ is the mean of x, $\hat{y}$ is the fitted regression line, p_2 is the intercept of the line y , and p_1 is the slope of line y .

5.4. Discrimination Of Neutron-Gamma Ray Pulses

Pulse shape discrimination (PSD) plots are obtained by graphing the PSD metric against the energy metric. For Fig. 5.17, Fig. 5.18, Fig. 5.19, Fig. 5.20, Fig. 5.21, Fig. 5.22, Fig. 5.23, Fig. 5.24, and Fig. 5.25, the PSD metric is the NCC value for pulses correlated with the reference neutron pulse at a correlation lag of 72 ns. For Fig. 5.26 and Fig. 5.27, the PSD metric is the NCC value for pulses correlated with the reference gamma ray pulse at a correlation lag of 156 ns. The energy metric for the plots is the integral value of the pulse from 0 to 3092 ns. The integral value of a pulse is obtained by summing the smoothed averages of the N baseline-corrected samples that define the pulse. Five consecutive samples are used for smoothing, and the baseline is calculated by taking the average of the first 5 to 10 samples before the actual pulse begins. The integral value calculated here does not include the entire pulse tail.

5.5. Pulse Shape Discrimination Using Reference Neutron Pulse

In Fig. 5.17 to Fig. 5.25, the red-colored data points in the upper region have been deemed neutron pulses and the blue-colored data points in the lower region were judged as gamma pulses. The wide separation between neutron and gamma ray pulses observed in Fig. 5.1 and Fig. 5.2 is also reflected in the PSD plots of Fig. 5.17 and Fig. 5.22. Neutron and gamma ray pulses are discriminated by applying the NCC cutoff from Table 5.1. Similar to Fig. 5.5, Fig. 5.18 also shows a very small separation between the neutron and gamma ray pulses at the event rate of 120 kHz. In Fig. 5.19, a band of neutron pulses merge with the cluster of gamma ray pulses as observed in Fig. 5.6. The group of neutron pulses separated by a small gap in Fig. 5.19 represents the pure neutron pulses without

any pileup. As discussed in Section 5.1, when the event rate increases above 180 kHz, the two regions merge due to the presence of weak, low-energy gamma ray pulses along with strong, high-energy neutron pulses and vice versa. However, pulses that produce PSD metric values above 0.6 when correlated with the reference neutron pulse are mostly neutron pulses. Fig. 5.20 shows the PSD plot at a very high event rate of 2.4 MHz. At this event rate, very few neutron pulses are identified and their PSD values are observed to be converging with those of the gamma ray pulses. A similar trend is also seen in the PSD plots of data files 1, 2, 4, 5, 8 from Table 3.2 given in Fig. 5.21 to Fig. 5.25.

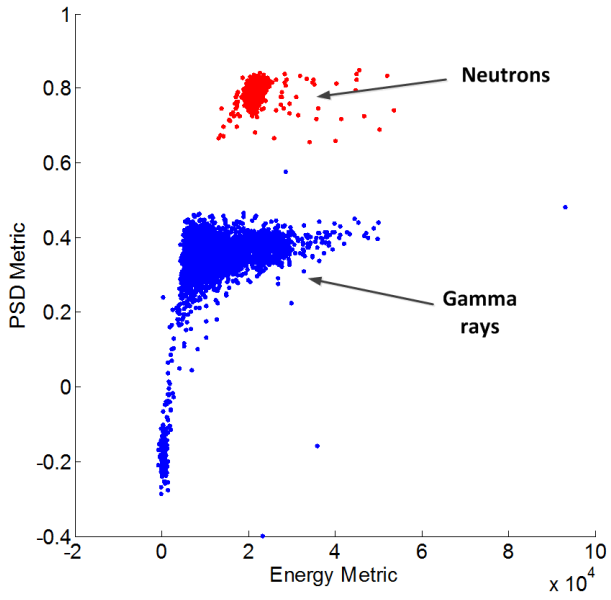

Fig. 5.17 PSD Plot of Reference Neutron Pulse and Other Pulses in Data File 1 from Table 3.1 at 5 kHz Event Rate.

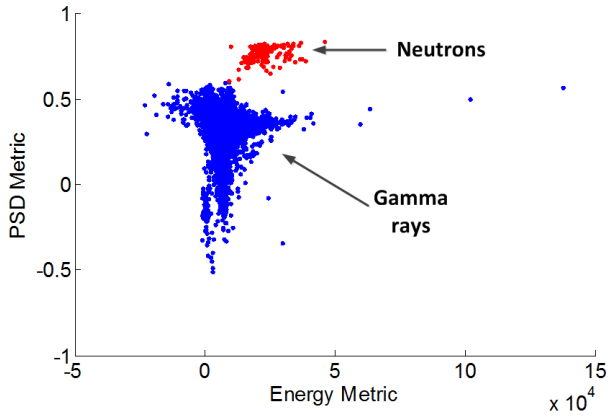

Fig. 5.18 PSD Plot of Reference Neutron Pulse and Other Pulses in Data File 5 from Table 3.1 at 120 kHz Event Rate.

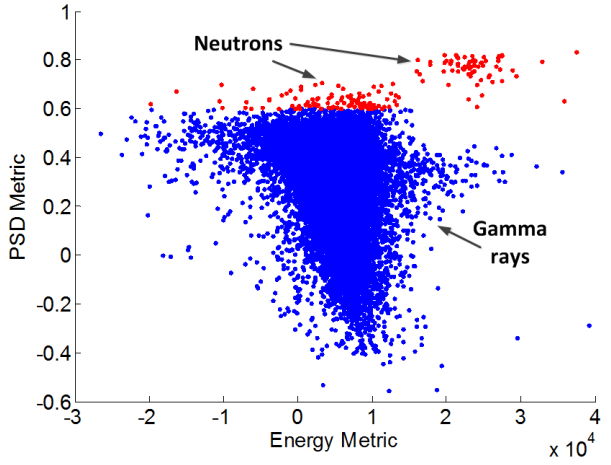

Fig. 5.19 PSD Plot of Reference Neutron Pulse and Other Pulses in Data File 6 from Table 3.1 at 180 kHz Event Rate.

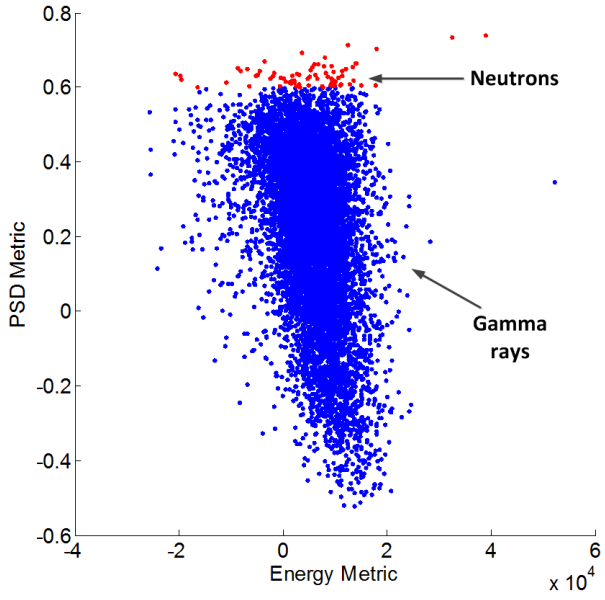

Fig. 5.20 PSD Plot of Reference Neutron Pulse and Other Pulses in Data File 8 from Table 3.1 at 2.4 MHz Event Rate.

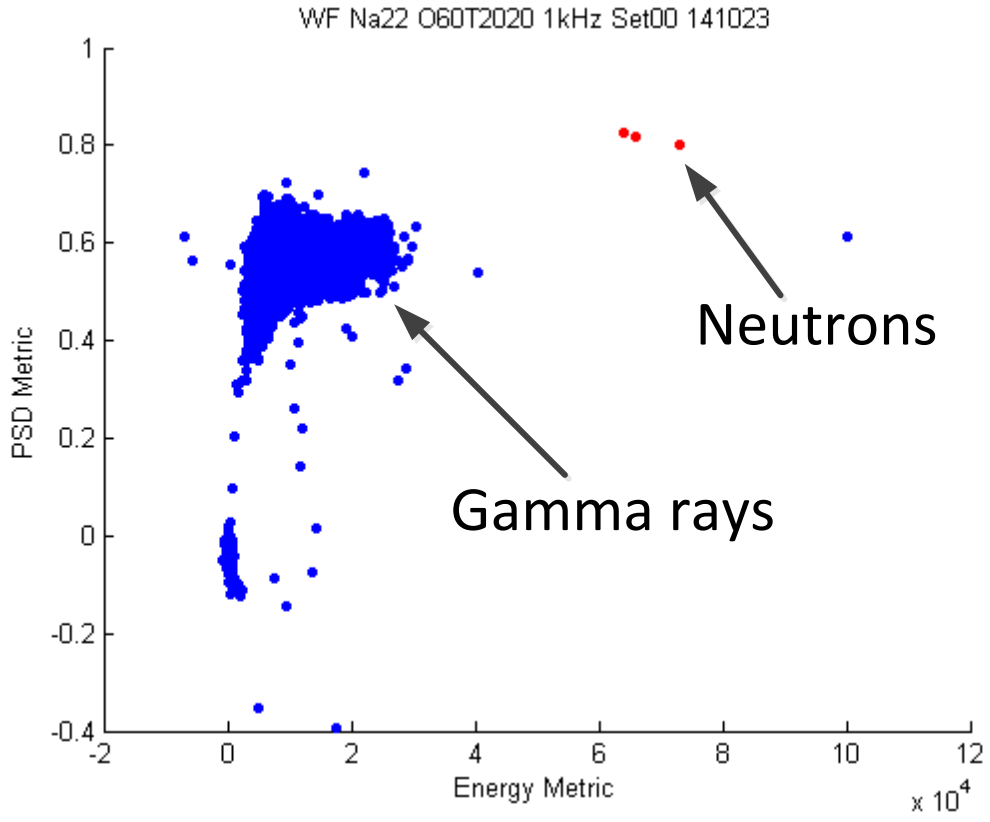

Fig. 5.21 PSD Plot of Reference Neutron Pulse and Other Pulses in Data File 1 from Table 3.2 at 1 kHz Event Rate.

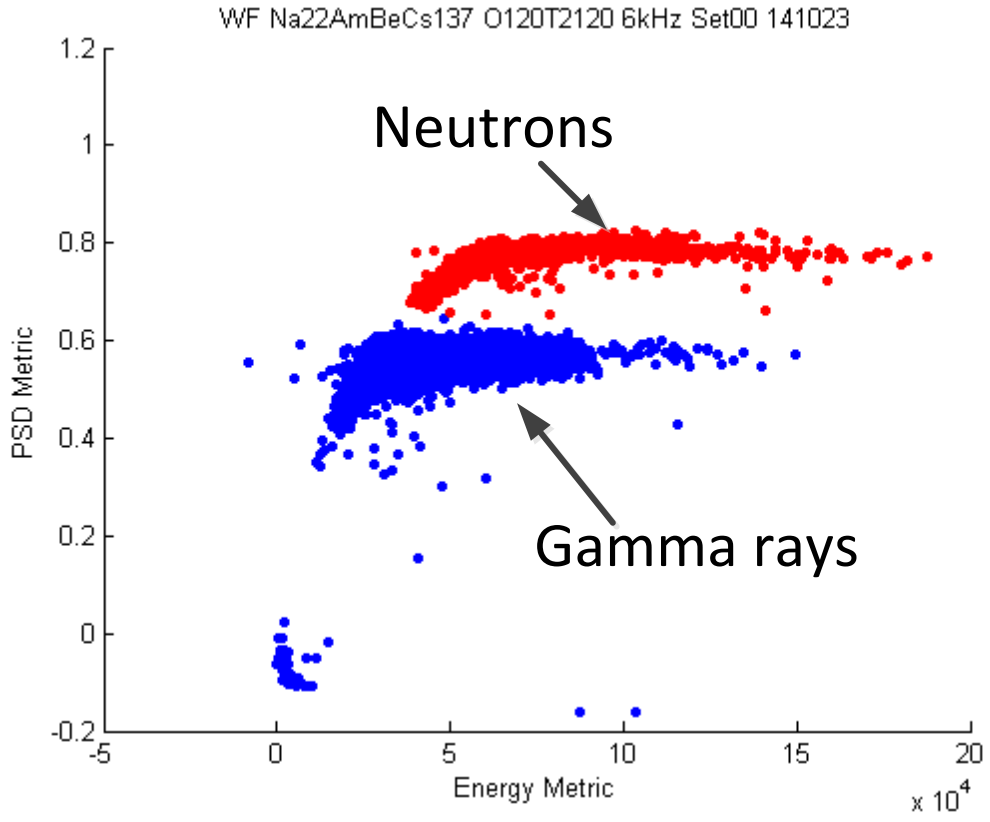

Fig. 5.22 PSD Plot of Reference Neutron Pulse and Other Pulses in Data File 2 from Table 3.2 at 6 kHz Event Rate.

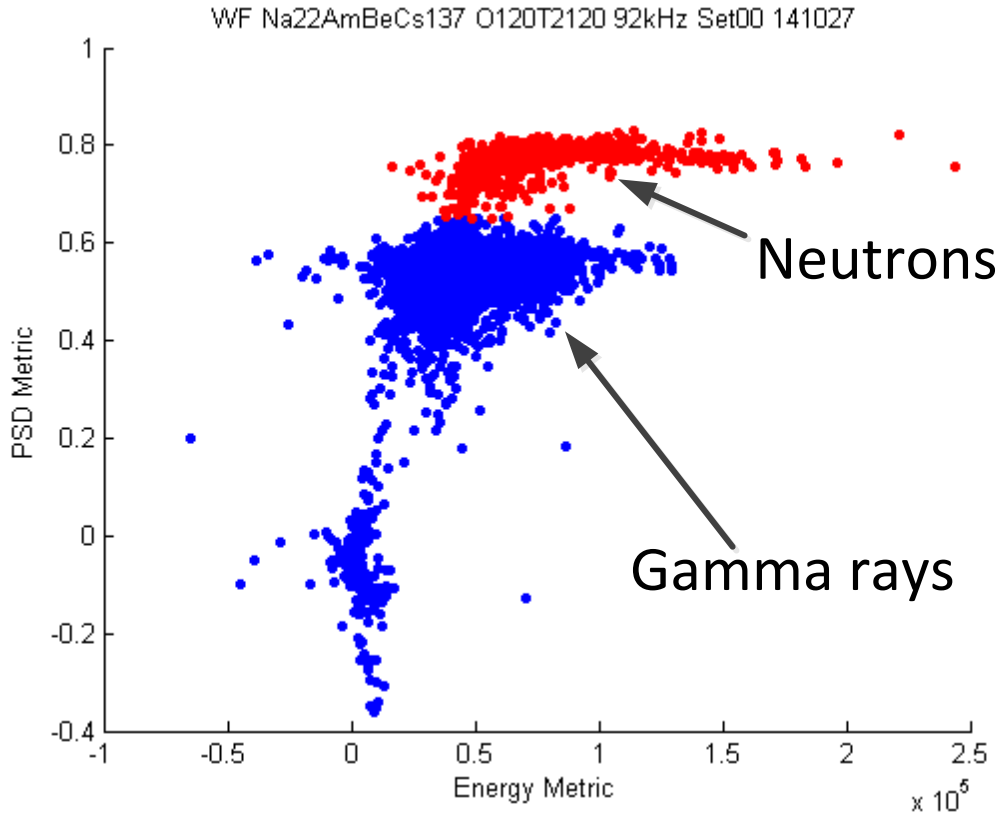

Fig. 5.23 PSD Plot of Reference Neutron Pulse and Other Pulses in Data File 4 from Table 3.2 at 92 kHz Event Rate.

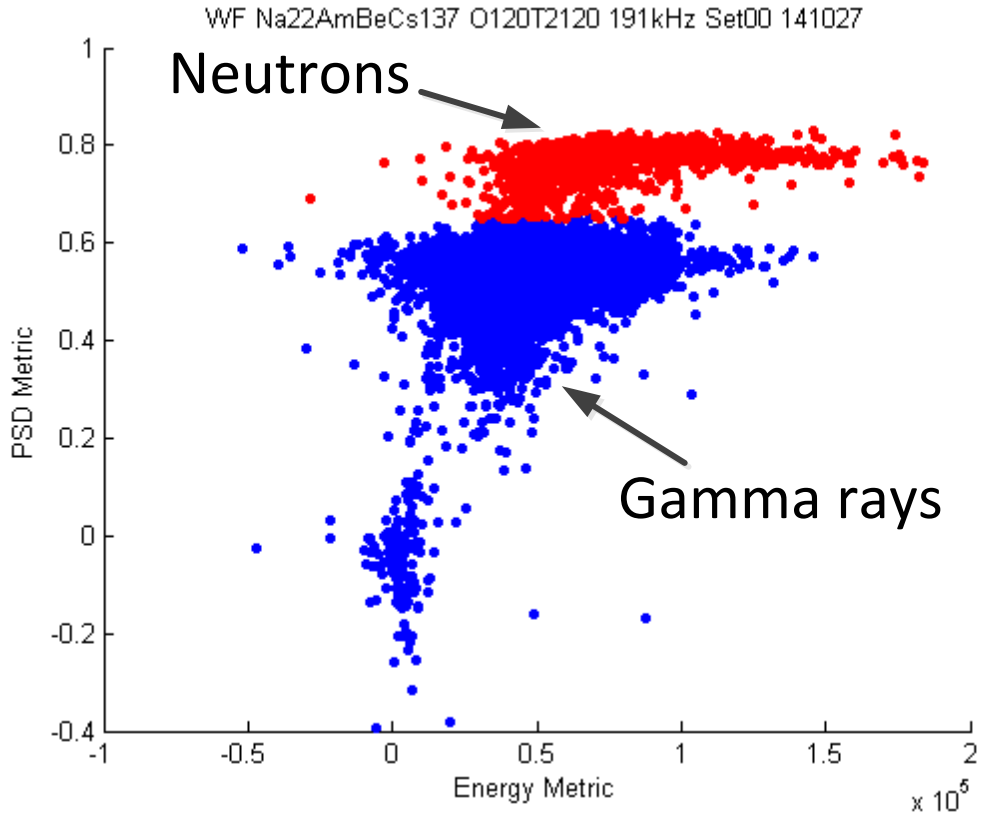

Fig. 5.24 PSD Plot of Reference Neutron Pulse and Other Pulses in Data File 5 from Table 3.2 at 191 kHz Event Rate.

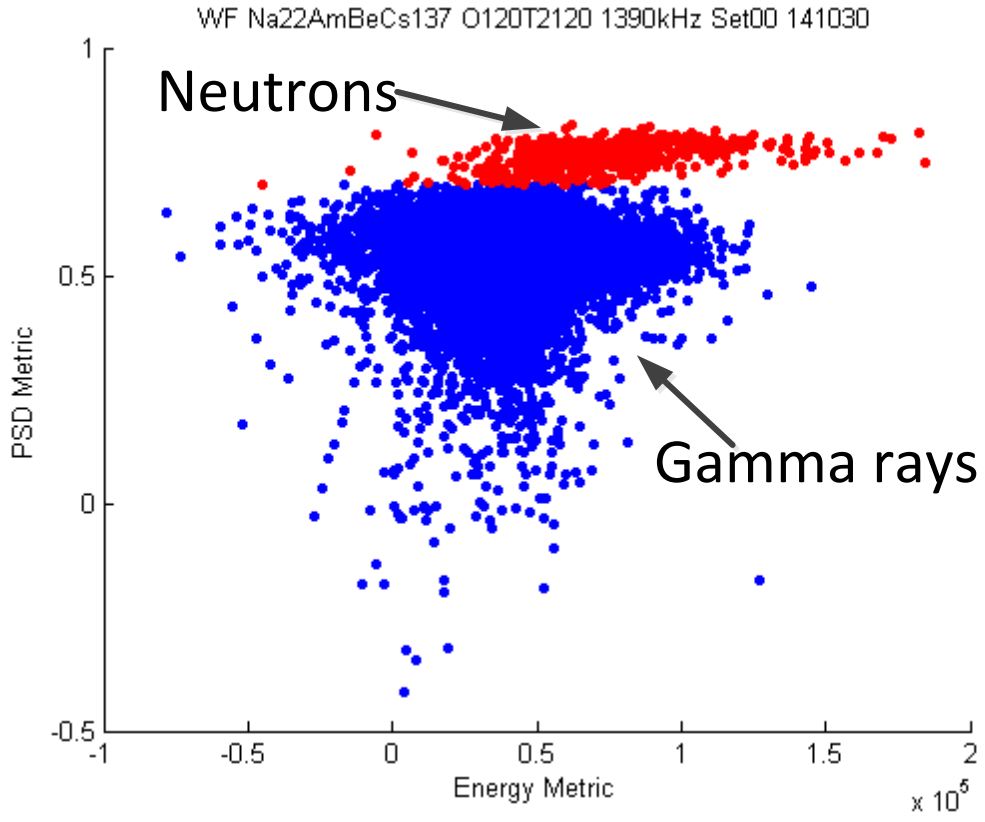

Fig. 5.25 PSD Plot of Reference Neutron Pulse and Other Pulses in Data File 8 from Table 3.2 at 1390 kHz Event Rate.

5.6. Pulse Shape Discrimination Using Reference Gamma Ray Pulse

Pulses that produce a PSD metric above 0.46 when correlated with the reference gamma ray pulse typically contain a high-energy neutron pulse and can be classified as a neutron pulse. Gamma ray pulses usually produce a PSD metric value below 0.6 when correlated with reference neutron pulse. By comparing Fig. 5.17 and Fig. 5.26, one can note that number of neutron pulses identified by using the reference gamma ray pulse is one hundred higher than the number of neutron pulses identified by the reference neutron pulse. A similar trend is also observed when Fig. 5.20 and Fig. 5.27 are compared. Visual

identification of all neutron pulses discriminated by the reference gamma ray pulse shows that some gamma ray pulses have been wrongly identified as a neutron pulse, thereby implying that the NCC with the neutron reference performs better.

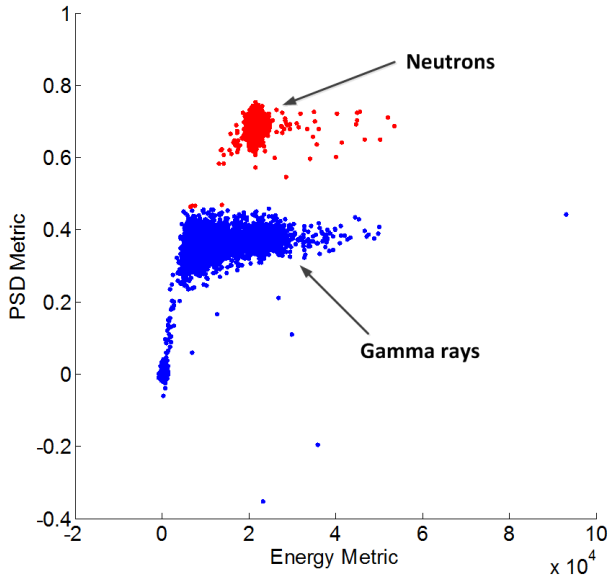

Fig. 5.26 PSD Plot of Reference Gamma Ray Pulse and Other Pulses in Data File 1 from Table 3.1 at 5 kHz Event Rate.

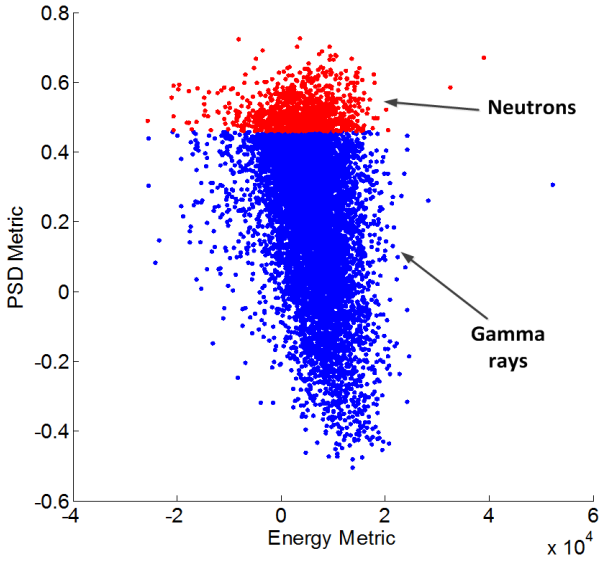

Fig. 5.27 PSD Plot of Reference Gamma Ray Pulse and Other Pulses in Data File 8 from Table 3.1 at 2.4 MHz Event Rate.

5.7. Distribution of Neutrons and Gamma Rays

In the previous section, application of the NCC technique to all data sets I and II was discussed. The results presented in Sections 5.1 and 5.5 can be confirmed by plotting the distribution of neutron and gamma ray pulses as a function of PSD metric for all the data sets I and II. The PSD metric was calculated using the method discussed in Section 5.4. Distributions of neutron and gamma ray pulses are then fitted using MATLAB function 'histfit' with option 'kernel'. Fig. 5.28, Fig. 5.29, Fig. 5.30, and Fig. 5.31 show the distribution of neutron and gamma ray pulses as a function of PSD metric for the event rates 6 kHz, 92 kHz, 191 kHz, and 1390 kHz from Table 3.2. In Fig. 5.28, the left peak represents gamma rays and right one represents neutrons. As expected at low event rates, the gamma ray and neutron peaks are widely separated. It is can be noted from Fig. 5.28 that the PSD metric, which is simply the NCC value, stays less than 0.6 for gamma ray

pulses and above 0.6 for neutrons. As the event rate increases, the separation between the two peaks decreases. At event rates above 180 kHz, shown in Fig. 5.30, the two distributions begin to merge and the number of pulses present between the peaks increases. At an extremely high event rate of 1390 kHz, shown in Fig. 5.31, the two peaks merge significantly.

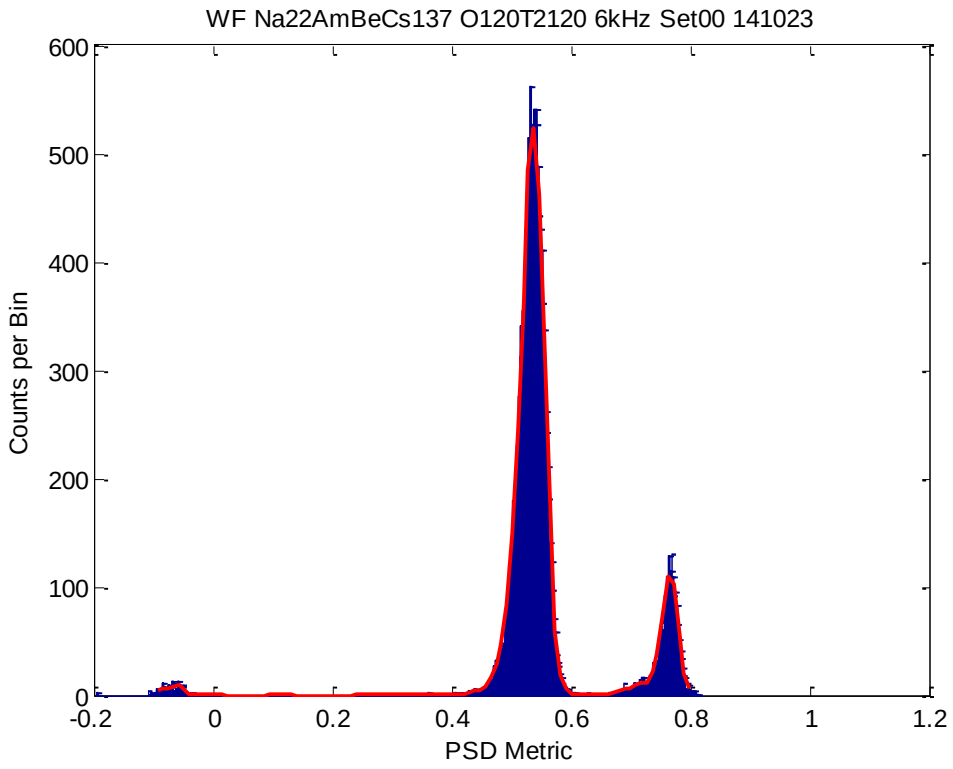

Fig. 5.28 Distribution of Neutron and Gamma Ray Pulses in Data File 1 from Table 3.2 at 6 kHz Event Rate.

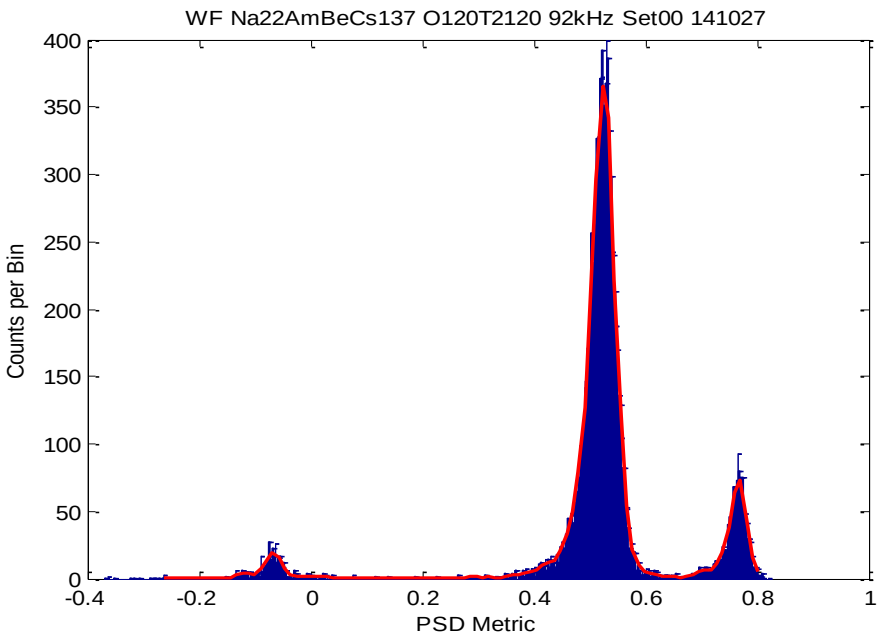

Fig. 5.29 Distribution of Neutron and Gamma Ray Pulses in Data File 4 from Table 3.2 at 92 kHz Event Rate.

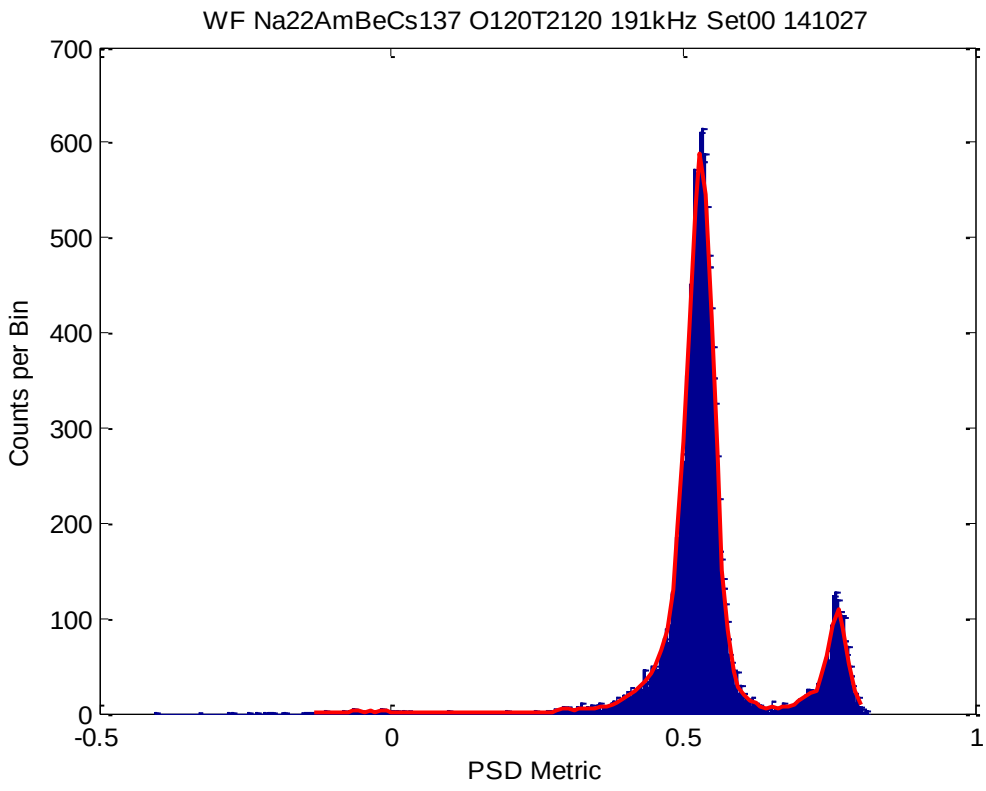

Fig. 5.30 Distribution of Neutron and Gamma Ray Pulses in Data File 5 from Table 3.2 at 191 kHz Event Rate.

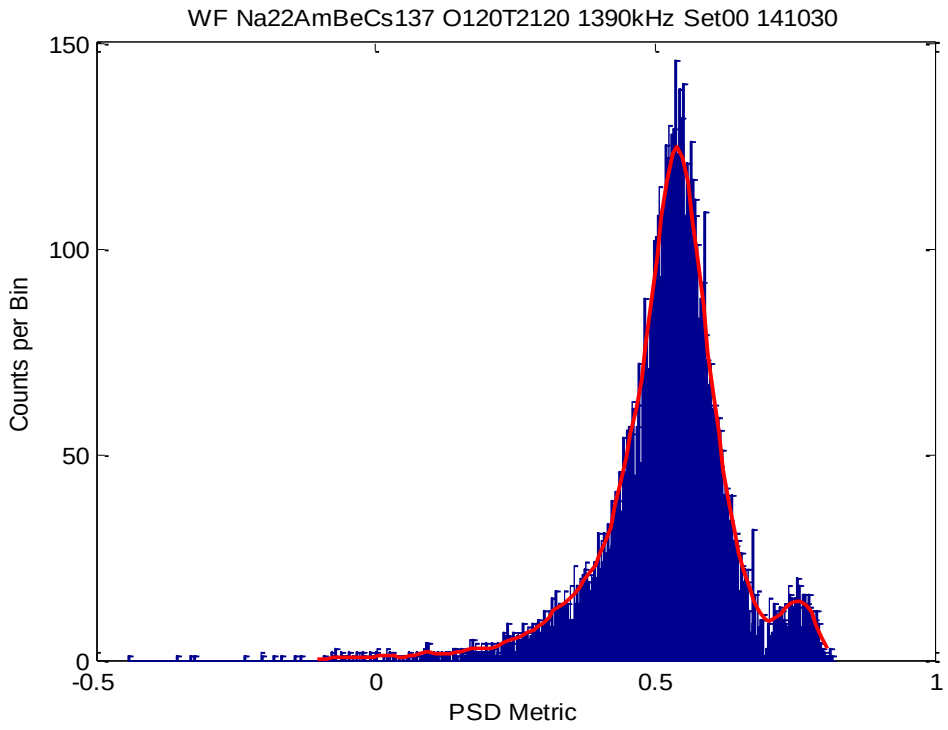

Fig. 5.31 Distribution of Neutron and Gamma Ray Pulses in Data File 8 from Table 3.2 at 1390 kHz Event Rate.

5.8. Comparison of Different PSD Methods

In this section, a comparison of the different PSD methods is made. Table 5.2 shows the comparison of the NCC method with the integral and filtered methods. It presents the number of neutrons detected, for different event rates and three methods such as NCC, integral and filtered methods discussed in Chapter 4. At a 6 kHz event rate, the NCC method has detected 1428 neutrons, whereas the integral and filtered methods have detected 1085 neutrons and 1111 neutrons, respectively. All the methods are compared to the integral method as it is a well-known method used in this application. This shows that the NCC method is not very off from the other two methods. As the event rate increases,

the neutron count decreases for all three methods. This can also be seen in Fig. 5.32 which plots the neutron count versus event rate. The neutron count remains almost constant until 370 kHz and drops off significantly as the event rate increases further. This is because of the difficulty in discriminating neutrons from gamma rays due to pileup, baseline shift and noise. The NCC method detects more neutrons compared to the other two methods as can be seen in Fig. 5.32. The filtered method and integral method neutron counts are very similar until 100 kHz. A further increase in event rate increases the neutron count for the integral method and decreases it for both the NCC and filtered methods.

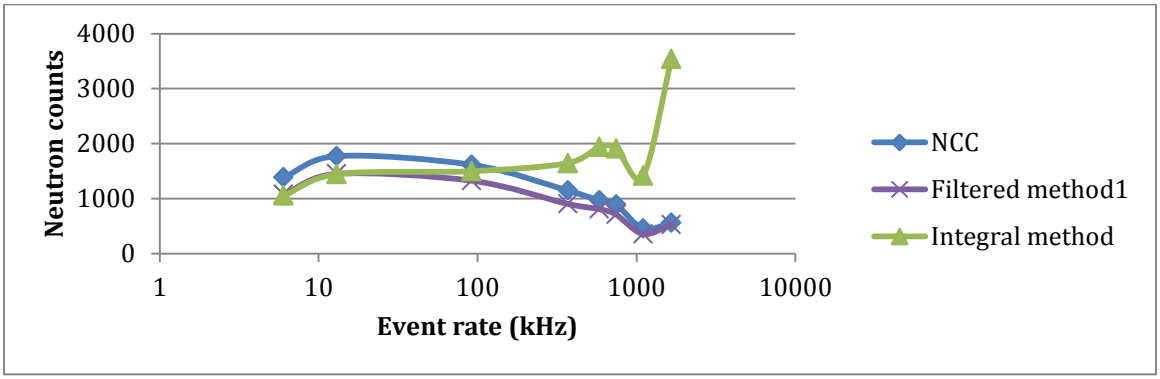

Fig. 5.32 Plot of Neutron Count with Event Rate for NCC, Filtered and Integral Methods.

Table 5.2 Comparison of NCC, Integral and Filtered Methods

Event rate (kHz)	Number of Samples in Data File	Data File Sampling Period (sec)	Filtered Method (PSD < 116 & Energy 2200<x<3300)	Integral Method (PSD < 0.525 & energy 2800 <x<3700)	NCC Method
6	2.58e+08	1.030029	1111	1085	1428
13	1.92e+08	0.766378	1112	1108	1360
92	1.8e+08	0.720175	955	1080	1164
370	1.96e+08	0.785187	710	1293	901
583	2.55e+08	1.021903	827	1981	990
745	3.52e+08	1.408893	1001	2697	1257
1100	1.54e+08	1.021903	366	1450	467
1660	4.02e+08	1.609499	850	5696	903

5.9. Figure Of Merit of NCC Method

As discussed in the previous chapter, the FOM is one metric for qualifying a PSD method. Table 5.3 shows the FOM calculation for different event rates. Fig. 5.33 plots FOM versus event rate. At low event rate, the FOM is around 3 which is good. As the event rate increases above 180 kHz, the FOM rolls off drastically. At high event rate, the FOM is 1.12 which is very low. This again is due to noise, pileup and baseline shift.

Table 5.3 FOM of NCC Method

Event rate	Gamma peak (NCC value)	Neutron peak (NCC value)	FWHMgamma	FWHMneutron	FOM	Cutoff (NCC value)
6	0.5344	0.7597	0.0399	0.0323	3.120	0.606
13	0.528	0.7619	0.037	0.0309	3.444	0.618
92	0.5227	0.77	0.0362	0.0307	3.696	0.666
370	0.5294	0.7653	0.038	0.0401	3.020	0.648
583	0.5353	0.7631	0.046	0.0438	2.536	0.668
745	0.5376	0.7567	0.0587	0.0376	2.275	0.721
1100	0.5396	0.7608	0.0957	0.0532	1.485	0.696
1660	0.5444	0.7568	0.142	0.0461	1.129	0.715

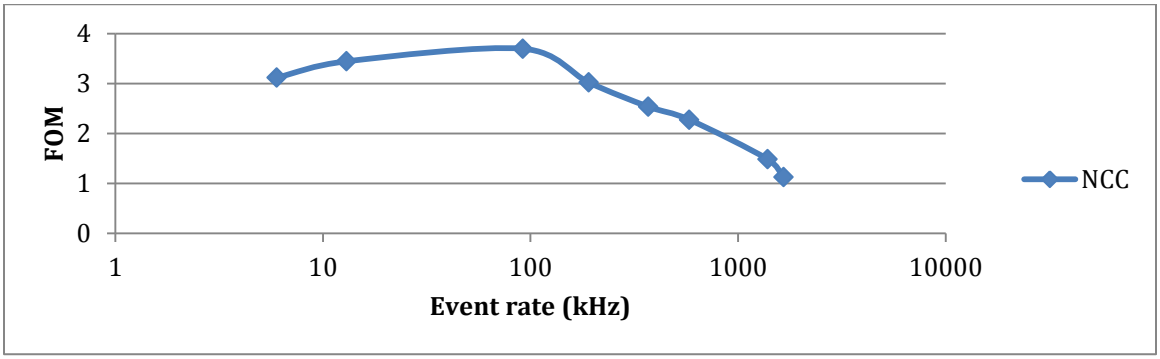

Fig. 5.33 FOM of NCC Method.

CHAPTER 6. CONCLUSION AND FUTURE WORK

As discussed in this thesis, due to the sensitivity of CLYC to gamma rays, pulse shape discrimination techniques are required to distinguish neutrons and gamma rays. PSD techniques such as charge comparison method, pulse gradient analysis, frequency gradient analysis are well researched and documented. One less explored technique, the cross correlation based PSD technique, is evaluated in this work. A neutron pulse produces a different NCC curve when compared to gamma ray pulse when it is cross correlated with either a template neutron or template gamma ray pulse. A template neutron pulse was obtained by modelling an experimentally obtained pulse using Marrone's equation. The parameter values used in Marrone's equation are obtained by manually adjusting the initial values of parameters obtained using Matlab curve fitting tool. With this template pulse, the NCC technique was applied to a large number of pulses from ^{137}Cs, AmBe, ^{252}Cf, ^{22}Na and ^{57}Co sources at different event rates from 1 kHz to 5300 kHz. The NCC curves obtained using the template neutron pulse produce significant neutron-gamma ray discrimination at low (< 100 kHz) to medium (< 200 kHz) event rates. However, at high event rates (> 200 kHz), the separation between gamma ray and neutron NCC curves disappears due to pileup, noise and baseline shift. PSD plots and the distribution of neutron and gamma ray pulses confirm this trend. The FOM of NCC is around 3, which is good, for low event rates and drops steeply as the event rate increases. Finally, at high event rates, the FOM settles down to around 1. The number of neutrons detected using the NCC technique is almost comparable to the integral method

and the filtered method at low event rates (< 100 kHz). However, the neutron count increases significantly at high event rates (> 200 kHz) when comparted to the other two methods. The NCC technique is a very simple approach to implement in hardware and it is worth exploring further to make it perform at high event rates as well.

Future work can focus on improving the hardware system, developing techniques to get rid of pileup, better shape recognition methods to detect neutron and gamma ray NCC curves. There is a distortion on the pulses detected by scintillator. They are significant particularly at high event rates. It is desired to have a high speed hardware system which can process the pulses quicker with reduced noise level. Pileup is the biggest problem at high event rates. Advanced algorithms can be developed to eliminate pileup which will be a significant breakthrough in scintillation detection. Finally, shape detection algorithms are required to differentiate neutron and gamma ray NCC curves. Future work also involves expanding the algorithms to not only count the pulses but also to provide rudimentary neutron and gamma energy spectra.

REFERENCES

[1] Nuclear Material Accounting Handbook, IAEA, Austria. [Online]. Available: http://www-pub.iaea.org/MTCD/publications/PDF/svs_015_web.pdf

[2] S. Adee. (2010, September) Physics Projects Deflate for Lack of Helium-3: US Radiation Detectors Suck up the Existing Supply. IEEE Spectrum [Online]. Available: http://spectrum.ieee.org/biomedical/diagnostics/physics-projects-deflate-for-lack-of-helium3

[3] A. P. Simpson, S. Jones, M. J. Clapham, et al., "A Review of Neutron Detection Technology Alternatives to Helium-3 for Safeguards Applications," in *Proc. of the 52th Annual Meeting of the Institute of Nuclear Materials Management*, Palm Desert, CA, July 17-21, 2011.

[4] T. Persons and G. Aloise (2011, September). Technology Assessment: Neutron Detectors: Alternatives to Using Helium-3. United States Government Accountability Office GAO-11-753. [Online]. Available: http://www.gao.gov/assets/590/585514.pdf

[5] D. W. Lee, L. C. Stonehill, A. Klimenko, et al., "Pulse-shape analysis of Cs2LiYCl6:Ce scintillator for neutron and gamma-ray discrimination," *Nuclear Instruments and Methods in Physics Research*, vol. A 664, pp. 1-5, 2012.

[6] J. Glodo, W. M. Higgins, E. V. D. van Loef, et al., "Scintillation Properties of 1 Inch Cs2LiYC6:Ce Crystals," *IEEE Transactions on Nuclear Science*, vol. 55, pp. 1206-1209, 2008.

[7] J. Glodo, R. Hawrami, E.V.D. Van Loef, U. Shirwadkar, K.S. Shah, "Pulse shape discrimination with selected elpasolite crystals," *IEEE Transactions on Nuclear Science*, vol. 59, pp. 2328-2333, 2012.

[8] K.A.A. Gamage, M.J. Joyce, N.P. Hawkes, "A comparison of four different digital algorithms for pulse-shape discrimination in fast scintillators," *Nuclear Instruments and Methods in Physics Research*, vol. A 642, pp. 78-83, 2011.

[9] B. D'Mellow, M.D. Aspinall, R.O. Mackin, M.J. Joyce, A.J. Peyton, "Digital discrimination of neutrons and γ-rays in liquid scintillators using pulse gradient analysis," *Nuclear Instruments and Methods in Physics Research*, vol. A 578, pp. 191-197, 2007.

[10] G. Liu, M. J. Joyce, X. Ma, and M. D. Aspinall, "A digital method for the discrimination of neutrons and gamma-rays with organic scintillation detectors using

frequency gradient analysis," *IEEE Transactions on Nuclear Science*, vol. 57, no. 3, pp. 1682-1691, June 2010.

[11] S. Yousefi, L. Lucchese, M.D. Aspinall, "Digital discrimination of neutrons and gamma-rays in liquid scintillators using wavelets," *Nuclear Instruments and Methods in Physics Research*, vol. A 598, pp. 551-555, 2009.

[12] V. Esmaeili-sani, A. Moussavi-zarandi, N. Akbar-ashrafi, B. Boghrati, H. Afarideh, "Neutron–gamma discrimination based on bipolar trapezoidal pulse shaping using FPGAs in NE-213," *Nuclear Instruments and Methods in Physics Research*, vol. A 694, pp. 113-118, 2012.

[13] M. Mardiyanto. (2008, August). Neutron-gamma pulse shape discrimination with a NE-213 liquid scintillator by using digital signal processing combined with similarity method. Atom Indonesia. [Online]. Available: http://aij.batan.go.id/index.php/aij/article/view/101

[14] M. Nakhostin, "Recursive algorithms for digital implementation of neutron/gamma discrimination in liquid scintillation detectors," *Nuclear Instruments and Methods in Physics Research,* vol. A 672, pp. 1-5, 2012.

[15] M. Faisal, R. T. Schiffer, M. Flaska, A. Pozzi, D.D. Wentzloff, "A correlation-based pulse detection technique for gamma-ray/neutron detectors," *Nuclear Instruments and Methods in Physics Research*, vol. A 652, pp. 479-482, 2011.

[16] Hamamatsu. PHOTOMULTIPLIER TUBES. [Online]. Available: https://www.hamamatsu.com/resources/pdf/etd/PMT_handbook_v3aE.pdf

[17] C. Chatfield, *The Analysis of Times Series: An Introduction*, 6th ed., Chapman & Hall/CRC Press, 2004, p. 333.

[18] E. B Johnson, C. Whitney, X. J. Chen, S. Vogel, J. F. Christian, K. Shah, A. Gueorguiev, M. McClish, K. E. Holbert, "Prototype of a CLYC based detector system for special nuclear material accounting," in *Proc. of the 54th Annual Meeting of the Institute of Nuclear Materials Management*, Palm Desert, CA, July 14-18, 2013.

[19] S. Marrone et al., "Pulse shape analysis of liquid scintillators for neutron studies," *Nuclear Instruments and Methods in Physics Research,* vol. A 490, pp. 299-307, 2002.

APPENDIX A

PSD PLOTS OF DATA FILE-II USING INTEGRAL METHOD

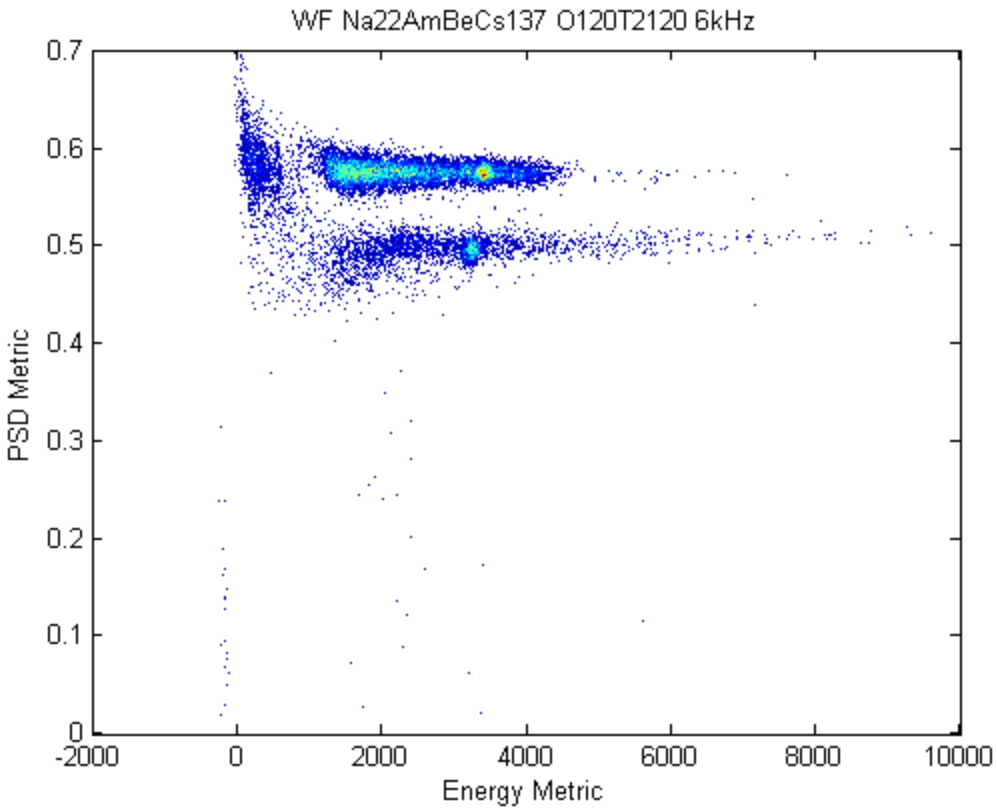

PSD plot of pulses from data file 2 in Table 3.2 at 6 kHz event rate

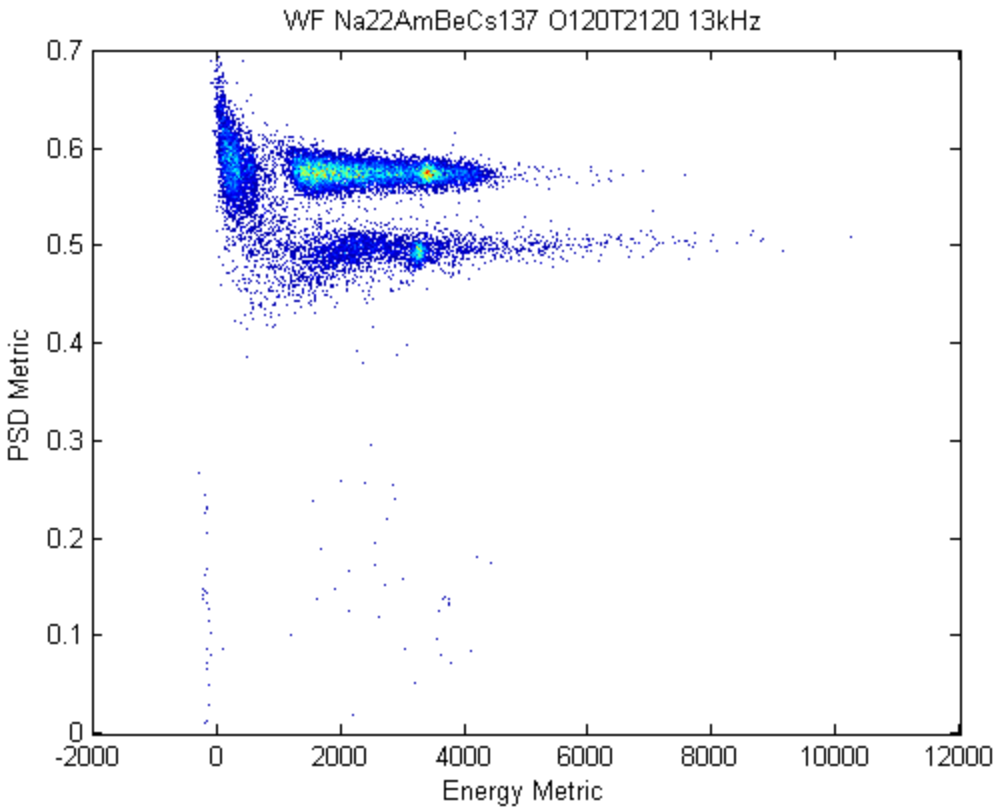

PSD plot of pulses from data file 3 in Table 3.2 at 13 kHz event rate

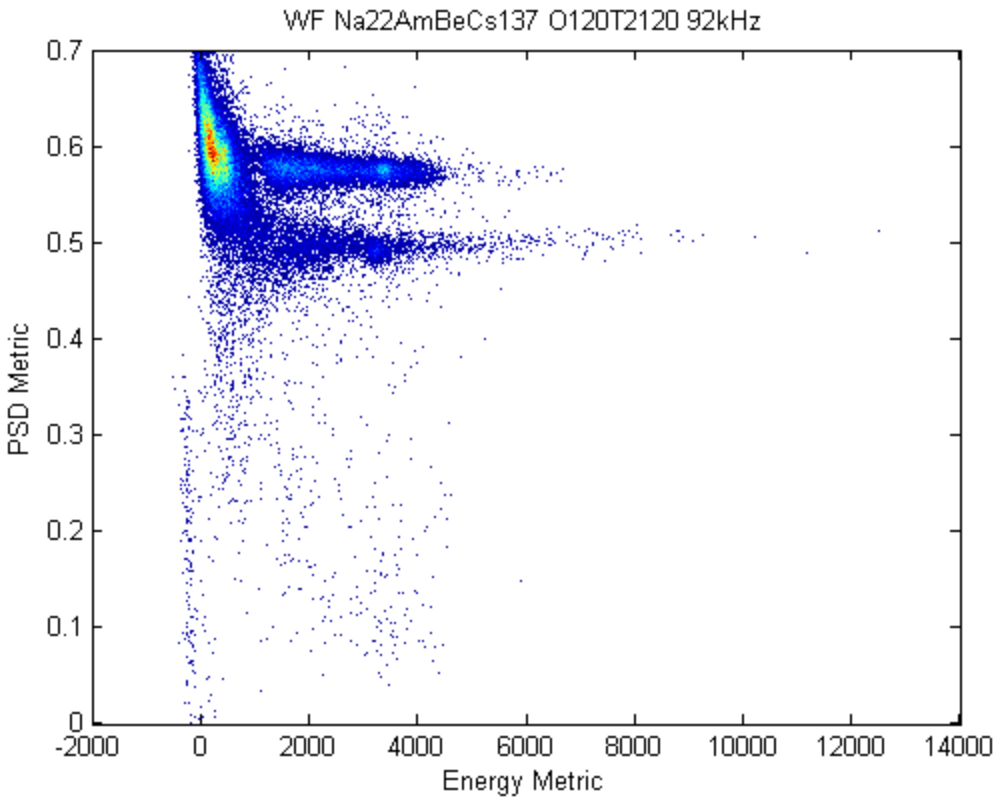

PSD plot of pulses from data file 4 in Table 3.2 at 92 kHz event rate

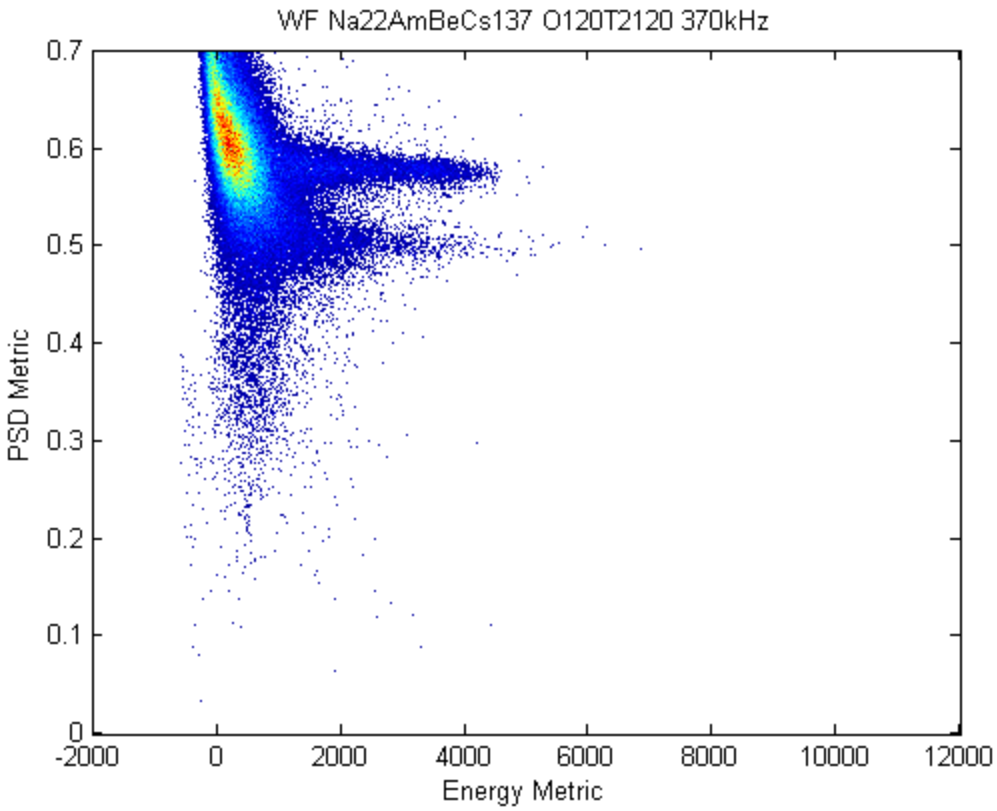

PSD plot of pulses from data file 6 in Table 3.2 at 370 kHz event rate

APPENDIX B

PSD PLOTS OF DATA FILE-II USING FILTERED METHOD

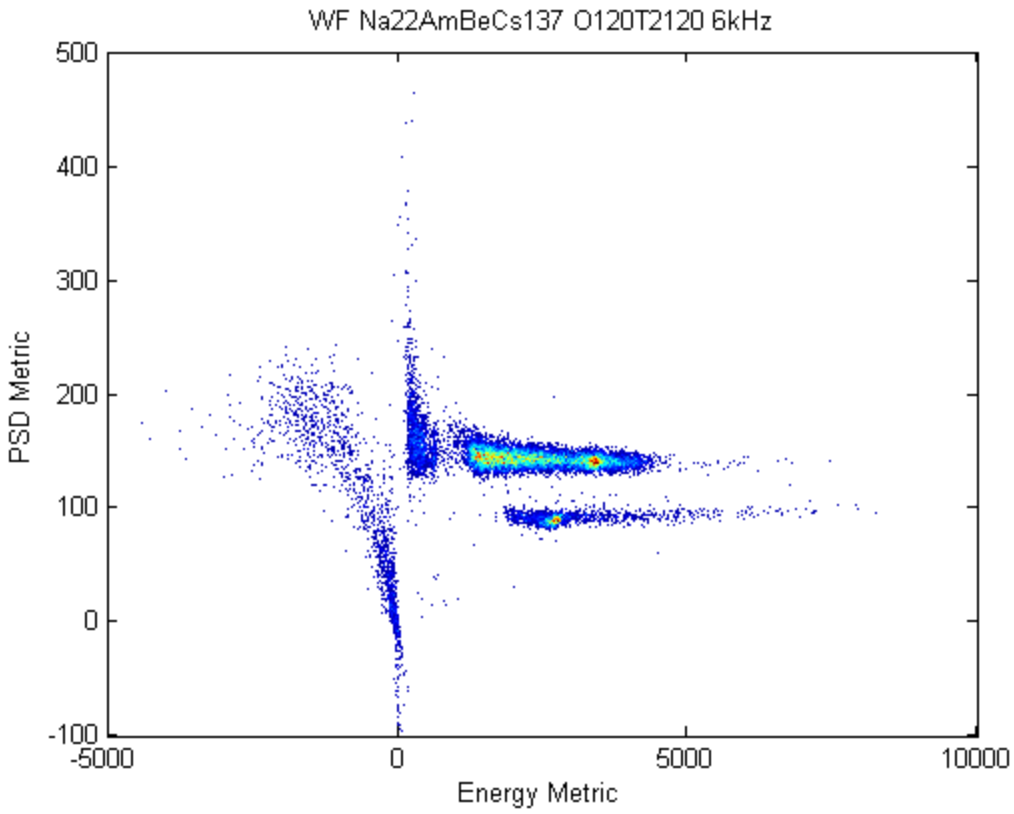

PSD plot of pulses from data file 2 in Table 3.2 at 6 kHz event rate

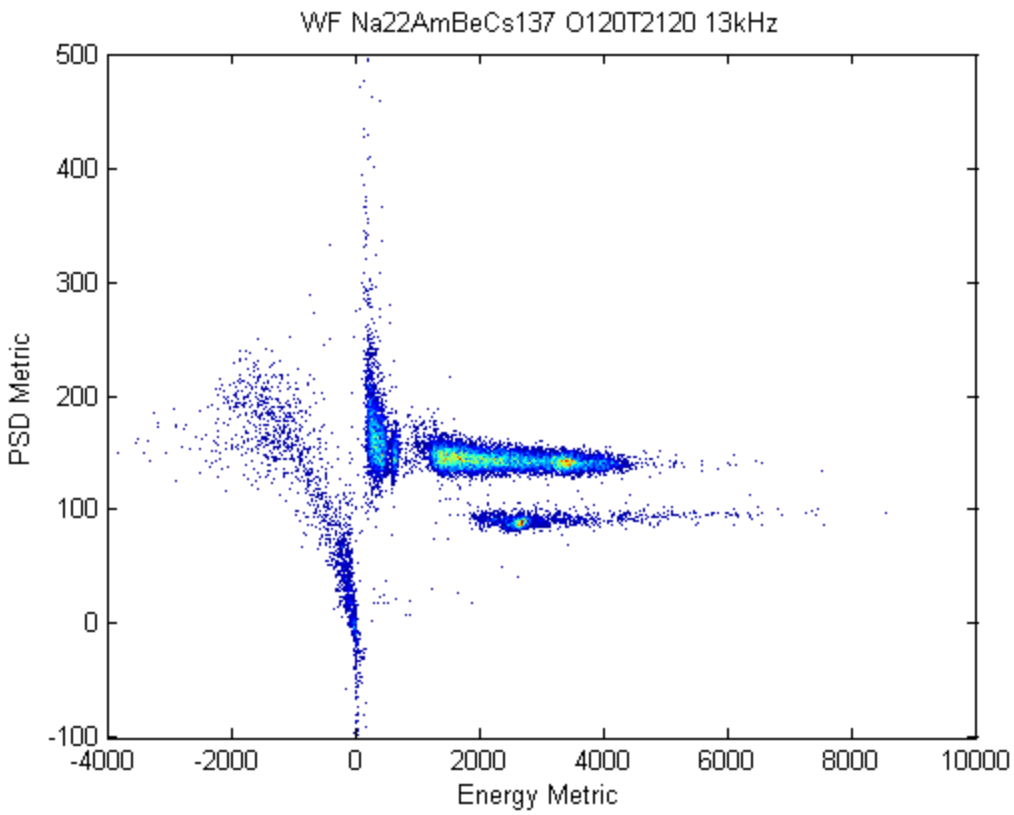

PSD plot of pulses from data file 3 in Table 3.2 at 13 kHz event rate

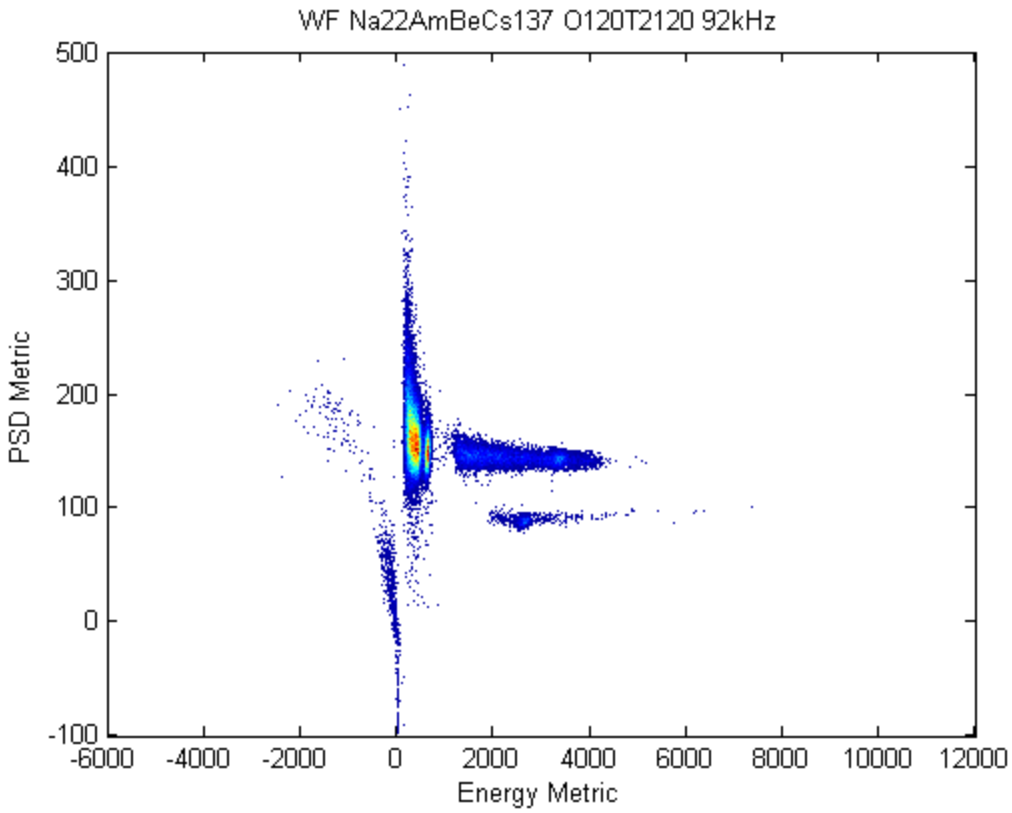

PSD plot of pulses from data file 4 in Table 3.2 at 92 kHz event rate

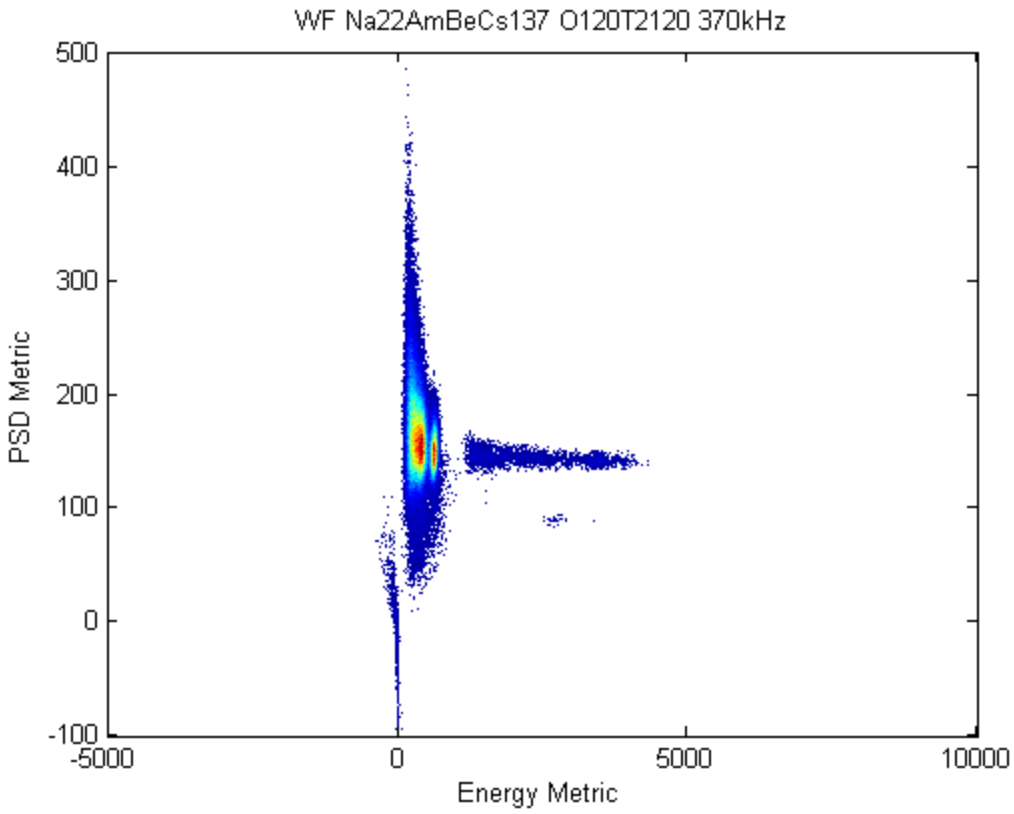

PSD plot of pulses from data file 6 in Table 3.2 at 370 kHz event rate